Effects of Random Surface Errors on the Performance of Paraboloidal Reflectors

by

Siwaphong Boonsalee

Submitted to the Department of Electrical Engineering and Computer Science
in partial fulfillment of the requirements for the degrees of
Bachelor of Science in Electrical Science and Engineering
and
Master of Engineering in Electrical Engineering and Computer Science
at the
MASSACHUSETTS INSTITUTE OF TECHNOLOGY
February 2000 [February 2001]

[redacted]

Author ....
Department of Electrical Engineering and Computer Science
February 6, 2001

Certified by ....
Jin A. Kong
Professor
Thesis Supervisor

Certified by ....
Yan Zhang
Research Affiliate
Thesis Supervisor

Accepted by ....
Arthur C. Smith
Chairman, Department Committee on Graduate Students

Effects of Random Surface Errors on the Performance of Paraboloidal Reflectors

by

Siwaphong Boonsalee

Submitted to the Department of Electrical Engineering and Computer Science
on February 6, 2001, in partial fulfillment of the
requirements for the degrees of
Bachelor of Science in Electrical Science and Engineering
and
Master of Engineering in Electrical Engineering and Computer Science

Abstract

A program based on ray tracing has been developed to study the radiation patterns of paraboloidal reflector antennas whose surfaces are subjected to random errors with the emphasis on using an accurate representation of the statistics of the random surface errors. An ensemble of Gaussian random surfaces is created to be used with the Monte Carlo simulation. The average patterns from different surface root-mean-square values are presented for both the co-polarized and cross-polarized fields on the E-plane, H-plane, and 45-degree plane. They are compared with results based on physical optics and the antenna tolerance theory.

Thesis Supervisor: Jin A. Kong
Title: Professor

Thesis Supervisor: Yan Zhang
Title: Research Affiliate

Acknowledgments

I have been growing along with this thesis for the last three years of my life. It has been an incredibly painful period. Now it is all over, and I would like to say something about the people who I have come into close contact with during my last three years at MIT. I would like to express my appreciation for all things they have done for me.

First of all, I would like to thank my thesis advisor, Professor Jin Au Kong, for the opportunity to begin, and to finish, this thesis work. His deep understanding, sympathy, and kindness have been acknowledged, and they will stay with me. I am also in great debt to Dr. Yan Zhang, my thesis supervisor, who has helped me develop better understanding of the subject until I can finish this thesis. I will always remember him for his kindness and his friendship.

Next, I would like to thank my academic advisor, Professor James D. Bruce, who has been advising and encouraging me since I was a sophomore. His schedule is always very busy, but he always has time for his advisees when they need him most.

I am privileged to have received the sincere love and support from Ms. Anne M. Hunter, the Course secretary, who has been like a mother to all the department's undergraduate students. As long as she stays with the department, there will always be some troubled kids coming along, but her great sympathy and understanding will make MIT more tolerable for them.

I have long been in great debt to my superiors at the Aeronautical Radio of Thailand for granting me the scholarship to do my Master's degree at MIT, and for extending the grant period until now. I will never be able to pay back in full for the goodwill that they have endowed into me. The same gratitude is also given to the Royal Thai Government for granting me the King Scholarship and for the opportunity to study at MIT as an undergraduate student.

I have a lot to thank many of my fiends who have been hanging around me during this difficult period of my life. Kulpant (Namo) Pimsamarn, Yot Boontongkong, Poompat (Tengo) Saengudomlert, Pimpa (Oy) Limthongkul, Thanisara (Ant) Kiatbaramee, Suchatvee (Vince) Suwansavat, Pradya (Ou) Prempraneerach, Attasit (Pong) Korchaiyapruk, Wei Leung (Keith) Low, and Daniel Hu, for their continued friendship and support during the time that I needed them most.

I would like to thank everyone in my family for their love and support. I would like to express my deepest gratitude to one of them in particular, who I feel has been the person who understands me most. She has been supporting me greatly by preserving the bond between me and my parents during the most difficult periods. This person is my younger sister, Sansanee Boonsalee, who is the most wonderful sister in the world.

Last and most important, I would like to dedicate this work to my parents, Mrs. Jintana and Mr. Poonsak Boonsalee, for everything they have done for me since the beginning of my life. They have endured more than anybody during the last two years that I have been struggling with myself, yet they have never stopped believing in me then, now, and perhaps forever.

To my parents

Contents

List of Figures

List of Tables

Chapter 1

Introduction

1.1 Paraboloidal reflector antennas

An antenna is the part of a transmitting or receiving system which is designed to radiate or receive electromagnetic waves [1]. It provides a transition from a guided wave on a transmission line to a wave in free space. A reflector antenna is an antenna consisting of one or more reflecting surfaces and a radiating feed system. Reflector antennas are used to provide a pencil-beam radiation, which gives a magnification to the gain of the source radiator and focuses the radiated energy into a specific direction. Most reflector surfaces are derived from the conic sections with well known geometrical properties such as circles, parabolas, hyperbolas, and ellipses [2]. Reflecting surfaces are generated by translation or by rotation of the curves around the focal axis. In principle, such reflectors are wideband devices, capable of operating from radio to optical frequencies [3]. As a source of high-gain microwave beam, reflector antennas are more preferred to lens and array antennas because they are the simplest, the cheapest, and the lightest option [2][4].

Among various types of reflector antennas, paraboloidal reflectors are the most utilized [2]. They are used as stand-alone reflectors or as primary reflectors in both the Cassegrain and the Gregorian reflector systems. A paraboloidal reflector surface is specified by two parameters: (1) the diameter D, and (2) the focal length f. However, it is often stated in terms of the size D and the shape of the paraboloid by the focal-to-diameter ratio f/D. The f/D ratio represents the curvature of the dish when D is fixed. The angle θ_0 from the main axis to the rim of the reflector is related to the f/D ratio by

$$\theta_0 = 2\tan^{-1}\left(\frac{1}{4f/D}\right) \tag{1.1}$$

which can be rewritten as

$$f/D = \frac{1}{4\tan(\theta_0/2)} \tag{1.2}$$

Equation (1.2) suggests that a reflector with diameter size D becomes flatter as the f/D ratio increases.

Two properties of the paraboloid make it an efficient structure for focusing radiation energy into a directional beam. First, the path lengths from the focal point to the aperture plane via the paraboloidal reflector are the same for all (geometrical optics) rays. Second, the reflected rays from the reflector surface are parallel to the reflector axis [5][6]. Thus, a paraboloidal reflector will transform radially emerging rays from a point source at the focus into parallel rays at the aperture plane of the reflector.[1] Such structure can be used

---

[1] The aperture plane of an antenna is a surface on which it is convenient to make assumption regarding the field values for the purpose of computing the radiated fields. It is often taken to be a plane near the

to convert electromagnetic waves with a spherical phase front into those with a plane phase front [7]. In addition, we will find that the field on the aperture plane has a uniform phase.

The feed is a very important part of reflector antenna systems. It requires a good combination of amplitude, phase, and polarization of the field incident on the reflector to achieve the maximum efficiency. The feed of a reflector antenna should be small in size and give a spherical phase front as if the energy is radiated from a single point. The amplitude of the radiation from the feed must be uniform over a wide angle to illuminate the entire area of the reflector adequately. A good feed must also direct most of its radiation energy into the area of the reflector to avoid the spill over, which is a loss of energy by waves radiated from the feed that fail to strike the reflector. The radiation characteristic of the feed should be such that all the waves will be polarized in the same direction after reflection from the reflector surface. Radiation from the perpendicularly polarized component of the aperture field will contribute to minor lobes and be wasted [2].

The paraboloidal reflector is a wideband antenna. The bandwidth of a reflector is determined at the low frequency by the size of the reflector. It should be at least several wavelengths in extent. Towards the high frequency end, performance is limited by the smoothness of the reflector surface. Surface distortions must be much less than a wavelength to avoid significant phase errors in the aperture.

---

antenna which is perpendicular to the direction of maximum radiation [1].

1.1.1 Radiation patterns of paraboloidal reflector antennas

Radiation pattern or antenna pattern is the angular variation of radiation intensity at a fixed distance from an antenna when it is transmitting. Since most antennas are reciprocal devices, they display the same characteristic when they are used for transmission and reception of electromagnetic waves. Figure 1-1 shows a typical radiation pattern of paraboloidal reflector antennas with dipole feeds located at the focal point. The area around the center of the co-polarized pattern is the main lobe, which represents the solid angle containing the most intense portion of the radiation. This is because the fields from various parts of the antenna arrive at this area more in-phase than they do for other directions [6]. The highest peak is located at the center of the main lobe, which is the direction where the radiation field is strongest. The rest of the pattern are collectively called minor lobes or side lobes, which represent the radiated energy that is not contained in the main lobe.

In most applications, it is undesirable to transmit or to receive electromagnetic energy in different directions other than that of the main lobe. If an antenna with high side lobe level is used at the transmitter, a large amount of the radiated energy will be wasted. This leaked energy may cause interference to the nearby receivers. At the receiver, an antenna with a high side lobe level has more potential to pick up unwanted energy from the background, which may degrade the signal-to-noise ratio.

The radiation pattern of a reflector antenna is a function of the reflector geometry and the feed illumination. The most basic method to analyze reflector antennas is to use geometrical optics to find the aperture-field distribution by tracing geometrical optics rays from the source to the aperture. For the paraboloidal reflectors, all rays from the feed travel the same

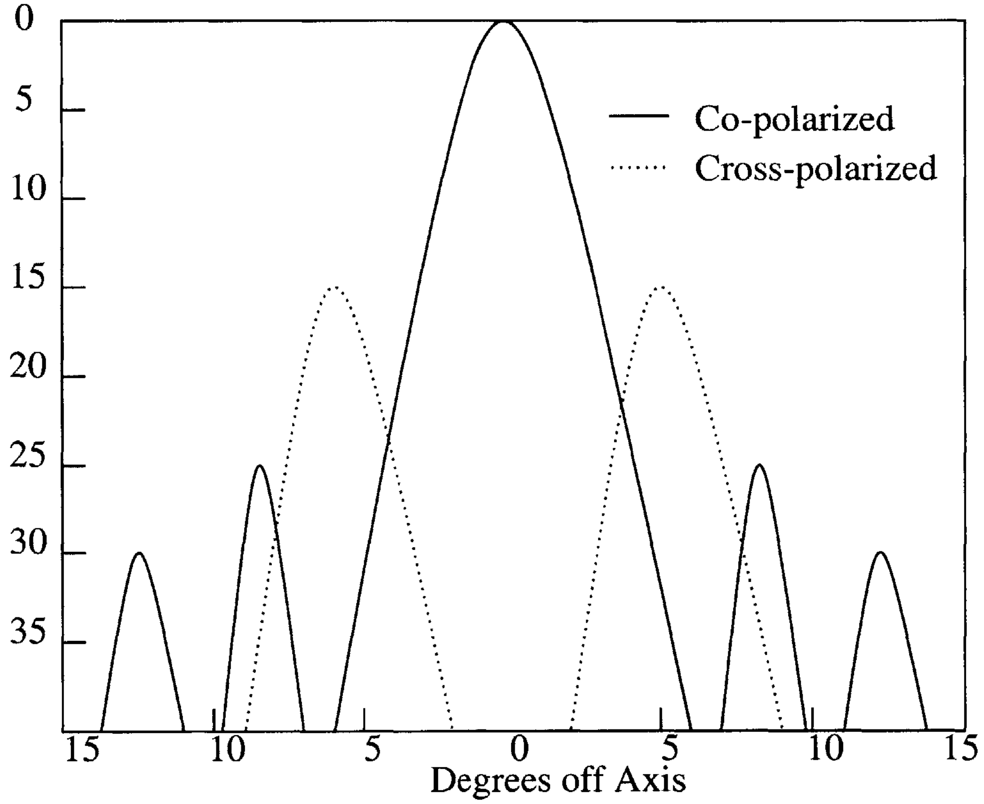

Figure 1-1: A typical radiation pattern of paraboloidal reflector antennas showing the co-polarized pattern (filled lines) and the cross-polarized pattern (dotted lines).

distance to the aperture plane, and the field distribution on the aperture will have a uniform phase. However, the distribution of the amplitude need not be uniform.[2] Once the aperture-field distribution is known, the radiation field can be found by solving a two-dimensional diffraction integral of the aperture field. The integral is given by

$$\begin{aligned} \overline{E}(\overline{r}) &= i\omega\mu\frac{e^{ikr}}{4\pi r}(\hat{\theta}f_\theta + \hat{\phi}f_\phi) && (1.4) \\ \overline{f}(\theta,\phi) &= \iint_{A'} \overline{E}_{ap}e^{-ik\rho'\sin\theta\cos(\phi-\phi')}\rho' d\rho' d\phi' && (1.5) \end{aligned}$$

where the primed variables are those associated with the aperture plane, and the unprimed variables are those associated with the radiation field. The integral in Equation (1.5) can be rewritten to illustrate the Fourier relationship between the aperture field and the radiation field as follow

$$\overline{f}(\theta,\phi) = \iint_{A'} \overline{E}_{ap}(x',y')e^{-ikux'-ikvy'}dx'dy' \qquad (1.6)$$

where $u = \sin\theta\cos\phi$ and $v = \sin\theta\sin\phi$ are the pattern variables. Alternatively, we may use physical optics to approximate the induced surface currents, which can be integrated over the reflector surface or on the aperture plane.

The size of reflector antennas is closely related to the beamwidth. Reflector antennas with larger size compared to the wavelength have narrower beamwidths for the main lobe and yield higher maximum gains. These two features are desirable in most reflector antenna

---

[2] The following polynomial function is often used as a practical approximation of the aperture-field distribution [8]

$$E_{ap}(\rho) = E_0[B + (1-B)(1-\rho^2/R^2)^p] \qquad (1.3)$$

where E_0 is a constant, ρ is the radial coordinate of a point on the circular aperture $(0 \leq \rho \leq R)$, R is the maximum radius of the aperture, and B is a constant that specifies the degrees of edge tapering. B is dimensionless and is usually converted to decibels by taking the logarithm and multiplying by 20.

applications. In radar and radio astronomy applications, antennas with narrow beamwidths give better angular resolution and bring greater accuracy. In communication systems, antennas with high maximum gain bring good signal-to-noise ratios for the transmitted and received signals using the same level of transmission power [9].

1.2 Effect of random surface errors on the performance of reflector antennas

The surfaces of reflector antennas in operating conditions are subjected to deviations from the ideal surface. The deviations make it difficult to maintain the desired amplitude and phase of the fields on the aperture, making the overall performance of the antenna deteriorates. Many important measures of reflector antenna performance—the maximum gain, the beamwidth, the maximum side lobe level, and the cross-polarization interference—are degraded by the presence of surface errors. This section describes the nature of the surface errors on reflector antennas along with the effects of random surface errors on the performance parameters outlined above.

1.2.1 Surface errors on reflector antennas

Surfaces of large reflector antennas, such as those required for radio astronomy or interplanetary sciences, are subject to distortions caused by forces of gravity, wind loads, thermal strains, manufacturing tolerances, and misalignment of the panels [10][11][9]. The surface errors caused by these conditions can be put into two categories: the deterministic errors

Table 1.1: The manufacturing tolerance ratios of some large reflector antennas

Agency/Location	$D(m)$	$\varepsilon_{rms}(mm)$	R
Cal Tech, Owens Valley	10.4	.025	416000
Univ. Massachusetts	13.7	.100	137000
ESSCO	20.1	.150	134000
Crimean RT-22	22.0	.120	183000
NRAO, Charlottesville	25.0	.070	357000
IRAM, Grenoble, Spain	30.0	.090	333000
RRL, Kashima, Japan*	34.0	.127	268000
Nobeyama	45.0	.200	225000
Effelsberg**	60.0	.400	150000
JPL***	70.0	.430	163000
Effelsberg	100.0	.730	137000

*Proposal **Inner $60\,m$ of the $100\,m$ Effelsberg antenna ***Proposed upgrade

and the random errors. The causes of deterministic, or systematic , distortions include the gravitational forces, wind loads, thermal expansions, and structural designs such as support ribs and slots between panels [12]. To a large extent, the deterministic surface deformations can be mechanically compensated for by manually adjusting the antenna profiles or by using adaptive reflector surfaces [13][14]. Electromagnetic compensation techniques based on feed array can be used to supplement the mechanical techniques to deal with subtle residual errors.

Most moderate to large reflectors are constructed from many pieces of panels which must be fabricated and assembled to form the final reflector. However, there is always some tolerance allowed in the manufacturing precision of the panels, which is a well-known cause of random surface errors. The manufacturing tolerance $R = D/\varepsilon_{rms}$ is specified by the ratio of the dish diameter D to the root-mean-square surface error ε_{rms} of the reflector [13][9]. Some manufacturing tolerance ratios of large antennas are presented in Table 1.1 (From [9]).

Precise measurement of the reflector accuracy during the fabrication and assembly, as well as during the operation, is necessary for maximum performance. Conventional mechanical and optical surveying techniques provide high degrees of accuracy in the production and construction of reflector antennas. During the fabrication and assembly stages, theodolite, prism, and inclinometer (for the measurement of angle) are useful. During the installation process, tape, rod, wheel, linear transducer, and modulated laser are used to give measurement of distance. Laser, microwave, and acoustic interferometric and holographic techniques can be applied to the surface metrology, which will be used to determine the surface profiles of antennas in operation [8].

In practice, a measure for the accuracy of the reflector surface is the surface rms, defined as the root-mean-square of one-half of geometrical optics path-length changes at discrete points on the aperture [15]. It has been discovered that the surface deviations are usually random and Gaussian in character, or at least likely to follow a bell-shaped curve [11]. The deviations may not be uniformly distributed, but for most part of the reflector this assumption holds true. The region of correlation of the surface deviations tends to be circular when the contours of adjustment are spaced in uniform grids. The number of uncorrelated regions over the reflector surface depends on the panel size and spacing of the target points.

1.2.2 Effect on the gain, directivity, and radiation pattern

The directive gain, or the gain, $G(\theta, \phi)$ of an antenna describes the variation of the radiation intensity with direction in space. $G(\theta, \phi)$ can be measured experimentally for an antenna with a matched feed [5]. It is defined as the ratio of the Poynting's power density $S_r(\theta, \phi)$

radiated in the (θ, ϕ) direction to the total power radiated by an isotropic antenna[3]

$$G(\theta, \phi) = \frac{< S_r(\theta, \phi) >}{P_r/4\pi r^2} \tag{1.7}$$

where P_r is the total radiated power, which is calculated by integrating S_r over a sphere of radius r with $r \to \infty$.

The radiation pattern $p(\theta, \phi)$ of the antenna is the relative distribution of radiated power as a function of direction in space. The radiation pattern is the gain normalized to unity by the maximum gain

$$p(\theta, \phi) = \frac{G(\theta, \phi)}{G_{max}} \tag{1.8}$$

The radiation pattern is often displayed in two planar sections called the E-plane and H-plane patterns. The E-plane pattern is a view of the radiation pattern obtained from a section which contains the electric field vector and the direction of maximum radiation. Similarly, the H-plane pattern is a sectional view which contains the magnetic field vector.

The directivity of an antenna is a measure of its ability to concentrate the radiated power in a given direction. The directivity is the maximum value of the gain of the antenna

$$G_{max} = max\{G(\theta, \phi)\} \tag{1.9}$$

---

[3] There are inconsistent definition and usage of the terms "directive gain", "gain", and "directivity". Our definitions are compatible with [16] and [7]. The IEEE [1] uses the same definition for the directive gain but uses the term "directivity" synonymously. The gain is defined differently by replacing P_r in Equation (1.7) with P_t, the amount of power accepted by the antenna. The two will become equivalent if the antenna radiates with 100 % efficiency.

The directivity of a paraboloidal reflector antenna is given by [17]

$$G_{max} = \eta_{ap} \left(\frac{\pi D}{\lambda} \right)^2 \tag{1.10}$$

where D is the diameter of the aperture, λ is the wavelength, and η_{ap} is the aperture efficiency. The aperture efficiency is the ratio of the directivity of an antenna to its standard directivity $(\pi D/\lambda)^2$, i.e., directivity of the aperture when illuminated by a uniform plane wave.

Equation (1.10) suggests that the antenna peak gain increases indefinitely with increasing frequency. In reality, however, the gain is often limited by deviations on the antenna surface from the ideal shape. Based on the antenna tolerance theory [11], the maximum gain is reduced by an exponential factor

$$G_{max} = \eta_{ap} \left(\frac{\pi D}{\lambda} \right)^2 e^{-(4\pi\varepsilon_{rms}/\lambda)^2} \tag{1.11}$$

where ε_{rms} is the root-mean-square value of surface deviations. Figure 1-2 shows the maximum gain of some large antennas as a function of frequency. For a given antenna, the reduction of the antenna peak gain increases with the frequency, and there is a value for the operating frequency which yields the maximum peak gain. The wavelength at this optimal frequency is found to be $\lambda = 4\pi\varepsilon_{rms}$. Further increase of operating frequency beyond this value will lead to more reduction of the peak gain [9].

The radiation patterns are very sensitive to the phase distribution on the antenna aperture. Beam direction, maximum gain, and the side lobe levels are strongly dependent on the aperture phase distribution. The random surface errors degrade the radiation patterns

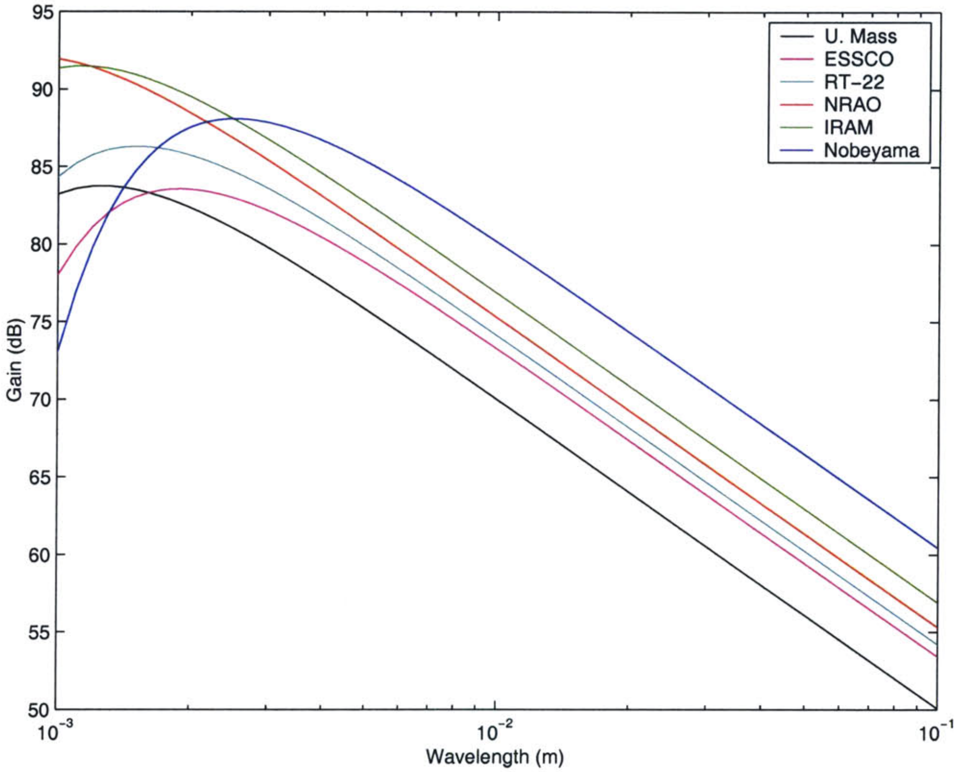

Figure 1-2: The maximum gain of some large antennas listed in Table 1.1 as a function of wavelength. The aperture efficiency η_{ap} is assumed equal to 55 % for all antennas.

largely through the introduction of random phase errors to the aperture field [11][10]. For the axially symmetric reflector antennas, the direction of the peak gain is on the axis of symmetry. If the random surface errors are uniformly distributed over the antenna surface, the direction of the maximum gain will not change because the effects from the random phase errors tend to cancel each other [18].

1.2.3 Effect on the side lobe

The average level of side lobes is a measure of how well the power is concentrated into the main lobe. The side lobe level (SLL), which is the ratio between the gain of the peak side lobe to that of the peak main lobe, is expressed by

$$SLL = 10\,log_{10}\frac{max\{G_{side\,lobe}\}}{G_{max}} \tag{1.12}$$

The design of reflector antennas usually involves tradeoff between the aperture efficiency η_{ap} and the side-lobe level. Many high-performance antennas are designed so that the amplitude of the aperture field is tapered towards the edge of the reflectors as much as possible to reduce the peak of the side lobes. However, because of the Fourier relationship between the aperture field and the far field, efforts to decrease the side lobes by tapering the aperture field may result in broader main beams, which decrease the directivity and the aperture efficiency.

Random surface errors cause the side lobes to rise on average. Research results show that reflector antennas with low SLL have a stronger requirement on the surface rms to wavelength ratio ($\varepsilon_{rms}/\lambda$) [10]. It has been found that the side lobes degrade much faster than the peak gain, and for a given manufacturing tolerance level, a considerably smaller $\varepsilon_{rms}/\lambda$ is required to keep the side lobes within the required bounds. Thus, the requirement on the maximum side lobe is likely to be a decisive factor to determine the maximum operating frequency of reflector antennas.

1.3 Effect on the beamwidth

The beamwidth is a measure of the ability to focus for reflector antennas. There are two definitions of beamwidth in common use. The first one measures the angular spread of the main lobe between the first-null positions, which is known as the first-null beamwidth. The other measures the angular spread between the half-power points of the main lobe, which is known as the half-power beamwidth. Another performance parameter related to the beamwidth is the beam efficiency of an antenna, which is defined as the ratio of power radiated in the main-beam region to the total radiated power. There are two definitions of the main beam in correspondence to the definitions of the beamwidth; one uses the first-null beamwidth, while the other uses 2.5 times the half-power beamwidth [19]. The beam efficiency is higher for reflectors with tapered aperture illumination because they have lower side lobes.

One of the effects of the random surface errors on the radiation patterns is the broadening of the main beam. In addition, The presence of random surface errors also reduce the beam efficiency [19]. The degree of reduction is largely determined by the level of the rms surface errors compared with the wavelength and the tapering of the aperture illumination.

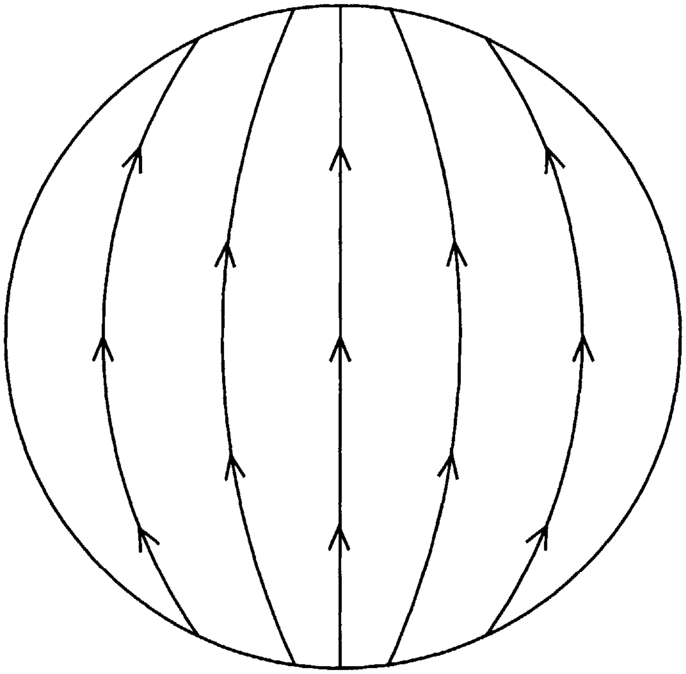

Figure 1-3: Polarization of the aperture field for a paraboloidal reflector antenna with a vertically oriented electric dipole feed.

1.3.1 Effect on the cross-polarization

The polarization describes the vector nature of electric fields radiated by an antenna. Figure 1-3 shows the polarization on the aperture field of a paraboloidal reflector with a dipole feed. The field component perpendicular to the polarization of the feed is called the cross-polarized aperture field, and the radiation resulting from it is called the cross-polarized radiation. The cross-polarized radiation will not be picked up by the receiver and will be a waste of the transmission energy. Hence, efficient antennas are designed to minimize the cross-polarized radiation. In addition, the quality of polarization is important for dual-polarized antennas, which use orthogonal polarization to provide two communication channels for each frequency band. A high level of cross-polarized radiation will degrade the quality of the orthogonal signals by mutual inteference.

For axially symmetric reflector antennas, the cross-polarized radiation field does not appear on the E-plane and the H-plane, as well as on the main axis. This is a result of two factors: (1) adjacent quadratures of the reflectors have their cross-polarization in anti-phase, and (2) the path length from the focus to the aperture plane is constant for all rays. Surface errors may increase cross-polarization level on the main axis in two ways. First, the amplitude distribution of cross-polarized components may differ in different quadrants of the aperture, and the cancellation of their contribution to the fields on axis may not be complete. Second, there will be phase variations on the aperture caused by path-length differences. If the surface errors are small, which is the case for most antennas, the amplitude errors are negligible. However, effects from the phase variations cannot be ignored.

1.4 Work in the past

The effects of random surface errors on reflector antennas have been studied since the mid 1950's. By far, the most recognized work is the antenna tolerance theory developed by J. Ruze [11] to predict changes in the average pattern as a result of random surface errors. He was among the first to use statistical approach to analyze the effect of random phase errors in the aperture of an antenna caused by the path length differences. The antenna tolerance theory states the effects of random surface errors on the average gain pattern in terms of the antenna's aperture illumination, root-mean-square surface errors, and correlation distance. The random phase errors are assumed to be Gaussian distributed with Gaussian spatial correlation function, which closely reflect the true distribution of the surface errors. The formula of the antenna tolerance theory can be reduced to a simple expression to determine the gain loss in the axial direction. For any reflector antennas, there is a wavelength at which the gain reaches a maximum. This wavelength depends on ε_{rms}, the rms deviation of the reflector surface from the ideal surface and is given by $\lambda = 4\pi\varepsilon_{rms}$.

There is an attempt to modify Ruze's work to make the statistical model and the illumination function more realistic by M. Zarghamee. He extends Ruze's analysis by relaxing the assumption that the error distribution must be uniform, which is likely to make the estimate of the gain reduction too pessimistic [15]. He assumes instead that the distribution of the rms surface error is tapered towards the rim of the reflector. However, this effect is minor if the surface deviations are not a large fraction of the operating wavelength.

D. K. Cheng took a deterministic approach to analyze the effects of random surface errors on radiation patterns [20]. He disagrees with the statistical approach where only the average behavior of a large number (an ensemble) of antennas and the average radiation pattern can be discussed. This is because the pattern of the individual antenna will differ from the average pattern. In practice, it is desirable to be able to predict the maximum effect on the gain, beamwidth, and etc., if the maximum phase error is given for an individual antenna even when the exact phase distribution is unknown. In his own work, he determines the maximum loss in the gain from the maximum phase error on the aperture of the antenna. In addition, the maximum change in the beamwidth of the main lobe can also be predicted from the slope of the radiation pattern near the half-power point and from the maximum phase error.

Y. Rahmat-Samii develops a useful mathematical model to study the degradation on the average power pattern caused by the random surface errors [10]. The analysis begins with a division of the reflector surface into annular regions. Each region is given a root-mean-square value for the deviations from the ideal position. A closed-form expression for the average radiation pattern from each ring is derived before it is used to find the average pattern for the whole reflector, which results in an efficient and time-saving computational method. The model incorporates information on the focus-to-diameter (f/D) ratio and allows non-uniform surface errors and non-uniform illumination functions. The simulation results show that reflector antennas with lower side lobe levels are more sensitive to the rms surface errors. This model has been used subsequently to study the effects of random surface errors on the beam efficiency and on the side lobe level [21][19]. It has been shown that the model could be extended to include other types of errors such as the misalignment errors in addition to the random surface errors [22].

S. I. Ghobrial studies the effect of surface imperfections on the axial cross-polarization performance of reflector antennas [18][23]. His results show that the average cross-polarization due to random surface errors is proportional to the root-mean-square error and the correlation diameter of the surface errors. In addition, it is also a function of the polarization efficiency of the antenna. The axial cross-polarization probability density is also found to be close to the Rayleigh distribution for relatively large errors. In [18], he derives expressions for the probability density and the average value of cross-polarization on the main axis. He shows that for small errors, the average on-axis cross-polarization is directly proportional to the rms surface error. For relatively large errors ($\lambda > 0.04$) the cross-polarization is proportional to the square root of $(1 - e^{-2\sigma^2})$, where σ is the rms phase errors.

V. K. Tripp presents a different approach to analyze the effects of random errors on the aperture antennas [24]. In stead of using the statistics of the phase term in the aperture field, he introduces the error as the field scattered from defects, which are randomly positioned. The defects are represented by a matrix of scattering function which can be calculated, assumed or measured. A closed-form vector expression is derived for the average power pattern in terms of the unperturbed aperture field, the scattering matrix of a defect, and the probability density function of a defect position. Some good features of this model are that the surface errors need not be small, and their distribution over the aperture is not restricted. However, the drawback seems to be that this model is not convenient for doing parametric studies due to the complexity of implementation.

1.5 Motivation

There are a few reasons to be interested in the study of effects of random surface errors on the performance of reflector antennas. The most important is its usefulness in assessing performance of antennas at various operating frequency ranges and in the specification of antenna surface accuracy during the construction or upgrade. The quantitative results of such study can be used by antenna engineers to specify the required level of manufacturing tolerance. If the manufacturing tolerances are set too loose, the reflector may not perform according to the specifications. On the other hand, the manufacturing tolerances that are set too tight may result in excessive costs [21]. As the use of microwave frequencies continues to increase, there will be a growing demand for more accurate manufacture, installation, and validation of reflector surfaces.

Almost all previous studies on the effects of random surface errors on reflector antenna performance have focused on the analysis of phase errors on the antenna aperture [11][15][10][25][26][20][27][24][23][18][21][19]. These efforts result in some useful mathematical models and closed-form formulas which are suitable for parametric studies but are often compromised with simplified assumptions on the characteristics of the error distribution and in the formulation of analysis. For instance, it has been widely accepted that the errors are distributed more or less with the Gaussian distributed height and having the Gaussian correlation function. Yet, no known computer simulation-based study in the past has incorporated this model to the full extent.

So we think the study can be improved in many areas in order to have more accurate results. A modern approach is to do a Monte Carlo simulation by generating an ensemble of instances of the random surface errors that may appear on the reflector surface and study the statistics of the radiation patterns. This approach should allow more realistic assumptions on the statistical distribution of random surface errors, which will lead to more accurate results. Furthermore, a collection of data from the simulation will enable us to understand the statistics of the performance parameters of interest in addition to the mean values.

1.6 Objective

The purpose of this project is to develop a simulation program to study the radiation patterns of paraboloidal reflector antennas whose surfaces are subjected to random errors. The emphasis of this project is on using an accurate representation of the statistics of the random surface errors, and on making the results truly reflect their presence. The program should produce the co-polarized and cross-polarized radiation patterns on three planes of observation–E-plane, H-plane and 45-degree plane. It should be flexible enough for users to change the size D, shape f/D, and feed pattern $G(\theta', \phi')$ of the paraboloidal reflector.

1.7 Approach

There are three high-frequency methods for the computation of the radiation from reflector antennas in common use: geometrical optics/aperture integration (GO/AI), physical optics/surface integration (PO/SI), and physical optics/aperture integration (PO/AI) [28]. The aperture integration methods—GO/AI and PO/AI—are the most popular methods to analyze radiation field from reflectors because they avoid integration over a non-planar surface. In GO/AI, ray tracing is used to find equivalent currents in the aperture plane based on intensity of the field in ray tubes. In PO, the induced current elements on the reflector surface are approximated to be twice the magnetic field intensity. However, the radiation integral can be performed either on the reflector surface or on the aperture plane. From the formulation, PO is potentially superior to GO because it includes axially directed surface current elements, while GO does not. In addition, PO accounts for surface normal variations as well as phase variations due to surface distortions, whereas typical application of GO only considers phase variations due to changes in path lengths.

A formulation based on geometrical optics ray-tracing will be used in this study. Geometrical optics has theoretical foundations based on Maxwell's equations [29][7]. This technique can be used to analyze reflector antennas when the size of the structures are much larger than the wavelength. When applied to the analysis of reflector antennas, solutions obtained from GO are found to agree with those obtained from other potentially superior approaches such as physical optics (PO) and geometrical theory of diffraction (GTD) up to the first few side lobes [30][31][28][32].

We assume the reflector has a point-source feed, and electromagnetic energy radiated from the feed can be thought to flow in ray cones with their bases on a spherical wave front. The ray cones will be generated in such way that they have equal solid angle, so that on a wave front, the cones will support the same amount of base area. Thus, the radiation power contained in each cone will depend only on the source's gain factor.

When the incident ray vectors hit the reflector, they will be reflected according to the law of reflection. The positions where the ray vectors intersect with the aperture plane will be recorded as well as the distances that they travel from the source to the aperture plane and the polarization of the electric field associated with them. This information will be used to calculate the radiation pattern which depends on the field distribution on the aperture plane.

By the field equivalence principle, the fields on the wave front can be replaced by an equivalent source, and we put an equivalent current sheet on the base of each ray cone. These current sheets will be substituted by a dipole with equal current moment. The location of the dipole is chosen at the centroid of the current sheet.

For the ideal paraboloidal reflector, the phase term of the aperture field distribution will be equal due to the property of parabolas. With the addition of a random rough surface, the distance that the rays must travel from the source to the aperture plane will not be the same; hence the difference in the phase term. The difference in the phase term is the main factor for the change in the radiation pattern. Other factors include changes in position of the reflected rays due to the angle of reflection and changes in amplitude of the electromagnetic field intensity for each ray.

The surface errors which appear on the reflector surface are assumed to come from the manufacturing or during the construction process. The random errors are assumed to be uniformly Gaussian in distribution and in correlation pattern, with a specified correlation length over the reflector surface. The degradation in the performance of reflectors will be quantified with respect to the root-mean-square values of the height distribution.

1.8 Scope of the project and this document

The scope of this project will be limited to the study of some performance parameters of the reflector antennas which can be determined from the radiation patterns. From the radiation pattern, we will be interested in the effects of random surface errors on the gain pattern, directivity, beamwidth, side-lobe levels, and on-axis cross-polarization. We will be concerned only in the far field because most applications assume far distance between the source and the receiver.

Throughout the project, the reflector will be assumed to have the size $D = 40\,\lambda$ and shape $f/D = 0.5$ with a linearly polarized isotropic point-source feed at the focus. In addition, we will use one value of the correlation interval for the ensemble of Gaussian random surfaces.

In our application of geometrical optics, it will be assumed that the currents on the shadow region of the reflector have negligible effects on the far-field pattern. The diffractions on the edge of the dish are also not included.

Chapter 2 begins with the theory of geometrical optics followed by an analysis of radiation field from a paraboloidal reflector based on GO and the Huygens' principle. The solution will be used to compare with the numerical results from ray tracing before it will be used to study reflectors with random surface errors. We also present results based on PO and compare them with those from GO ray tracing, along with an analysis of the maximum angle of observation where GO and PO results would agree.

Chapter 3 describes the theory and a method to create the Gaussian random surfaces to be used as the surface errors in the Monte Carlo simulation. A series of verification is made to validate the computer-generated results and to illustrate some properties of the Gaussian random surfaces.

Chapter 4 begins with the effects on the GO and PO current elements brought by the incorporation of random surface errors to a paraboloidal reflector. As a result of the Monte Carlo simulation, we present the average patterns from GO and PO in both polarizations (co-polarization and cross-polarization) on the three major planes of observation (E-plane, H-plane, and 45-degree plane). The results from GO and PO will be discussed, and compared with those from the antenna tolerance theory.

Chapter 5 contains conclusions from our study and recommendations for the future work.

Chapter 2

Analysis of radiation patterns from a paraboloidal reflector

In this chapter, we formulate a model based on ray tracing to study the radiation field from paraboloidal reflector antennas. The model is intended to be used to analyze paraboloidal reflectors with small surface errors. We begin with the fundamentals of geometrical optics (GO). Next we present an analysis of the aperture field of paraboloidal reflectors with a linearly polarized point feed based on GO. The Huygens' principle is used to find the diffracted field from the aperture field. Then we describe a scheme to produce the ray vectors, which will be used for ray tracing. A general formulation to find the radiation field from the ray vectors are derived. Several pattern plots are presented to compare between the analytical results of geometrical optics and the numerical results from ray tracing. The purpose is to verify the correctness of the formulation and its implementation on a computer program.

The last part of this chapter contains an analysis of paraboloidal reflectors based on PO.

The potential for PO to produce results with higher accuracy will be the basis for using PO-based results as our reference standard when the random surface errors are added to the reflectors.

2.1 Geometrical optics analysis of radiation patterns from a paraboloidal reflector

In this section, we derive an analytical solution to the radiation field of a paraboloidal reflector with a linearly polarized isotropic feed. We use geometrical optics to find the field distribution on the aperture plane of the reflector. Then we apply Huygens' principle to the aperture field to find the radiation field. The radiation field will be described in terms of the co-polarized and the cross-polarized radiation patterns. The appearance of these patterns will depend on the definition of the polarization reference vectors.

2.1.1 Geometrical Optics

Geometrical optics (GO) is a very high frequency approximation to solutions of Maxwell's equations [16][7][29]. Geometrical optics is very accurate for use in the design and analysis of optical devices since optical wavelengths are extremely small compared to the dimensions of optical systems. At microwave frequencies, the operating wavelengths are not always relatively small compared to the dimensions of microwave systems. However, geometrical optics remains sufficiently accurate even for antennas with dimensions as small as five wavelengths [33]. In general, geometrical optics can be used to analyze and synthesize optical and microwave systems to the approximation that diffraction and interference from the edges can be neglected.

In classical geometrical optics, the wavelength, the phase, and the polarization of the electromagnetic waves are omitted [29]. The extension of classical geometrical optics to microwave analysis includes the above factors, which can be done by using the asymptotic solution of the Maxwell's equations as $\omega \to \infty (\lambda \to 0)$. This extension consists of the following: (1) assuming a small but finite wavelength, (2) identifying the wave fronts with equiphase surfaces, and (3) assuming electromagnetic plane waves propagating along the geometrical optics rays in a homogeneous medium.

Let us consider the following plane-wave solution to the Maxwell's equations

$$\overline{E}(\bar{r}) = \overline{E} e^{ik_0 L(\bar{r})} \tag{2.1}$$

$$\overline{H}(\bar{r}) = \overline{H} e^{ik_0 L(\bar{r})} \tag{2.2}$$

where $k_0 = \omega / c$ and $k_0 \to \infty$. The phase function $L(\bar{r})$ is known as the eikonal. Substituting Equation (2.1) and Equation (2.2) into the source-free Maxwell's equations for isotropic media

$$\begin{aligned} \nabla \times \overline{E} &= i\omega\mu\overline{H} \\ \nabla \times \overline{H} &= -i\omega\epsilon\overline{E} \\ \nabla \cdot \overline{E} &= 0 \\ \nabla \cdot \overline{H} &= 0 \end{aligned} \tag{2.3}$$

and using the vector identities $\nabla \times (\overline{A}\phi) = \phi\nabla \times \overline{A} + \nabla\phi \times \overline{A}$, and $\nabla \cdot (\overline{A}\phi) = \nabla\phi \cdot \overline{A} + \phi\nabla \cdot \overline{A}$, we find

$$\begin{aligned} \nabla L(\bar{r}) \times \overline{H} + \frac{n}{\eta}\overline{E} &= \frac{i}{k_0}\nabla \times \overline{H} && (2.4) \\ \nabla L(\bar{r}) \times \overline{E} - n\eta\overline{H} &= \frac{i}{k_0}\nabla \times \overline{E} && (2.5) \\ \nabla L(\bar{r}) \cdot \overline{E} &= \frac{i}{k_0}\nabla \cdot \overline{E} && (2.6) \\ \nabla L(\bar{r}) \cdot \overline{H} &= \frac{i}{k_0}\nabla \cdot \overline{H} && (2.7) \end{aligned}$$

where $n = c\sqrt{\mu\epsilon}$ is the refractive index, and $\eta = \sqrt{\mu/\epsilon}$ is the characteristic impedance of the media.

In the high frequency limit, the right-hand sides of Equations (2.4)-(2.7) are equal to zero. The governing equations of geometrical optics are

$$\begin{aligned} \nabla L(\bar{r}) \times \overline{H} &= -\frac{n}{\eta}\overline{E} && (2.8) \\ \nabla L(\bar{r}) \times \overline{E} &= n\eta\overline{H} && (2.9) \\ \nabla L(\bar{r}) \cdot \overline{E} &= 0 && (2.10) \\ \nabla L(\bar{r}) \cdot \overline{H} &= 0 && (2.11) \end{aligned}$$

Note that Equations (2.8)-(2.11) are independent of frequency. Substituting Equation (2.9) into Equation (2.8) and making use of Equation (2.10), we obtain the eikonal equation in geometrical optics

$$|\nabla L(\bar{r})|^2 = n^2 \qquad (2.12)$$

The wave fronts are described by letting $L(\bar{r})$ equal to a constant. The vector $\nabla L(\bar{r})$ evaluated at any point in space is always normal to the wave front passing through it. From Equation (2.12), we have

$$\nabla L = \hat{s} n \tag{2.13}$$

where $\hat{s}$ is the unit normal to the wave front. The vector $\hat{s}n$ is called the ray vector. From Equation (2.10) and Equation (2.11), the electric and magnetic fields at each point on a ray are always perpendicular to the ray. The time-average Poynting's vector is expressed by

$$\begin{aligned} < \bar{S} > &= \frac{1}{2} Re\{\bar{E} \times \bar{H}^*\} = \frac{1}{2n\eta} Re\{\bar{E} \times (\nabla L \times \bar{E})^*\} \\ &= \frac{1}{2n\eta} (\bar{E} \cdot \bar{E}^*) \nabla L \\ &= \hat{s} \frac{1}{2\eta} |\bar{E}|^2 \end{aligned} \tag{2.14}$$

The Poynting's vector has a unit of W/m^2 and can be viewed as the power density per unit area along the ray vector.

In order to trace geometrical optics rays through a system, it is necessary to know the behavior of the rays in the media and at the boundaries. Let $\bar{r}(s)$ be the position vector along a ray path in terms of the arc length parameter s. Since $d\bar{r}/ds = \hat{s}$, we find from Equation (2.13)

$$\frac{d^2\bar{r}}{ds^2} = \frac{d\bar{r}}{ds} \cdot \nabla (\frac{d\bar{r}}{ds}) = \hat{s} \cdot \nabla (\hat{s}) = \frac{\nabla L}{n} \cdot \nabla (\frac{\nabla L}{n}) \tag{2.15}$$

For homogeneous media in which n is a constant, we find from Equation (2.12) and

Equation (2.15)

$$\frac{d^2\bar{r}}{ds^2} = \frac{1}{2}\nabla(\frac{|\nabla L|^2}{n^2}) = 0 \tag{2.16}$$

Thus the ray path is a straight line in homogeneous media.[1]

Next we derive Snell's law from the solutions of geometrical optics. Snell's law governs the behavior of rays at the boundaries between two media. We integrate Equation (2.13) around a ribbon-like contour across the boundary separating two media with indices n_1 and n_2 as shown in Figure 2-1.

Applying Stoke's theorem and letting the ribbon width $\delta \rightarrow 0$, we have

$$\iint d\overline{S} \cdot \nabla \times (\hat{s}n) = \oint_C d\bar{l} \cdot \hat{s}n = 0 \tag{2.17}$$

where $d\overline{S}$ is the unit vector perpendicular to the ribbon area, and $d\bar{l}$ is the differential line element along the closed contour of the ribbon. The contributions to the integral from the two sides of the ribbon perpendicular to the surface are negligible because they are proportional to the vanishing δ. Thus, the tangential components of the ray vectors are continuous across the boundary. For the transmitted ray, we find from Equation (2.17)

$$n_1 \sin\theta_i = n_2 \sin\theta_t \tag{2.18}$$

---

[1] The ray path can also be determined from Fermat's principle. The optical path length along a ray path C is defined as the line integral $\int_C nds$, where n is the index of refraction of the medium and s is the arc length along C. Fermat's principle states that electromagnetic energy travelling between two points will follow any ray path that makes the integral stationary. In a homogeneous medium, ray paths will be straight lines.

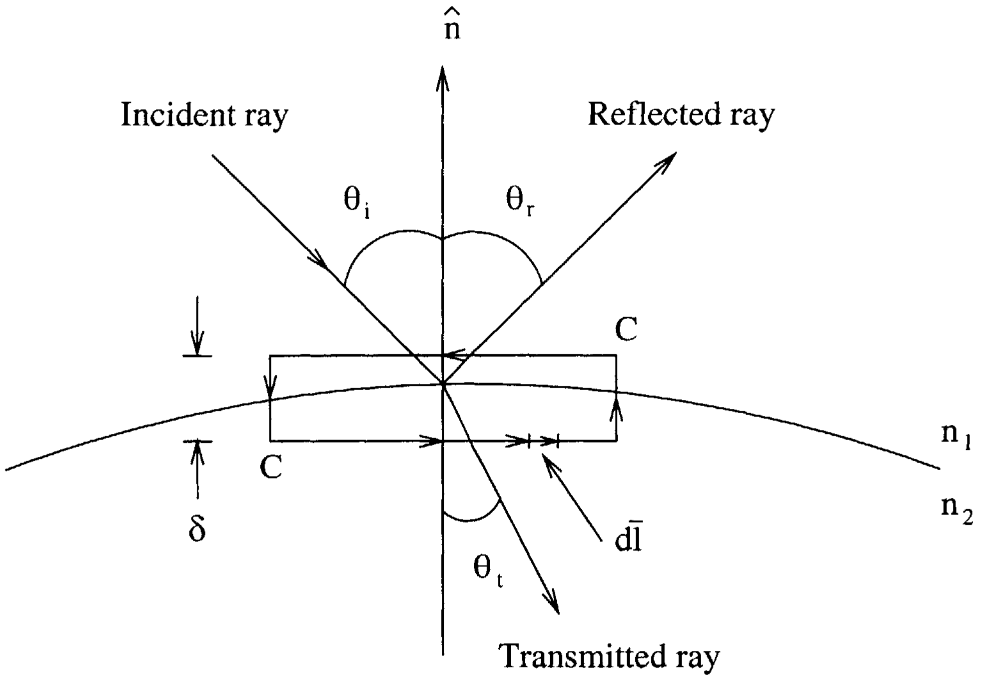

Figure 2-1: Derivation of Snell's law using geometrical optics.

For the reflected ray, we use $\theta_t = \pi - \theta_r$ and $n_2 = n_1$. From Equation (2.18), we find $n_1 \sin\theta_i = n_1 \sin\theta_r$. Thus the angle of reflection θ_r is equal to the angle of incidence θ_i. This derivation is valid as long as the radii of curvature of the incident wave and of the boundary surface are large compared to the wavelength [7].

2.1.2 Aperture field of paraboloidal reflectors

In this section, we use geometrical optics to find the aperture field of a paraboloidal reflector antenna with a linearly polarized point feed at the focus. The assumption that the source is a point radiator is justified if the main reflector is in the far field of the feed [16]. In the far field, any current distribution reduces to a point source or can be described adequately in terms of wave fronts and rays. We shall assume that wave fronts from the source are concentric

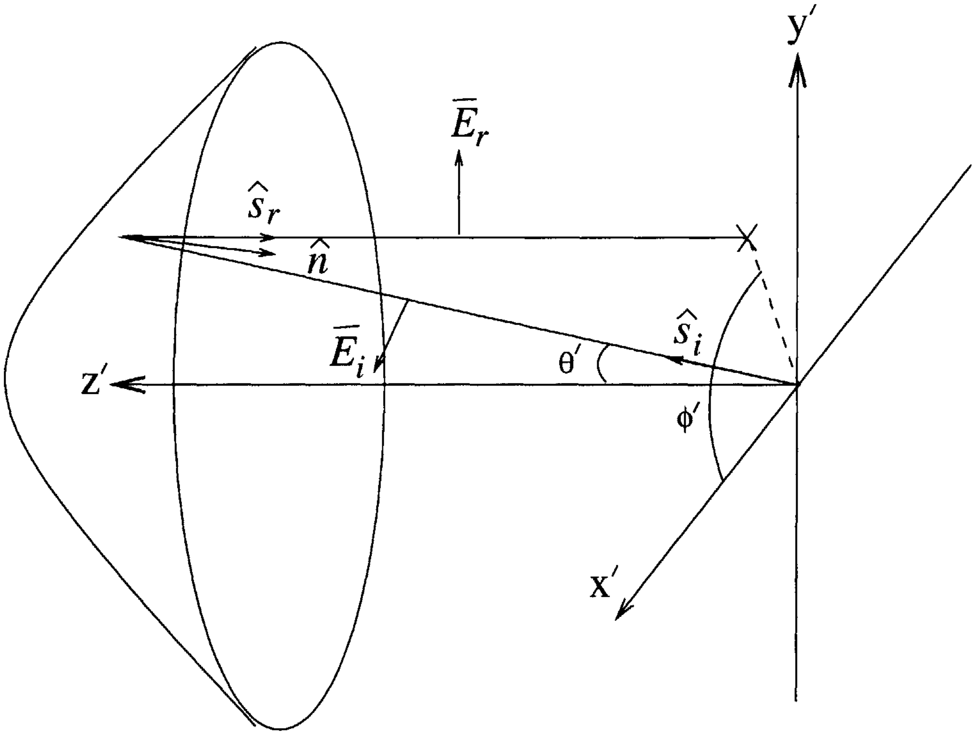

Figure 2-2: Geometrical optics analysis of the aperture field of a paraboloidal reflector.

spherical with the center at the source point. Figure 2-2 displays the ideal paraboloidal reflector, which is described by

$$r' = f\sec^2\frac{\theta'}{2} \qquad 0 \le \theta' \le \theta'_0 \tag{2.19}$$

where r' is the distance from the origin to the surface of the paraboloid, f is the focal length, and θ'_0 is the angle between the main axis and the rim of the paraboloid. $\overline{E}_i$ and $\overline{E}_r$ are the incident and the reflected electric fields respectively. The vectors $\hat{s}_i$ and $\hat{s}_r$ denote the incident and the reflected ray vectors.

Assuming there is a point-source feed located at the focus. The incident electric field vector on the paraboloidal surface at a distance r' from the focal point is

$$\overline{E}_i = \hat{e}_i\, E(\theta', \phi')\frac{e^{i\omega r'/c}}{r'} \tag{2.20}$$

The amplitude $E(\theta', \phi')$ is related to the gain factor $G(\theta', \phi')$ of the source by

$$\frac{1}{2\eta}|E(\theta', \phi')|^2 = \frac{P_t}{4\pi}G(\theta', \phi') \tag{2.21}$$

where P_t is the total power radiated by the source.

We will assume that the point source at the focus is y'-polarized. The polarization of the incident wave, which is specified by the unit vector $\hat{e}_i$, is given by

$$\hat{e}_i = \frac{\hat{r}' \times (\hat{y}' \times \hat{r}')}{|\hat{r}' \times (\hat{y}' \times \hat{r}'|)} = \frac{\hat{y}' - (\hat{r}' \cdot \hat{y}')\hat{r}'}{|\hat{y}' - (\hat{r}' \cdot \hat{y}')\hat{r}'|} \tag{2.22}$$

We find $\hat{e}_i$ in rectangular coordinates by a substitution of $\hat{r}' = \hat{x}' \sin\theta' \cos\phi' + \hat{y}' \sin\theta' \sin\phi' + \hat{z}' \cos\theta'$ into Equation (2.22), which gives

$$\begin{aligned} \hat{e}_i &= \frac{1}{\sqrt{1-\sin^2\theta' \sin^2\phi'}} \{-\hat{x}' \sin^2\theta' \sin\phi' \cos\theta' \\ &\quad + \hat{y}' (1-\sin^2\theta' \sin^2\phi') - \hat{z}' \sin\theta' \cos\theta' \sin\phi'\} \end{aligned} \tag{2.23}$$

The reflected electric field $\overline{E}_r$ is determined from $\overline{E}_i$ and $\hat{n}$, the unit normal vector to the paraboloidal surface, by using the following electromagnetic boundary conditions

$$\hat{n} \times (\overline{E}_r + \overline{E}_i) = 0 \tag{2.24}$$

$$\hat{n} \cdot \overline{E}_i = \hat{n} \cdot \overline{E}_r \tag{2.25}$$

Equation (2.24) states that the tangential electric fields vanish at the reflector surface, which is assumed a perfect conductor. Equation (2.25) states the continuity between $\overline{E}_i$ and $\overline{E}_r$. Cross-multiplying Equation (2.24) by $\hat{n}$ and making use of Equation (2.25), we find

$$\overline{E}_r = 2\hat{n}(\hat{n} \cdot \overline{E}_i) - \overline{E}_i = \hat{e}_r \, E(\theta', \phi') \frac{e^{i\omega r'/c}}{r'} \tag{2.26}$$

The unit vector $\hat{e}_r$, which is the polarization of the reflected wave, is given by

$$\hat{e}_r = 2\hat{n}(\hat{n} \cdot \hat{e}_i) - \hat{e}_i \tag{2.27}$$

In order to find $\hat{e}_r$, we begin with the unit normal to the reflector surface $\hat{n}$. Taking the gradient of Equation (2.19), we find the normal vector to the reflector surface

$$\nabla[f - r'\cos^2\frac{\theta'}{2}] = \hat{r}'\cos^2\frac{\theta'}{2} + \hat{\theta}'\sin\frac{\theta'}{2}\cos\frac{\theta'}{2} \tag{2.28}$$

Normalizing the above expression by $-\cos(\theta'/2)$ and using the following transformation of vectors from the spherical to the rectangular coordinate systems

$$\hat{r} = \hat{x}\sin\theta\cos\phi + \hat{y}\sin\theta\sin\phi + \hat{z}\cos\theta \tag{2.29}$$

$$\hat{\theta} = \hat{x}\cos\theta\cos\phi + \hat{y}\cos\theta\sin\phi - \hat{z}\sin\theta \tag{2.30}$$

$$\hat{\phi} = -\hat{x}\sin\theta + \hat{y}\cos\theta \tag{2.31}$$

we find

$$\hat{n} = -\hat{x}'\,\sin\frac{\theta'}{2}\cos\phi' - \hat{y}'\,\sin\frac{\theta'}{2}\sin\phi' - \hat{z}'\,\cos\frac{\theta'}{2} \tag{2.32}$$

Note that the vector $\hat{n}$ above points toward the concave side of the paraboloid. The polarization vector $\hat{e}_r$ of the reflected wave is determined from Equations (2.23), (2.27), and (2.32)

$$\hat{e}_r = \frac{1}{\sqrt{1 - \sin^2\theta'\sin^2\phi'}}\{\hat{x}'\,(1 - \cos\theta')\sin\phi'\cos\phi' - \hat{y}'\,(\cos\theta'\sin^2\phi' + \cos^2\phi')\} \tag{2.33}$$

The incident ray vector $\hat{s}_i$ is the same as the position vector $\hat{r}'$ and is expressed by

$$\hat{s}_i = \hat{x}'\sin\theta'\cos\phi' + \hat{y}'\sin\theta'\sin\phi' + \hat{z}'\cos\theta' \tag{2.34}$$

The reflected ray vector $\hat{s}_r$ is determined from the following vector equations

$$\hat{n} \times (\hat{s}_i - \hat{s}_r) = 0 \tag{2.35}$$

$$\hat{n} \cdot \hat{s}_i = \hat{n} \cdot \hat{s}_r \tag{2.36}$$

Equation (2.35) states that the three vectors—$\hat{s}_i$, $\hat{s}_r$, and $\hat{n}$—lie on the same plane. Equation (2.36) is the Snell's law of reflection in vector form. We cross-multiply Equation (2.35) by $\hat{n}$ and make use of Equation (2.36) to obtain

$$\hat{s}_r = \hat{s}_i - 2\hat{n}(\hat{n} \cdot \hat{s}_i) \tag{2.37}$$

From Equation (2.32) and Equation (2.34), we find that $\hat{n} \cdot \hat{s}_i = -\cos(\theta'/2)$ and $2\hat{n}(\hat{n} \cdot \hat{s}_i) = \hat{x}'\sin\theta'\cos\phi' + \hat{y}'\sin\theta'\sin\phi' + \hat{z}'2\cos^2(\theta'/2)$. Hence, $\hat{s}_r$ can be expressed in rectangular coordinates as

$$\hat{s}_r = -\hat{z}' \tag{2.38}$$

So the reflected rays are parallel to the axis of symmetry of the paraboloid. Equation (2.38) agrees with Equation (2.33), which shows no $\hat{z}'$-polarized component for the reflected wave.

We obtain the electric field at the aperture plane from Equation (2.26) and Equation (2.27)

$$\overline{E}_{ap} = \hat{e}_r E(\theta', \phi') \frac{e^{ik(r' + r'\cos\theta')}}{r'} = \hat{e}_r E(\theta', \phi') \frac{e^{i2kf}}{r'} \tag{2.39}$$

The phase term of $\overline{E}_{ap}$ increases from that of $\overline{E}_r$ in Equation (2.26) by $kr'\cos\theta'$, where $k = \omega/c$. The increment is due to the extra distance that the reflected rays must travel from the reflector surface to the aperture plane. The magnitude of $\overline{E}_{ap}$ equals the magnitude of $\overline{E}_r$ on the reflector surface because the reflected rays are parallel to the axis of the paraboloid, making the power density per unit area unchanged. The aperture field is composed of the co-polarized and cross-polarized components. The co-polarized component is the field component which is parallel to the polarization of the feed ($\hat{y}'$ in this case), while the cross-polarized component is in the perpendicular direction. The cross-polarized component comes from the x' component of $\hat{e}_r$, which is caused by the curvature of the paraboloidal surface.

If the feed is isotropic, $E(\theta', \phi')$ will be uniform in all directions. From Equations (2.39) and (2.33), the co-polarized component of $\overline{E}_{ap}$ is symmetrical around the x'-axis ($\phi' = 0$) and y'-axis ($\phi' = \pi/2$). The cross-polarized component of $\overline{E}_{ap}$ is symmetrical around the $\phi' = \pi/4$ and $\phi' = 3\pi/4$ lines, and anti-symmetrical around the x'-axis and y'-axis. This information will be useful in the discussion about the radiation patterns of the reflector in the next section.

In the above analysis, we made two assumptions regarding the application of GO. First, there is no surface current on the shadow side of the reflector. Second, the discontinuity in the surface current at the edge of the reflector is negligible; hence, there will be no edge effect. These assumptions usually restrict the accuracy of the radiation pattern to the main beam and the first few side lobes [34][35]. The pattern in the far side lobe region can be determined more accurately by including diffraction from the rim of the reflector. This can be done by an augmentation of diffraction effects to the results of GO using the geometrical theory of diffraction (GTD) [6][36][29].

2.1.3 Radiation field from the aperture distribution

Once the field on the aperture is obtained, the field in the forward direction can be found from Huygens' principle. The aperture field $\overline{E}_{ap}$ can be thought of as a plane wave hitting a screen made of perfect conductor with an open circular slit, making the field zero everywhere except on the aperture area. The aperture field contains the tangential components of electromagnetic fields on the surface of a large volume in free space which contains the point of observation. The geometry for finding the radiation field from the aperture field of a paraboloidal reflector is shown in Figure 2-3.

The Huygens' Principle

Huygens' principle states that the field solution in a region V' is completely determined by the tangential field specified over the surface S' enclosing V'. In mathematical terms, Huygens' principle expresses the fields at an observation point in terms of fields at the boundary surface. Consider a hypothetical surface S' enclosing a radiating source. The region V' is the volume bounded between S' and a spherical surface with an infinite radius. The electromagnetic field outside the surface S' is [7]

$$\overline{E}(\overline{r}) = \iint_{S'} dS' \, \{ i\omega\mu \overline{\overline{G}}(\overline{r}, \overline{r}') \cdot [\hat{n} \times \overline{H}(\overline{r}')] + \nabla \times \overline{\overline{G}}(\overline{r}, \overline{r}') \cdot [\hat{n} \times \overline{E}(\overline{r}')] \} \tag{2.40}$$

$$\overline{H}(\overline{r}) = \iint_{S'} dS' \, \{ -i\omega\epsilon \overline{\overline{G}}(\overline{r}, \overline{r}') \cdot [\hat{n} \times \overline{E}(\overline{r}')] + \nabla \times \overline{\overline{G}}(\overline{r}, \overline{r}') \cdot [\hat{n} \times \overline{H}(\overline{r}')] \} \tag{2.41}$$

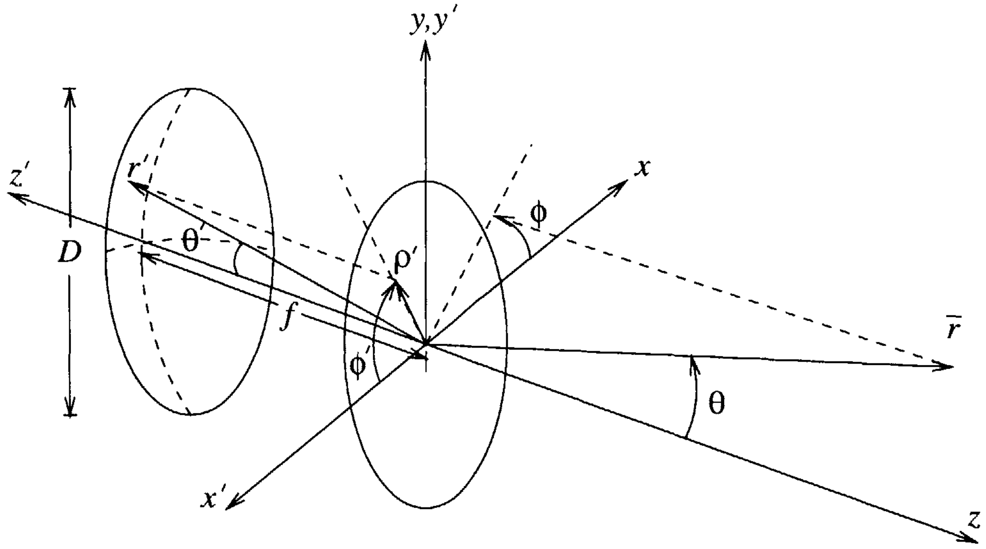

Figure 2-3: Geometry used for finding the radiation field from the aperture field of a paraboloidal reflector antenna. The primed coordinates are used for the analysis of the reflector's aperture field.

where $\hat{n}$ is the outward normal to the surface S', and $\overline{\overline{G}}(\overline{r}, \overline{r}')$ is the three-dimensional dyadic Green's function given by

$$\overline{\overline{G}}(\overline{r}, \overline{r}') = \left[\overline{\overline{I}} + \frac{1}{k^2}\nabla\nabla\right] \frac{e^{ik|\overline{r}-\overline{r}'|}}{4\pi|\overline{r}-\overline{r}'|} \tag{2.42}$$

The del operator ∇ in Equation (2.42) is given by

$$\nabla = \hat{r}\frac{\partial}{\partial r} + \hat{\theta}\frac{1}{r}\frac{\partial}{\partial \theta} + \hat{\phi}\frac{1}{r\sin\theta}\frac{\partial}{\partial \phi} \tag{2.43}$$

Note that $\overline{E}(\overline{r})$ in Equation (2.40) is expressed in terms of the tangential electric and magnetic field components at the surface S'.

Consider the diffraction of a plane wave normally incident on an aperture in an infinite conducting plane. So the fields are zero everywhere on the other side of the screen except on the aperture area. At the aperture we use the equivalence principle[2] to assume a magnetic current sheet with $\overline{M}_s = -2\hat{n} \times \overline{E}$ and no electric current sheet.[3] From the Huygens' principle,

$$\overline{E}(\overline{r}) = \iint_{S'} dS' \left\{ i\omega\mu\overline{\overline{G}}(\overline{r}, \overline{r}') \cdot \overline{J}_s(\overline{r}') - \nabla \times \overline{\overline{G}}(\overline{r}, \overline{r}') \cdot \overline{M}_s(\overline{r}') \right\} \tag{2.44}$$

$$\overline{H}(\overline{r}) = \iint_{S'} dS' \left\{ -i\omega\epsilon\overline{\overline{G}}(\overline{r}, \overline{r}') \cdot \overline{M}_s(\overline{r}') + \nabla \times \overline{\overline{G}}(\overline{r}, \overline{r}') \cdot \overline{J}_s(\overline{r}') \right\} \tag{2.45}$$

---

[2] When we are interested in a limited region of space, we can replace all uninteresting regions outside this space by using equivalent sources. The equivalent sources can be placed in the uninteresting regions or on the boundaries of the region of interest. The equivalent sources are not unique and can be constructed in many different ways.

[3] Alternatively we may use the following equivalent sources: (1) an electric current sheet $\overline{J}_s = \hat{n} \times \overline{H}$ and a magnetic current sheet $\overline{M}_s = -\hat{n} \times \overline{E}$ or (2) an electric current sheet with $\overline{J}_s = 2\hat{n} \times \overline{H}$ and no magnetic current sheet.

we find

$$
\begin{aligned}
\overline{E}(\overline{r}) &= 2\iint_{S'} dS' \nabla \times \overline{\overline{G}}(\overline{r},\overline{r}') \cdot [\hat{n} \times \overline{E}(\overline{r}')] \\
&= 2\nabla \times \iint_{S'} dS' \, \hat{n} \times \overline{\overline{G}}(\overline{r},\overline{r}') \cdot \overline{E}(\overline{r}') \\
&= 2\nabla \times \iint_{S'} dS' \, \hat{n} \times \overline{E}(\overline{r}') \frac{e^{ik|\overline{r}-\overline{r}'|}}{4\pi|\overline{r}-\overline{r}'|} \qquad (2.46)
\end{aligned}
$$

When the observation point is very far from the aperture, the diffracted field is equivalent to the radiation field due to an aperture antenna with a surface current distribution. In the radiation zone, the observation points are so remote from the aperture that all wave vectors originating from the aperture are essentially parallel. This condition allows the radiation field approximation $k|\overline{r}-\overline{r}'| \approx kr - \bar{k} \cdot \overline{r}'$. Using this approximation, the electric field in Equation (2.46) becomes

$$
\begin{aligned}
\overline{E}(\overline{r}) &\approx 2\nabla \times \frac{e^{ikr}}{4\pi r} \iint_{S'} dS' \hat{n} \times \overline{E}(\overline{r}') e^{-i\bar{k}\cdot\overline{r}'} \\
&= \frac{ie^{ikr}}{2\pi r} \bar{k} \times \iint_{S'} dS' \, \hat{n} \times \overline{E}(\overline{r}') e^{-i\bar{k}\cdot\overline{r}'} \qquad (2.47)
\end{aligned}
$$

where we replace the del operator ∇ by $i\bar{k}$ in the last step.[4]

---

[4] In Equation (2.47), the del operator

$$
\nabla = \hat{r}\frac{\partial}{\partial r} + \hat{\theta}\frac{1}{r}\frac{\partial}{\partial \theta} + \hat{\phi}\frac{1}{r\sin\theta}\frac{\partial}{\partial \phi}
$$

operates on the product of $\frac{e^{ikr}}{4\pi r}$ and the surface integral term. The operator $\frac{\partial}{\partial r}$ gives ik when operated on e^{ikr} which yields a term of the order of $1/r$ to the final solution. All other terms of the del operator yield terms of the order of $(1/r)^2$ or higher. In the far field, $kr \gg 0$, and only the terms of the order of $1/r$ are kept. So in this case we can replace ∇ by $i\bar{k}$.

Application of Huygens' principle to the aperture field

From previous analysis, the aperture field of a paraboloidal reflector can be expressed by

$$\overline{E}_{ap} = \hat{e}_r E(\theta', \phi') \frac{e^{-i(\omega/c)(r'+r'\cos\theta')}}{r'} \qquad 0 \le \theta' \le \theta'_0 \tag{2.48}$$

where $r' = f\sec^2(\theta'/2)$, and $\hat{e}_r = \dfrac{1}{\sqrt{1-\sin^2\theta'\sin^2\phi'}}\{\hat{x}'(1-\cos\theta')\sin\phi'\cos\phi' - \hat{y}'(\cos\theta'\sin^2\phi' + \cos^2\phi')\}$. Note that $\overline{E}_{ap}$ is completely described in terms of the angular parameters θ' and ϕ'. We can think of $\overline{E}_{ap}$ as a result of a normally incident plane wave on a screen made of perfect conductor with a circular aperture on it. We apply Huygens' principle to $\overline{E}_{ap}$ to find the radiation field from the aperture field as we would for a diffraction problem. From Equation (2.47)

$$\begin{aligned}
\overline{E}(\overline{r}) &= \frac{ie^{ikr}}{2\pi r}\overline{k} \times \iint_{A'} dA'\,\hat{n} \times \overline{E}_{ap} e^{-i\overline{k}\cdot\overline{\rho}'} \\
&= \frac{ie^{ikr}}{2\pi r}\overline{k} \times \iint_{A'} dA'\,\hat{n} \times \{\hat{x}'\,(\hat{x}'\cdot\overline{E}_{ap}) + \hat{y}'\,(\hat{y}'\cdot\overline{E}_{ap})\}e^{-i\overline{k}\cdot\overline{\rho}'} \\
&= \frac{ie^{ikr}}{2\pi r}\overline{k} \times \iint_{A'} dA'\,\hat{z} \times \{-\hat{x}\,(\hat{x}'\cdot\overline{E}_{ap}) + \hat{y}\,(\hat{y}'\cdot\overline{E}_{ap})\}e^{-i\overline{k}\cdot\overline{\rho}'} \\
&= \frac{ie^{ikr}}{2\pi r}\overline{k} \times \iint_{A'} dA'\,(-\hat{x}F_y + \hat{y}F_x)
\end{aligned} \tag{2.49}$$

where

$$F_x = -\iint_{A'} dA'\,(\hat{x}'\cdot\overline{E}_{ap})e^{-i\overline{k}\cdot\overline{\rho}'} \tag{2.50}$$

$$F_y = \iint_{A'} dA'\,(\hat{y}'\cdot\overline{E}_{ap})e^{-i\overline{k}\cdot\overline{\rho}'} \tag{2.51}$$

and dA' denotes the differential area on the aperture. F_x and F_y are the contributions to the radiation field from the cross-polarized and co-polarized components of the aperture field respectively. In the derivation of Equation (2.55), we replace $\hat{n}$ by $\hat{z}$ and use the fact that x and x' point to the opposite directions.

We substitute into Equation (2.49) $\overline{k} = \hat{x}k\sin\theta\cos\phi + \hat{y}k\sin\theta\sin\phi + \hat{z}k\cos\theta$ and $\bar{\rho}' = -\hat{x}\rho'\cos\phi' + \hat{y}\rho'\sin\phi'$ and use the transformation of vectors from the spherical to the rectangular coordinate system

$$\begin{aligned} \hat{x} &= \hat{r}\sin\theta\cos\phi + \hat{\theta}\cos\theta\cos\phi - \hat{\phi}\sin\phi && (2.52) \\ \hat{y} &= \hat{r}\sin\theta\sin\phi + \hat{\theta}\cos\theta\sin\phi + \hat{\phi}\cos\phi && (2.53) \\ \hat{z} &= \hat{r}\cos\theta - \hat{\theta}\sin\theta && (2.54) \end{aligned}$$

to obtain $\overline{E}(\bar{r})$ expressed in spherical coordinates

$$\begin{aligned} \overline{E}(\bar{r}) &= \frac{ie^{ikr}}{2\pi r}\{(\hat{x}k\sin\theta\cos\phi + \hat{y}k\sin\theta\sin\phi + \hat{z}k\cos\theta) \times (-\hat{x}F_y + \hat{y}F_x)\} \\ &= \frac{ike^{ikr}}{2\pi r}\{-\hat{x}F_x\cos\theta - \hat{y}F_y\cos\theta + \hat{z}(F_x\sin\theta\cos\phi + F_y\sin\theta\sin\phi)\} \\ &= \frac{ike^{ikr}}{2\pi r}\{\hat{\theta}(-F_x\cos\phi - F_y\sin\phi) + \hat{\phi}(F_x\cos\theta\sin\phi - F_y\cos\theta\cos\phi)\} \qquad (2.55) \end{aligned}$$

where

$$F_x = \iint_{A'} d\rho' d\phi'\, \rho'(\hat{x}' \cdot \overline{E}_{ap})e^{ik\rho'\sin\theta\cos(\phi+\phi')} \qquad (2.56)$$

$$F_y = \iint_{A'} d\rho' d\phi'\, \rho'\,(\hat{y}' \cdot \overline{E}_{ap})e^{ik\rho'\sin\theta\cos(\phi+\phi')} \qquad (2.57)$$

Polarization of the radiation field

Since our feed is linearly polarized, it should be easy to determine the co-polarized and the cross-polarized radiation fields. However, there are more than one way to define the directions of the co-polarization and cross-polarization reference vectors. Our choice of polarization reference vectors corresponds to the second definition of polarization proposed by A. Ludwig [37], which is illustrated in Figure 2-4b along with two other alternatives. This definition is chosen because the polarization vectors are always tangential to a spherical surface (and hence the radiation field) and because it is simple to understand. In addition, this definition is the most convenient in comparing between the calculated and the measured patterns [35].

The polarization unit vectors are defined in a system of coordinates x_1, y_1, z_1 which is related to the original system x, y, z by $x_1 = x$, $y_1 = z$ and $z_1 = -y$. For a feed which is linearly polarized along the y'-axis of the feed coordinate system, the co-polarization vector $\hat{i}_{co}$ and the cross-polarization vector $\hat{i}_{cr}$ are given by

$$\begin{aligned}
\hat{i}_{co} &\equiv \hat{\theta}_1 \\
&= \frac{1}{\sqrt{1-\sin^2\theta\sin^2\phi}}\{-\hat{x}\sin^2\theta\sin\phi\cos\phi \\
&\quad +\hat{y}(1-\sin^2\theta\sin^2\phi) - \hat{z}\sin\theta\cos\theta\sin\phi\} \\
&= \frac{1}{\sqrt{1-\sin^2\theta\sin^2\phi}}\{\hat{\theta}\cos\theta\sin\phi + \hat{\phi}\cos\phi\} \qquad (2.58)
\end{aligned}$$

$$\begin{aligned}
\hat{i}_{cr} &\equiv -\hat{\phi}_1 \\
&= \frac{1}{\sqrt{1-\sin^2\theta\sin^2\phi}}\{\hat{x}\cos\theta - \hat{z}\sin\theta\cos\phi\} \\
&= \frac{1}{\sqrt{1-\sin^2\theta\sin^2\phi}}\{\hat{\theta}\cos\phi - \hat{\phi}\cos\theta\sin\phi\} \qquad (2.59)
\end{aligned}$$

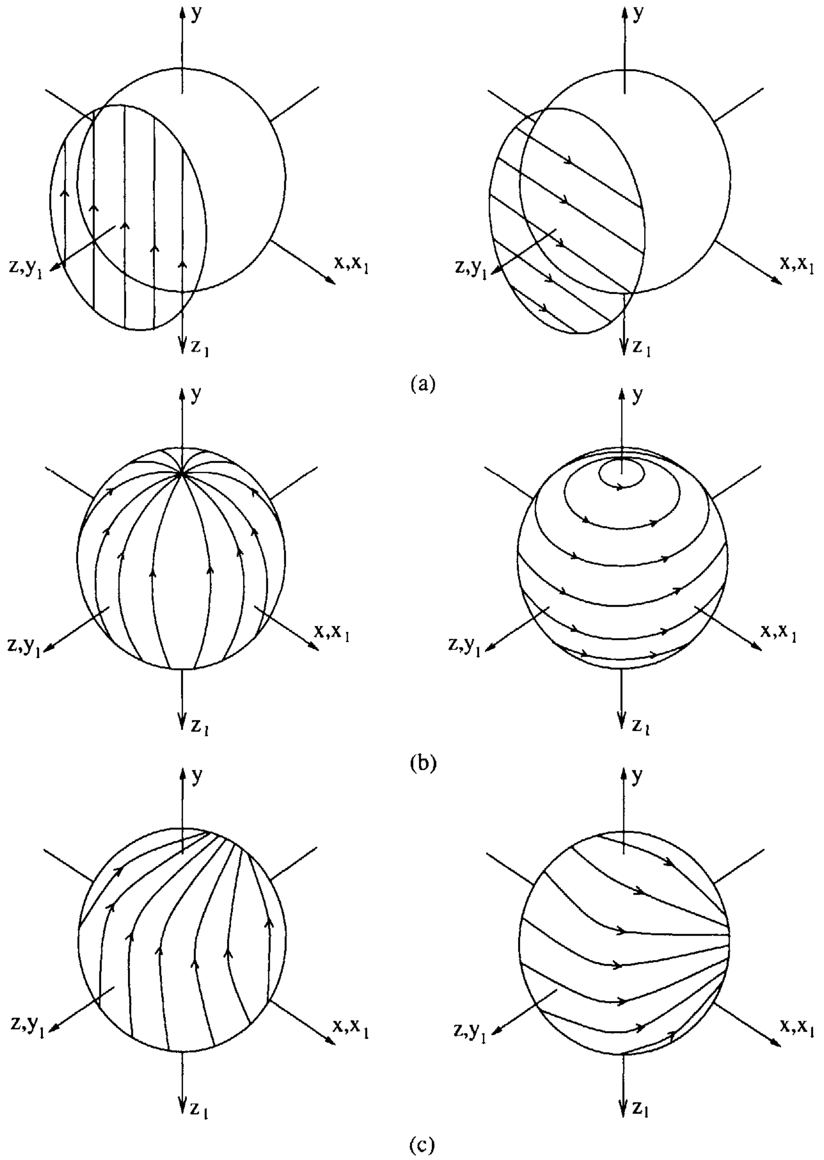

Figure 2-4: Three definitions of polarization. (a) In a rectangular coordinate system, one unit vector is taken as the direction of co-polarization, and another for cross-polarization. (b) In a spherical coordinate system, unit vectors tangential to a spherical surface are used. (c) The polarization vectors are defined according to the field measurement system. (Left: directions of the reference polarization. Right: directions of the cross polarization.) The co-polarization and cross-polarization reference vectors are perpendicular to each other at any points of observation.

The radiation field can be decomposed into the co-polarized and cross-polarized terms as follow

$$\overline{E}(\bar{r}) = \overline{E}_{co} + \overline{E}_{cr} \tag{2.60}$$

where $\overline{E}_{co} = (\overline{E}(\overline{r}) \cdot \hat{i}_{co})\hat{i}_{co}$, and $\overline{E}_{cr} = (\overline{E}(\overline{r}) \cdot \hat{i}_{cr})\hat{i}_{cr}$. The resulting co-polarized and cross-polarized components of the radiation fields are

$$\begin{aligned}
E_{co} &= \overline{E}(\overline{r}) \cdot \hat{i}_{co} \\
&= \frac{ike^{ikr}}{2\pi r}\frac{1}{\sqrt{1-\sin^2\theta\sin^2\phi}}\{(-F_x\cos\phi - F_y\sin\phi)\cos\theta\sin\phi \\
&\quad +(F_x\cos\theta\sin\phi - F_y\cos\theta\cos\phi)\cos\phi\} \\
&= -\frac{ike^{ikr}}{2\pi r}\frac{1}{\sqrt{1-\sin^2\theta\sin^2\phi}}F_y\cos\theta &(2.61) \\
E_{cr} &= \overline{E}(\overline{r}) \cdot \hat{i}_{cr} \\
&= \frac{ike^{ikr}}{2\pi r}\frac{1}{\sqrt{1-\sin^2\theta\sin^2\phi}}\{(-F_x\cos\phi - F_y\sin\phi)\cos\phi \\
&\quad +(-F_x\cos\theta\sin\phi + F_y\cos\theta\cos\phi)\cos\theta\sin\phi\} \\
&= \frac{ike^{ikr}}{2\pi r}\frac{1}{\sqrt{1-\sin^2\theta\sin^2\phi}}\{-F_x(1-\sin^2\theta\sin^2\phi) \\
&\quad -F_y\sin^2\theta\sin\phi\cos\phi\} &(2.62)
\end{aligned}$$

where Fx and Fy are expressed by Equations (2.56) and (2.57) respectively.

Figure 2-5 and Figure 2-6 show the radiation patterns for a paraboloidal reflector with diameter size $D = 40\,\lambda$ and with the focus-to-diameter ratio $f/D = 0.5$. The feed is isotropic ($G(\theta', \phi') = 1$) and y'-polarized. Figure 2-5 shows the radiation patterns on the principal E-plane and H-plane, where $\phi = \pi/2$ and $\phi = 0$ respectively. We display only one side of the

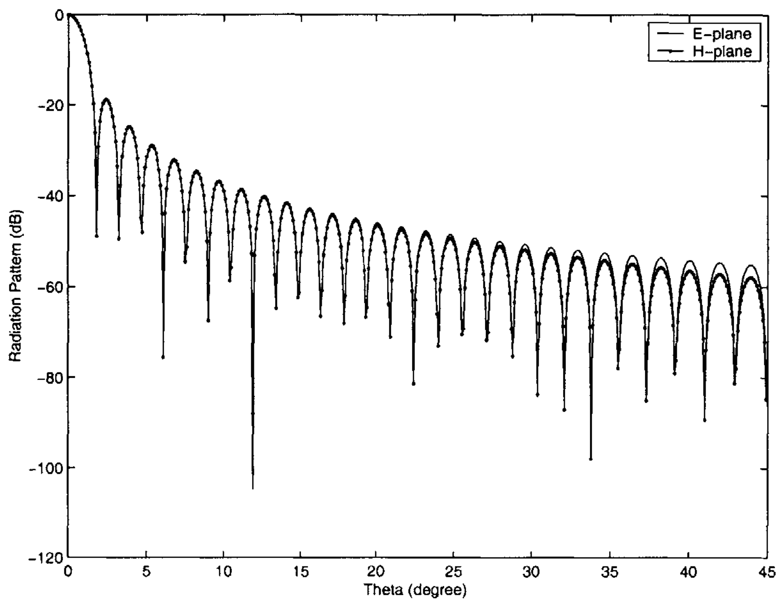

Figure 2-5: Co-polarized radiation patterns on the principal E-plane and H-plane for a paraboloidal reflector (D = $40\,\lambda$, $f/D = 0.5$) with a linearly polarized isotropic feed at the focus.

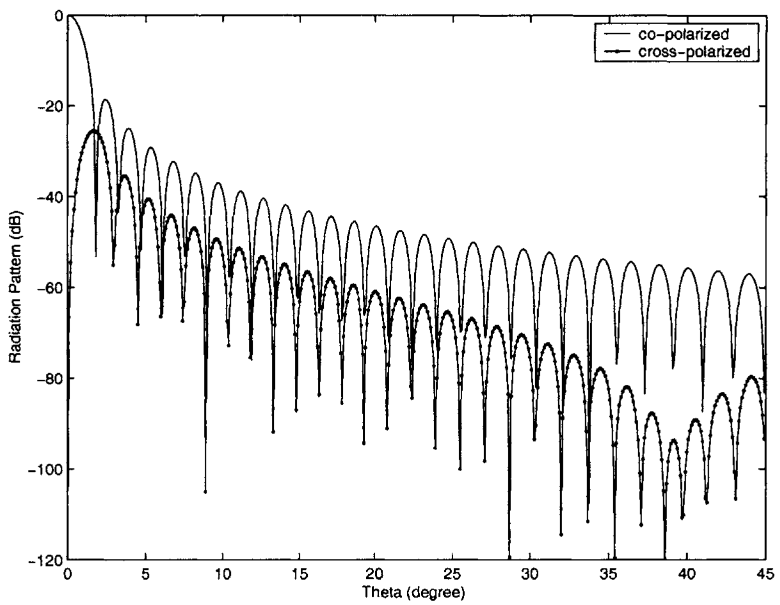

Figure 2-6: Co-polarized and cross-polarized radiation patterns on the plane tilted at 45 degrees from the principal E-plane and H-plane. The cross-polarized pattern is normalized with respect to the peak gain of the co-polarized pattern.

co-polarized patterns because they have a symmetry around the main axis on these planes. The cross-polarized patterns are not displayed because they do not appear on these planes due to the anti-symmetry of the cross-polarized component of $\overline{E}_{ap}$ around the $\phi' = 0$ and $\phi' = \pi/2$ lines. The E-plane and H-plane patterns look almost identical near the main lobe. The first null is located at $\theta = 1.8$ degrees. The peak side lobe level is -18.8 dB below the peak gain at $\theta = 2.4$ degrees.

Figure 2-6 shows the radiation pattern measured on the plane tilted at 45 degrees ($\phi = \pi/4$) between the principal E-plane and H-plane. Near the main axis where θ is small, F_x contributes most to E_{cr} (see Equation (2.62)), making the cross-polarized component on the aperture field the major cause of cross-polarized radiation on this plane. The co-polarized pattern on this plane looks similar to those on the principal planes; however, there is a significant increase in the level of cross-polarized radiation. In fact, this is the plane where the cross-polarization level reaches its maximum due to the symmetry of the cross-polarized component of $\overline{E}_{ap}$ around the $\phi' = \pi/4$ and $\phi' = 3\pi/4$ lines. The maximum level of the cross-polarized pattern is -25.5 dB below the peak gain at $\theta = 1.7$ degrees.

2.2 Numerical analysis of radiation pattern from a paraboloidal reflector by ray tracing

Ray tracing provides a numerical solution to electromagnetic problems by using the geometrical optics approach. In this section, we use ray tracing to find the aperture-field distribution of the ideal paraboloidal reflector with a linearly polarized isotropic feed. For each ray vector, four quantities will be determined and recorded: (1) the field intensity, which is related to the amplitude of the field, (2) the point of intersection with the aperture plane, (3) the polarization of the geometrical optics field represented by the ray, and (4) the path length that the ray travels from the feed to the aperture.

Numerical results from ray tracing will be compared with those obtained analytically from geometrical optics in the previous section in order to verify the accuracy of the implementation for the ideal paraboloidal reflector case. Later, this program will be used to find radiation patterns from reflector with random surface errors on the reflector surface.

2.2.1 The amplitude of the aperture field

Power distribution on the aperture of a paraboloidal reflector

In this section we use the concept of ray tube in geometrical optics to calculate the power distribution on the aperture of paraboloidal reflectors.

Equation (2.14) tells us that the radiated power flows along the paths of ray vectors. A ray tube is a feature of all the rays that pass through any given closed curve. The amount power flowing across any cross-section of a ray tube must be conserved since no power can flow across the lateral surfaces of the tube. Thus, as the cross-section of the ray tube increases, the power density per unit area decreases, and vice versa. These two cases correspond to converging and diverging rays respectively. For a ray tube passing through a differential area dA_1 on a wave front W_1 and intersects another wave front W_2 in the differential area dA_2, the total power flowing through dA_1 must be equal to the total power flowing through dA_2.

We can express this conservation of power in terms of the power density as follow

$$S_1 dA_1 = S_2 dA_2 \tag{2.63}$$

where S_1 is the power density (power per unit area) at dA_1 on W_1, and S_2 is the power density at dA_2 on W_2.

The concept of power flowing in ray tubes can be applied to the free-space region between the primary feed and the aperture of reflector antennas [38]. In the analysis of the power distribution on the aperture of the antenna or in the design of the feed for optimum illumination, the ray tube concept can be used to find an approximation to the relative power distribution. To determine the relative power distribution S_2/S_1, by Equation (2.63), it is necessary to know the ratio dA_1/dA_2 only to within a multiplicative constant. It turns out that this ratio can be easily determined from ray tracing.

Let S_0 be the power density at a wave front with radius R' centering at the source point O (see Figure 2-7). S_0 is related to the gain factor $G(\theta', \phi')$ of the source by

$$S_0 = \frac{1}{2\eta}|E(\theta', \phi')|^2 = \frac{P_t G(\theta', \phi')}{4\pi R'^2} \tag{2.64}$$

where P_t is the total radiated power from the source to the reflector. We will assume that $G(\theta', \phi')$ is symmetrical around the z'-axis and is a function of θ' only.

Let $S_1 = dP_1/dA_1$ and $S_2 = dP_2/dA_2$ be the power density at the reflector surface and at the aperture plane respectively. By the conservation law of geometrical optics, the amount of power flowing in the ray cone from the source to the reflector surface is equal to the amount

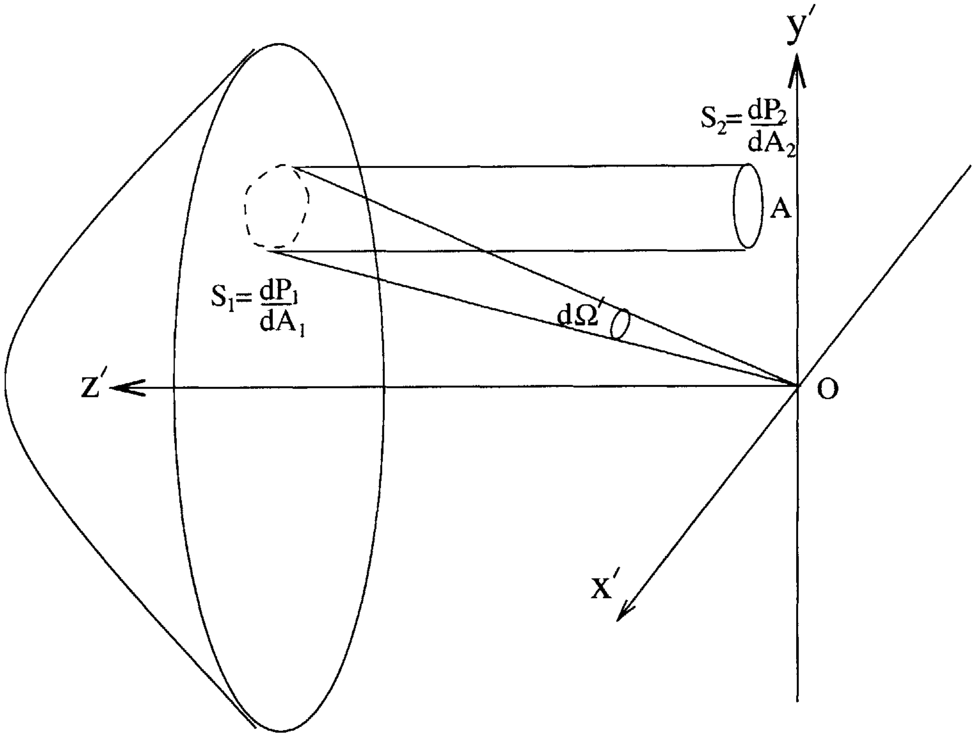

Figure 2-7: Geometrical optics analysis of power distribution on the aperture of a paraboloidal reflector.

of power flowing in the ray tube from the reflector surface to the aperture. This power is equal to

$$dP_1 = dP_2 = R'^2 S_0 d\Omega' = \frac{P_t}{4\pi} G(\theta') d\Omega' \tag{2.65}$$

From the definition, we find the power density on the aperture

$$S_2(\theta') = \frac{dP_2}{dA_2} = \frac{P_t}{4\pi} G(\theta') \frac{d\Omega'}{dA_2} \tag{2.66}$$

We substitute into Equation (2.66) $d\Omega' = \sin\theta' d\theta' d\phi'$ and $dA_2 = \rho' d\rho' d\phi'$ where $\rho' = r' \sin\theta'$. Since the paraboloidal reflector surface is described by $r' + r' \cos\theta' = 2f$ which gives $r' = f \sec^2(\theta'/2)$, we find $\rho' = 2f \tan(\theta'/2)$ and $d\rho' = f \sec^2(\theta'/2) d\theta' = r' d\theta'$. Finally, we obtain

$$\begin{aligned} S_2(\theta') &= \frac{P_t}{4\pi} G(\theta') \frac{\sin\theta' d\theta' d\phi'}{r'^2 \sin\theta' d\theta' d\phi'} \\ &= \frac{P_t}{4\pi} G(\theta') \cos^4 \frac{\theta'}{2} \end{aligned} \tag{2.67}$$

If the source point is isotropic, i.e., $G(\theta', \phi')$ is uniform, the field amplitude distribution on the aperture will be tapered around the edge of the dish by a factor of $\cos^2(\theta'/2)$. The distribution can be made uniform by making the gain of the source $G(\theta', \phi') = \sec^4(\theta'/2)$, which will bring the maximum aperture efficiency to the reflector.

Substitution of the aperture field with equivalent electric dipoles

In order to compute the far-field pattern from the aperture field distribution which is obtained by ray tracing, we divide the aperture area into a number of small patches. Each patch contains the point of intersection of a reflected ray and the aperture plane. The electromagnetic field on the patch will be replaced by an equivalent electric dipole located at the point of incidence. The magnitude and polarization of the dipole moment will be determined from the geometrical optics field which the ray vectors represent.

On the aperture plane, we find the magnitude of the electric and magnetic fields from Equation (2.14)

$$S_2(\theta') = \frac{1}{2\eta}|\overline{E}_2|^2 = \frac{\eta}{2}|\overline{H}_2|^2 \tag{2.68}$$

Using the equivalence principle [39], we may replace the electromagnetic field on the aperture by an equivalent current sheet $\overline{J}_s = 2(\hat{n} \times \overline{H}_2)$ whose magnitude is equal to

$$|\overline{J}_s(\theta')| = 2\sqrt{\frac{P_t G(\theta')}{2\pi\eta f^2}} \cos^2\frac{\theta'}{2} \tag{2.69}$$

We replace the surface current on a patch with area A_i by an electric dipole with dipole moment $\overline{I}_i l$. The magnitude of the dipole moment is equal to

$$\begin{aligned} |\overline{I}_i l| &= \iint_{A_i} |\overline{J}_s(\theta')|\, dA_2 \\ &= \iint_{\Omega'_i} 2\sqrt{\frac{P_t G(\theta')}{2\pi\eta f^2}} \cos^2\frac{\theta'}{2} f^2 \sec^4\frac{\theta'}{2} \sin\theta'\, d\theta' d\phi' \\ &= \iint_{\Omega'_i} 2\sqrt{\frac{P_t G(\theta')}{2\pi\eta f^2}} f^2 \cos^2\frac{\theta'}{2} \sec^4\frac{\theta'}{2}\, d\Omega' \\ &= C \iint_{\Omega'_i} \sec^2\frac{\theta'}{2}\, d\Omega' \end{aligned} \tag{2.70}$$

where $C = 2f\sqrt{\frac{P_t G}{2\pi\eta}}$ for an isotropic source and Ω'_i is the solid angle at the point source supported by area A_i (see Figure 2-7). We choose A_i such that they are supported by equal amount of solid angles $\Delta\Omega_i' = \Delta\Omega'$. We can write Equation (2.70) as

$$|\bar{I}_i l| = \Delta\Omega' C \sec^2 \frac{\overline{\theta}_i'}{2} \tag{2.71}$$

where $\overline{\theta}_i'$ is the 'mean value' of θ' that makes the left hand sides of Equations (2.70) and (2.71) equal for each A_i. The existence of $\overline{\theta}'$ is guaranteed by the Mean Value Theorem of calculus.

2.2.2 The ray vectors

Division of solid angles

We divide a spherical wave front surrounding the feed into patches with equal area. Each patch is the base of a ray cone whose vortex is located at the feed point. It is clear that each one of these cones will support the same amount of solid angle. The radiated power contained in a ray cone will be represented by a ray vector. The benefit of this scheme is that the power density associated with any ray will be a function of $G(\theta', \phi')$ only, which will make the implementation of ray tracing on a computer program easier. In case the source is an isotropic radiator, the average power flowing inside each of the cones will be the same, and each of the rays will represent electromagnetic field with equal amplitude.

When the ray vectors are generated for the purpose of studying the reflector by ray tracing, there are two points that we are concerned with. First, the number of rays must be large enough to cover adequately small areas on the reflector surface under the study. Second, the concentration of the rays should be distributed evenly over the spherical wave

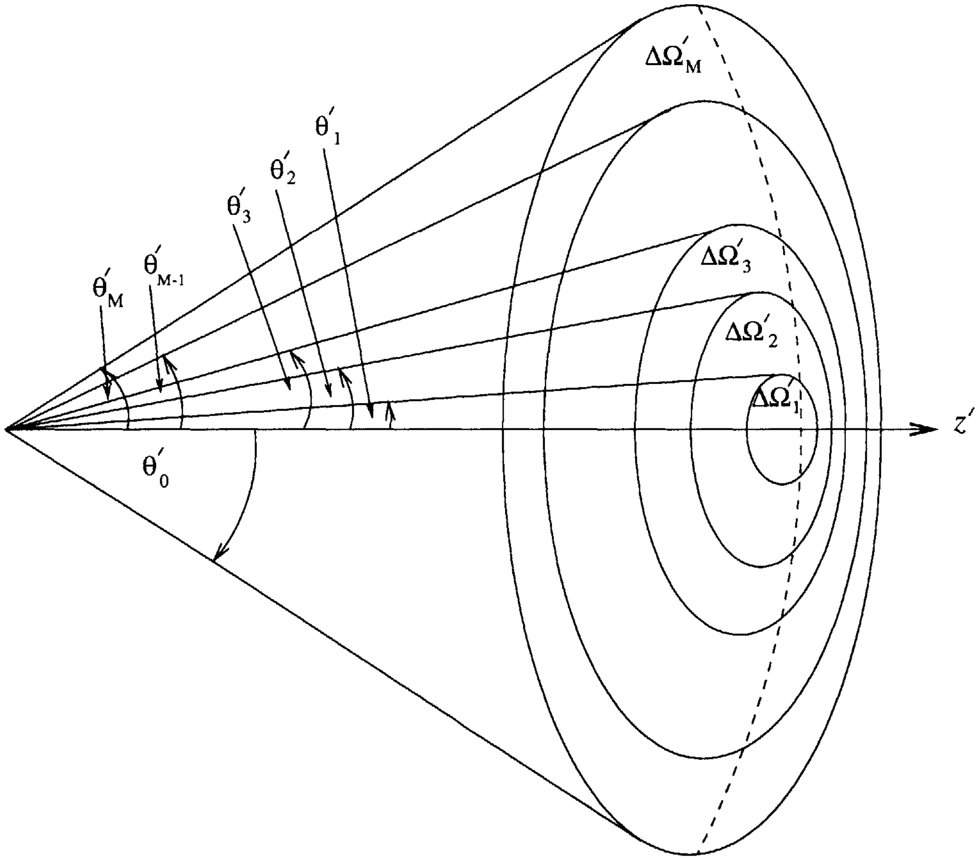

Figure 2-8: Division of a spherical wave front into M annular rings. The ith ring is supported by the solid angle $\Delta\Omega'_i$, where $\theta' = \theta'_0$ is the maximum angle supported by the poraboloid.

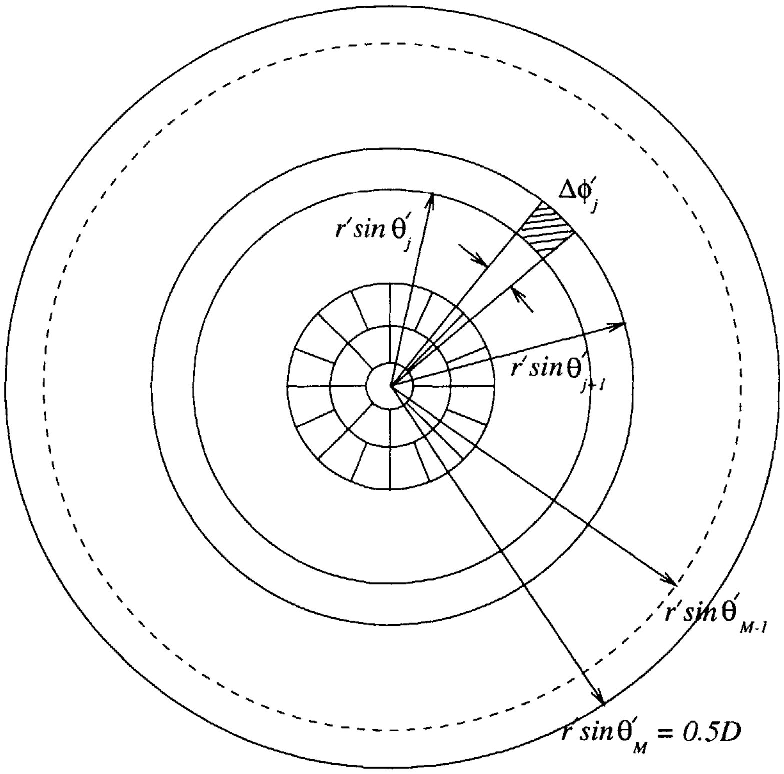

Figure 2-9: A view of solid angles on the aperture plane. The area on the jth ring is divided into N_j patches with equal area where $\Delta\phi'_j = 2\pi/N_j$.

front surrounding the point-source feed. This will result in the reflector surface being sampled non-selectively by the incident rays, making different areas on the reflector surface be equally represented by the outcome. A larger number of evenly distributed rays results in smaller spacing among the rays. This will bring a higher level of accuracy to the output of ray tracing, which can be thought of as a discrete geometrical optics.

In Figure 2-8, a spherical wave front supporting the solid angle Ω'_0 is divided into M rings. Each ring contains a group of N_i, $i = 1, 2, ..., M$, patches with equal surface area. The first ring is the spherical cap in the middle, which is bounded between the angles $\theta' = 0$ and $\theta' = \theta'_1$. The solid angles of the rings are calculated from the differential element $d\Omega' = \sin\theta' d\theta' d\phi'$ and are given by

$$\begin{aligned}
\Delta\Omega'_1 &= 2\pi(1 - \cos\theta'_1) \\
\Delta\Omega'_2 &= 2\pi(\cos\theta'_1 - \cos\theta'_2) \\
\vdots \quad & \quad \vdots \\
\Delta\Omega'_M &= 2\pi(\cos\theta'_{M-1} - \cos\theta'_M) \qquad (2.72)
\end{aligned}$$

Let $\Delta\Omega'_1$, the solid angle supported by the patch at the center, be the amount of solid angle supported by a ray cone. Then $\Delta\Omega'_i$ must be a N_i multiples of $\Delta\Omega'_1$, which we can express by the following equations

$$\begin{aligned}
N_1 &= 1 \\
N_2 &= \frac{\Delta\Omega'_2}{\Delta\Omega'_1}
\end{aligned}$$

$$
\begin{aligned}
&= \frac{1-\cos\theta'_2}{1-\cos\theta'_1} - 1 \\
N_3 &= \frac{\Delta\Omega'_3}{\Delta\Omega'_1} \\
&= \frac{\cos\theta'_2 - \cos\theta'_3}{1-\cos\theta'_1} \\
&= \frac{1-\cos\theta'_3}{1-\cos\theta'_1} - (1+N_2) \\
&\vdots \quad \vdots \\
N_M &= \frac{\Delta\Omega'_M}{\Delta\Omega'_1} \\
&= \frac{\cos\theta'_{M-1} - \cos\theta'_M}{1-\cos\theta'_1} \\
&= \frac{1-\cos\theta'_M}{1-\cos\theta'_1} - (1+N_2+\ldots+N_{M-1}) \qquad (2.73)
\end{aligned}
$$

Equation (2.73) has too many unknowns, and we cannot solve for θ'_i and N_i without imposing more constraints. As we mentioned earlier, we should have a uniform sampling on different parts of the the reflector surface in order to have more accurate results from ray tracing. For a given number of rays, they should be spread so that the ray vectors are distanced from each other as much as possible. To this end, the shape of the patches on each ring should become as close to a square as possible in order to maximize the mutual separation. Our solution is to have θ'_i, $1 \leq i \leq M$, be odd multiples of θ'_1, so that $\theta'_i = (2i-1)\theta'_1$ for $1 \leq i \leq M$ where $\theta'_0 = (2M-1)\theta'_1$. The number of patches N_i are obtained by substituting θ'_i into Equation (2.73) and rounding the answers to the nearest whole numbers.

Figure 2-10 plots the number of patches on each ring for a dish with size $D = 40\,\lambda$ and with the number of annular rings $M = 200$. The minimum distance between points of incidence on the reflector is approximately 0.1λ, which should be sufficient to give accurate results to ray tracing. In general, the diameter of the dish is equal to the product of twice

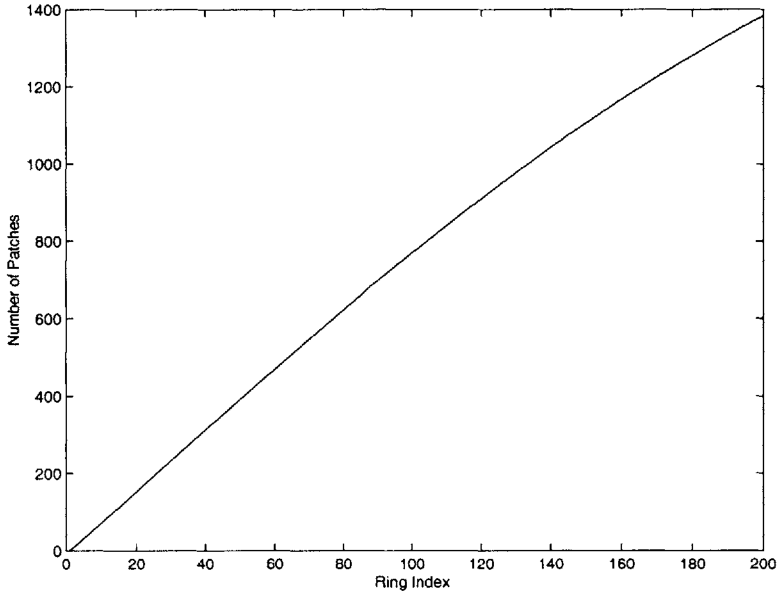

Figure 2-10: A plot showing the number of patches on each ring for a dish with $D = 40\ \lambda$ and $M = 200$ (total number = 149,131).

the sampling distance and M.

Directions of the incident ray vectors

Using the equivalence principle, we replace the aperture field by an equivalent electric current sheet. Later, we divide the aperture area into patches and replace the current sheet on each patch by an electric dipole. The locations of the dipoles are determined from the angles $\overline{\theta}'_i$ (see Equation (2.71)). We will approximate such angle for every patch from its centroid. Figure 2-11 shows the centroid of a spherical arc which is bounded by the angles θ'_1 and θ'_2. The centroid of the arc is located at position $\overline{r}'_c = \hat{x}'\, r'_{cx} + \hat{y}'\, r'_{cz}$ from the point source where

$$r'_{cx} = \frac{\int_{\theta'_1}^{\theta'_2} r'^2 \sin\theta' d\theta'}{\int_{\theta'_1}^{\theta'_2} r d\theta'}$$

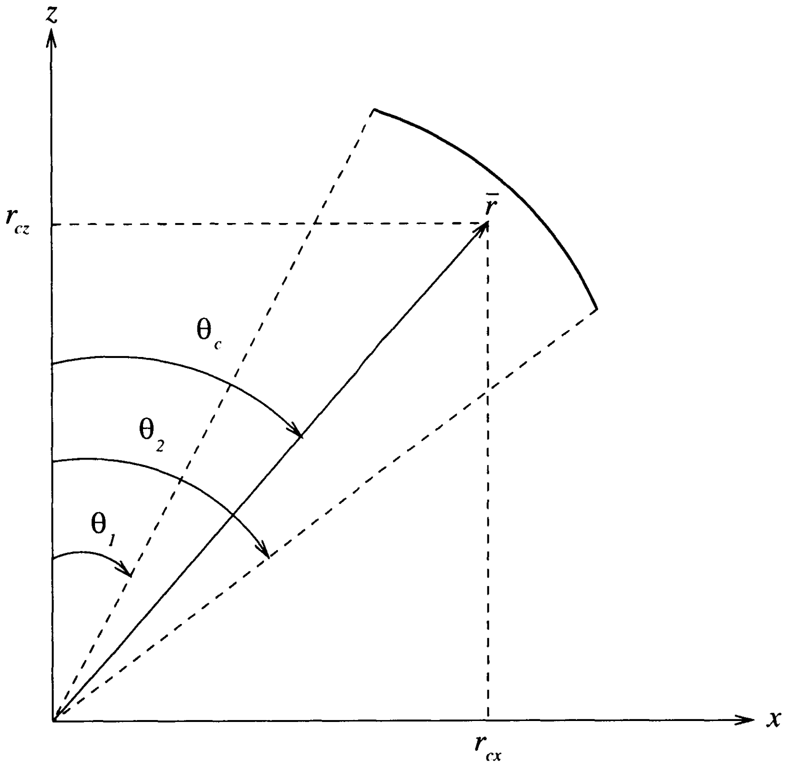

Figure 2-11: For a ray cone, the direction of the incident ray vector is taken to be the centroid of the spherical arc which is at the base of the ray cone.

$$= \frac{r'(\cos\theta'_1 - \cos\theta'_2)}{\theta'_2 - \theta'_1} \tag{2.74}$$

$$r'_{cz} = \frac{\int_{\theta'_1}^{\theta'_2} r'^2 \cos\theta' d\theta'}{\int_{\theta'_1}^{\theta'_2} r d\theta'}$$

$$= \frac{r'(\sin\theta'_2 - \sin\theta'_1)}{\theta'_2 - \theta'_1} \tag{2.75}$$

The angle θ'_c between $\overline{r}'_c$ and the z' axis is

$$\theta'_c = \tan^{-1}\left(\frac{r'_{cx}}{r'_{cz}}\right)$$

$$= \tan^{-1}\left(\frac{\cos\theta'_1 - \cos\theta'_2}{\sin\theta'_2 - \sin\theta'_1}\right) \tag{2.76}$$

2.2.3 Path lengths of the rays and polarization of the associated field

The path lengths which the rays travel from the source to the aperture plane determines the phase of the aperture field. From the assumption of geometrical optics, the electromagnetic energy travels along a ray is a local plane wave. Therefore, the phase of the field on a wave front is proportional to its distance from the source.

We begin with a description of the incident and reflected ray vectors for the case of the ideal paraboloid. Next, we determine points of incidence on the reflector surface from the incident rays, and use them to find points of intersection between the reflected rays and the aperture plane. The path lengths are determined from the distances between the source, points of incidence, and points of intersection. The polarization of the field associated with the ray vectors are determined from the polarization of the feed, the direction of the ray vectors, and the normal vector at the point of incidence.

The ray vectors

There are two types of ray vectors in our use of ray tracing to find the field distribution on the aperture of the reflector. The incident ray vectors $\hat{s}_i$ are simply unit vectors in the direction of incident rays onto the reflector surface and will be determined by the angles θ' and ϕ'. We can express $\hat{s}_i$ in terms of the feed coordinates as

$$\hat{s}_i = \hat{x}' \sin\theta' \cos\phi' + \hat{y}' \sin\theta' \sin\phi' + \hat{z}' \cos\theta' \tag{2.77}$$

The reflected ray vectors $\hat{s}_r$ are unit vectors in the directions of reflected rays from the reflector surface. They are determined from the incident ray vector $\hat{s}_i$ and the unit normal vector $\hat{n}$ to the reflector surface at the point of incidence

$$\hat{s}_r = \hat{s}_i - 2\hat{n}(\hat{n} \cdot \hat{s}_i) \tag{2.78}$$

For the ideal paraboloidal reflector, $\hat{n}$ is found to be

$$\hat{n} = -\hat{x}' \sin\frac{\theta'}{2} \cos\phi' - \hat{y}' \sin\frac{\theta'}{2} \sin\phi' - \hat{z}' \cos\frac{\theta'}{2} \tag{2.79}$$

and $\hat{s}_r$ is equal to

$$\hat{s}_r = -\hat{z}' \tag{2.80}$$

Points of incidence on the reflector surface

The points of incidence of the incident ray vectors on the reflector surface are determined from equations describing both entities either in the rectangular or the spherical coordinate systems. In the rectangular coordinate system, the paraboloid is described by

$$x'^2 + y'^2 = 4f(f - z') \qquad x'^2 + y'^2 \le \frac{D^2}{4} \tag{2.81}$$

where f is the focal length, and D is the diameter of the dish. In the spherical coordinate system, the paraboloidal surface is given by

$$r' = \frac{2f}{1 + \cos\theta'} = f \sec^2 \frac{\theta'}{2} \qquad \theta' \le \theta'_0 \tag{2.82}$$

In both expression, the focal point of the paraboloid lies at the origins of the coordinate systems. In the spherical coordinate system, a point of incidence $(r'_0, \theta'_0, \phi'_0)$ and its distance d from the origin are easily found from Equation (2.82) for a given $\hat{s}_i$. In the rectangular coordinate system, the point of incidence (x'_0, y'_0, z'_0) and its distance d from the origin can be found for a given incident vector $\hat{s}_i$ by solving Equation (2.81) with the parametric equations

$$x'_0 = d \sin\theta' \cos\phi' \tag{2.83}$$

$$y'_0 = d \sin\theta' \sin\phi' \tag{2.84}$$

$$z'_0 = d \cos\theta' \tag{2.85}$$

in which the solutions are

$$
\begin{aligned}
d &= \frac{2f(1-\cos\theta')}{\sin^2\theta'} && (2.86)\\
x_0' &= \frac{2f(1-\cos\theta')\cos\phi'}{\sin\theta'} && (2.87)\\
y_0' &= \frac{2f(1-\cos\theta')\sin\phi'}{\sin\theta'} && (2.88)\\
z_0' &= \frac{2f(1-\cos\theta')\cos\theta'}{\sin^2\theta'} && (2.89)
\end{aligned}
$$

Points of intersection between the reflected rays and the aperture plane

The locations of the electric dipoles on the aperture plane are determined from the equations of the reflected rays and the aperture plane. The parametric equations of the line passing through the point $\overline{P}_0 = (x_0', y_0', z_0')$ along the direction of $\hat{s}_r$ are

$$
\begin{aligned}
x' &= x_0' + d \cdot s_{rx} && (2.90)\\
y' &= y_0' + d \cdot s_{ry} && (2.91)\\
z' &= z_0' + d \cdot s_{rz} && (2.92)
\end{aligned}
$$

where d is the distance from (x', y', z') to (x_0', y_0', z_0'), and s_{rx},s_{ry},s_{rz} are the x',y',z' components of $\hat{s}_r$ respectively. If we choose the focal plane (the xy-plane) to be the aperture plane, d will be given by

$$d = -\frac{z_0'}{s_{rz}} \qquad (2.93)$$

The coordinates (x_{ap}, y_{ap}) of the point of intersection between the reflected ray and the aperture plane are

$$x_{ap} = x_0' - z_0' \frac{s_{rx}}{s_{rz}} \tag{2.94}$$

$$y_{ap} = y_0' - z_0' \frac{s_{ry}}{s_{rz}} \tag{2.95}$$

Polarization of the field associated with the ray vector

Assuming that the source is $\hat{y}'$-polarized, the polarization of the electric field associated with an incident ray vector is determined from the polarization of the feed and the direction of the incident ray by

$$\hat{e}_i = \frac{\hat{s}_i \times (\hat{y}' \times \hat{s}_i)}{|\hat{s}_i \times (\hat{y}' \times \hat{s}_i|)} = \frac{\hat{y}' - (\hat{s}_i \cdot \hat{y}')\hat{s}_i}{|\hat{y}' - (\hat{s}_i \cdot \hat{y}')\hat{s}_i|} \tag{2.96}$$

The polarization of the reflected ray is determined from the polarization of the incident ray and the unit vector at the point of incidence by

$$\hat{e}_r = 2\hat{n}(\hat{n} \cdot \hat{e}_i) - \hat{e}_i \tag{2.97}$$

2.2.4 Radiation field from the aperture dipoles

Figure 2-12 shows the distribution and polarization of equivalent electric dipoles on the aperture plane as a result of ray tracing. Differences in polarization and magnitudes of the dipole moments are captured by the orientation and sizes of the vectors. The symmetry and anti-symmetry of the components of the dipoles reflect those of the co-polarized and cross-polarized components of the aperture field.

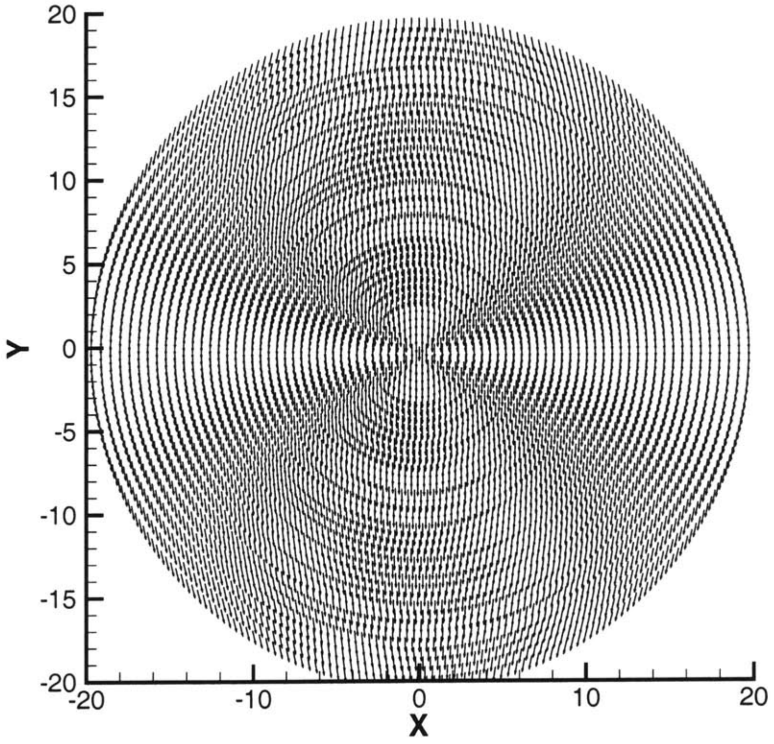

Figure 2-12: Distribution and polarization of equivalent electric dipoles on the aperture plane of a paraboloidal reflector with a linear isotropic feed obtained by ray tracing.

The current density for the electric dipoles located on the aperture are

$$\begin{aligned}\overline{J}_i(\overline{r}') &= \overline{I}_i l e^{ikd_i}\delta(\overline{r}' - \overline{r}_i') \\ &= \hat{x}\, I_{ix} l e^{ikd_i}\delta(\overline{r}' - \overline{r}_i') + \hat{y}\, I_{iy} l e^{ikd_i}\delta(\overline{r}' - \overline{r}_i') \qquad (2.98)\end{aligned}$$

where $\overline{I}_i l$ designate the current dipole moments, $I_{ix}l$ and $I_{iy}l$ are the x and y components of $\overline{I}_i l$ respectively, $\overline{r}_i'$ are the positions of the dipoles on the aperture plane, and d_i are the path lengths of the geometrical optics rays. In case of the ideal paraboloid, d_i are equal to $r' + r'\cos\theta' = 2f$ and will have no effect on the radiation patterns. In general, random deviations on the reflector surface will make the path lengths differ from each other. If the point source at the focus is linearly polarized in the $\hat{y}$ direction, $\overline{I}_{iy}l$ will correspond to the co-polarized components of the aperture field and $\overline{I}_{ix}l$ will correspond to the cross-polarized components. The vector current moments $\overline{f}_i(\theta, \phi)$ for the dipoles are [7]

$$\begin{aligned}\overline{f}_i(\theta,\phi) &= \iiint dV'\, \overline{J}_i(\overline{r}') e^{-i\overline{k}\cdot\overline{r}'} \\ &= \iiint dV'\, \overline{I}_i l e^{ikd_i}\delta(\overline{r}' - \overline{r}_i') e^{-i\overline{k}\cdot\overline{r}'} \\ &= (\hat{x}\, I_{ix}l + \hat{y}\, I_{iy}l) e^{ikd_i} e^{-i\overline{k}\cdot\overline{r}_i'} \qquad (2.99)\end{aligned}$$

Using the following transformation of vectors from the rectangular coordinates to the spherical coordinates

$$\hat{x} = \hat{r}\, \sin\theta\, \cos\phi + \hat{\theta}\, \cos\theta\, \cos\phi - \hat{\phi}\, \sin\phi \qquad (2.100)$$

$$\hat{y} = \hat{r}\, \sin\theta\, \sin\phi + \hat{\theta}\, \cos\theta\, \sin\phi + \hat{\phi}\, \cos\phi \qquad (2.101)$$

we can express the vector current moments in Equation (2.99) in spherical coordinates as

$$\begin{aligned}\overline{f}_i(\theta,\phi) &= e^{ikd_i}e^{-i\overline{k}\cdot\overline{r}'_i}\{\hat{r}(I_{ix}l\sin\theta\cos\phi + I_{iy}l\sin\theta\sin\phi) \\ &\qquad +\hat{\theta}(I_{ix}l\cos\theta\cos\phi + I_{iy}l\cos\theta\sin\phi) + \hat{\phi}(-I_{ix}l\sin\phi + I_{iy}l\cos\phi)\} \quad (2.102)\end{aligned}$$

In the far-field region, the electric field is expressed in terms of the $\hat{\theta}$ and $\hat{\phi}$ components of the vector current moment by (see Appendix A)

$$\overline{E}(\overline{r}) = i\omega\mu\frac{e^{ikr}}{4\pi r}(\hat{\theta}f_\theta + \hat{\phi}f_\phi) \quad (2.103)$$

The total field is a superposition of the fields from the individual dipoles and is expressed by

$$\begin{aligned}\overline{E}(\overline{r}) &= \sum_{i=1}^{N} i\omega\mu\frac{e^{ikr}}{4\pi r}(\hat{\theta}f_{i\theta} + \hat{\phi}f_{i\phi}) \\ &= \sum_{i=1}^{N} i\omega\mu\frac{e^{ikr}}{4\pi r}e^{ikd_i}e^{-i\overline{k}\cdot\overline{r}'_i}\{\hat{\theta}(I_{ix}l\cos\theta\cos\phi + I_{iy}l\cos\theta\sin\phi) \\ &\qquad +\hat{\phi}(-I_{ix}l\sin\phi + I_{iy}l\cos\phi)\} \quad (2.104)\end{aligned}$$

From our definition of polarization, the co-polarized and cross-polarized components of the radiation field are

$$\begin{aligned}E_{co} &= \overline{E}(\overline{r})\cdot\hat{i}_{co} \\ &= i\omega\mu\frac{e^{ikr}}{4\pi r}\sum_{i=1}^{N}\frac{1}{\sqrt{1-\sin^2\theta\sin^2\phi}}(f_{i\theta}\cos\theta\sin\phi + f_{i\phi}\cos\phi)\end{aligned}$$

$$
\begin{aligned}
&= i\omega\mu\frac{e^{ikr}}{4\pi r}\sum_{i=1}^{N}\frac{1}{\sqrt{1-\sin^2\theta\sin^2\phi}}e^{ikd_i}e^{-i\overline{k}\cdot\overline{r}'_i}\{(I_{ix}l\cos\theta\cos\phi+I_{iy}l\cos\theta\sin\phi)\cos\theta\sin\phi \\
&\quad +(-I_{ix}l\sin\phi+I_{iy}l\cos\phi)\cos\phi\} \\
&= i\omega\mu\frac{e^{ikr}}{4\pi r}\sum_{i=1}^{N}\frac{1}{\sqrt{1-\sin^2\theta\sin^2\phi}}e^{ikd_i}e^{-i\overline{k}\cdot\overline{r}'_i}\{-I_{ix}l\sin^2\theta\sin\phi\cos\phi \\
&\quad +I_{iy}l(1-\sin^2\theta\sin^2\phi)\} \qquad (2.105)
\end{aligned}
$$

$$
\begin{aligned}
E_{cr} &= \overline{E}(\overline{r})\cdot\hat{i}_{cr} \\
&= i\omega\mu\frac{e^{ikr}}{4\pi r}\sum_{i=1}^{N}\frac{1}{\sqrt{1-\sin^2\theta\sin^2\phi}}(f_{i\theta}\cos\phi+f_{i\phi}\cos\theta\sin\phi) \\
&= i\omega\mu\frac{e^{ikr}}{4\pi r}\sum_{i=1}^{N}\frac{1}{\sqrt{1-\sin^2\theta\sin^2\phi}}e^{ikd_i}e^{-i\overline{k}\cdot\overline{r}'_i}\{(I_{ix}l\cos\theta\cos\phi+I_{iy}l\cos\theta\sin\phi)\cos\phi \\
&\quad +(-I_{ix}l\sin\phi+I_{iy}l\cos\phi)\cos\theta\sin\phi\} \\
&= i\omega\mu\frac{e^{ikr}}{4\pi r}\sum_{i=1}^{N}\frac{1}{\sqrt{1-\sin^2\theta\sin^2\phi}}e^{ikd_i}e^{-i\overline{k}\cdot\overline{r}'_i}I_{ix}l\cos\theta \qquad (2.106)
\end{aligned}
$$

Figures 2-13 and Figure 2-14 show the radiation patterns of a paraboloidal reflector with parameters $D = 40\,\lambda$ and $f/D = 0.5$, which are obtained from ray tracing. The feed is assumed isotropic ($G(\theta', \phi') = 1$) and vertically polarized. Figure 2-13 shows the radiation patterns on the principal E-plane ($\phi = \pi/2$) and and H-plane ($\phi = 0$). Only the co-polarized patterns are displayed because the cross-polarized patterns do not appear on these planes. This can be explained from Equation (2.106) when we take into account the symmetry of the reflector and the anti-symmetry of $I_{ix}l$ around the x-axis and y-axis. The E- and H-plane patterns look almost identical at the main lobe, which suggests a near circular shape for the main beam. The first null is located at $\theta = 1.9$ degrees. The peak side-lobe level is -20.0 dB at $\theta = 2.4$ degrees. Near $\theta = 45$ degrees the level of the last side lobe is -58.8 dB on the E-plane and -55.8 dB on the H-plane.

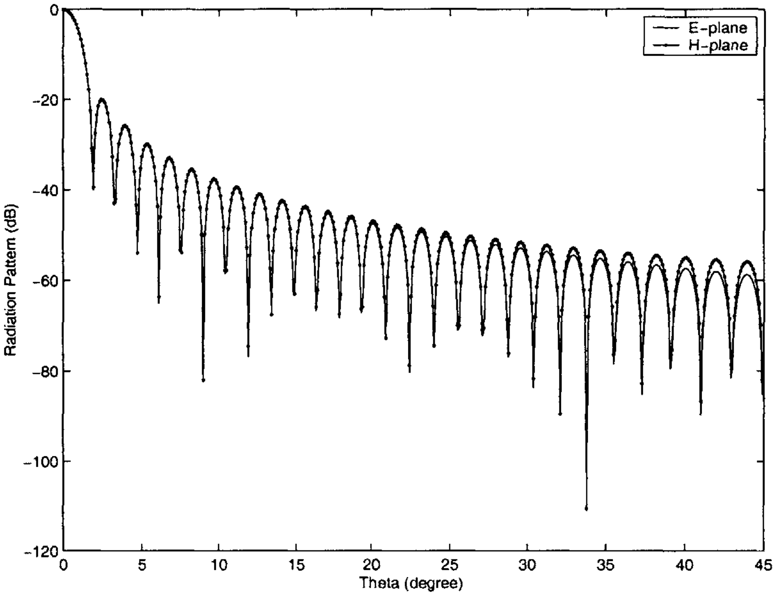

Figure 2-13: Co-polarized radiation patterns on the principal E-plane and H-plane for a paraboloidal reflector ($D = 40\,\lambda, f/D = 0.5$) with a linearly polarized isotropic feed obtained by ray tracing.

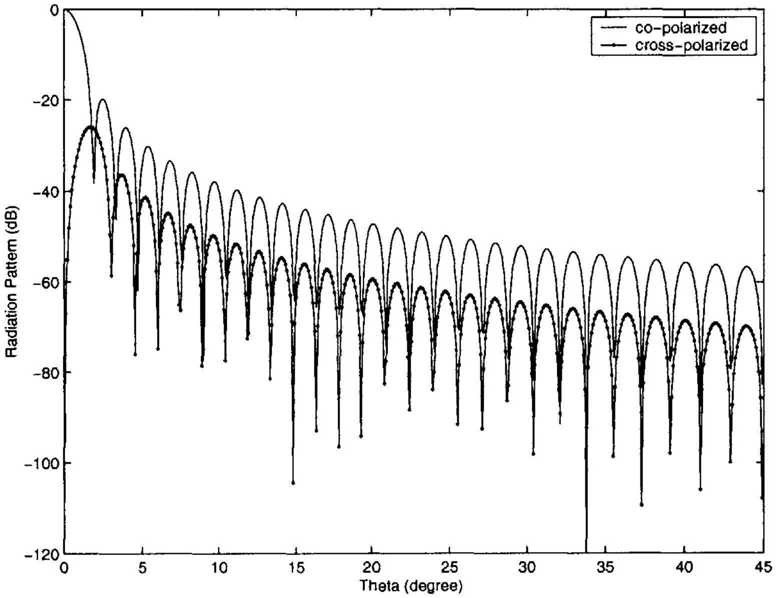

Figure 2-14: Co-polarized and cross-polarized radiation patterns on the plane tilted at 45 degrees from the principal E-plane and H-plane obtained by ray tracing.

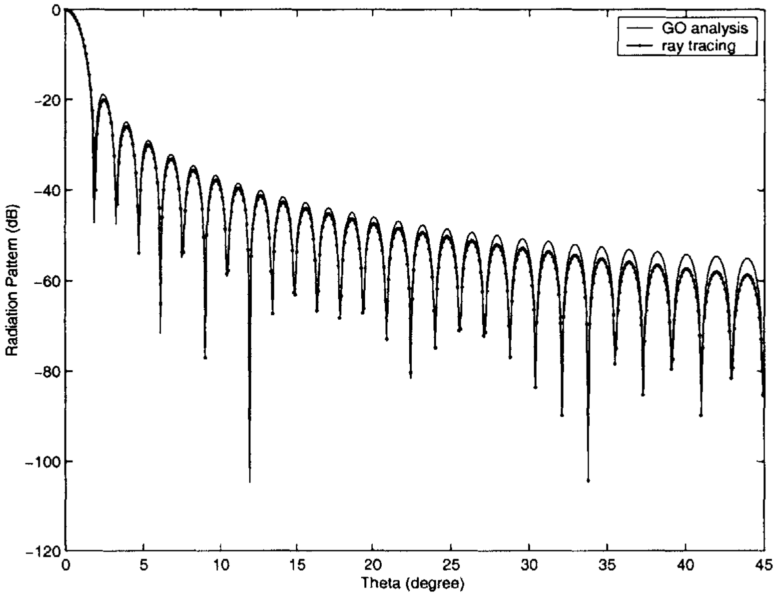

Figure 2-15: Comparison of the co-polarized radiation patterns on the E-plane between GO analysis and ray tracing.

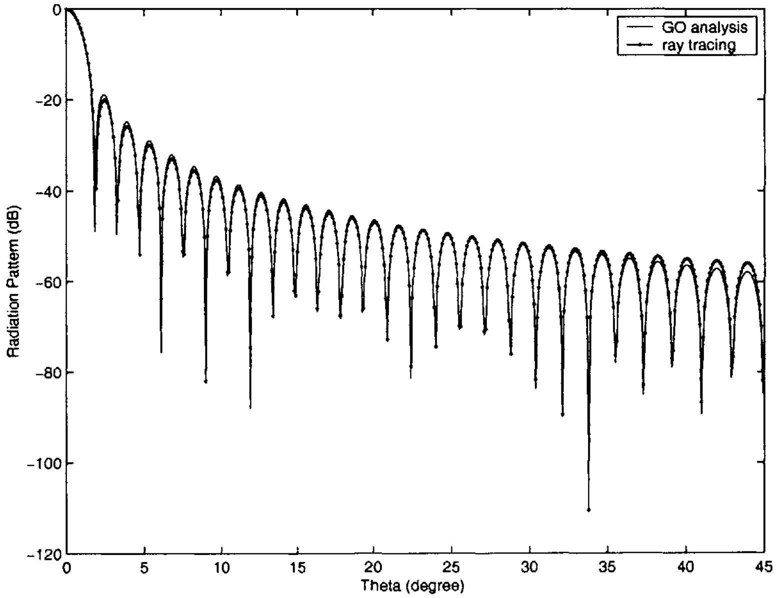

Figure 2-16: Comparison of the co-polarized radiation patterns on the H-plane between GO analysis and ray tracing.

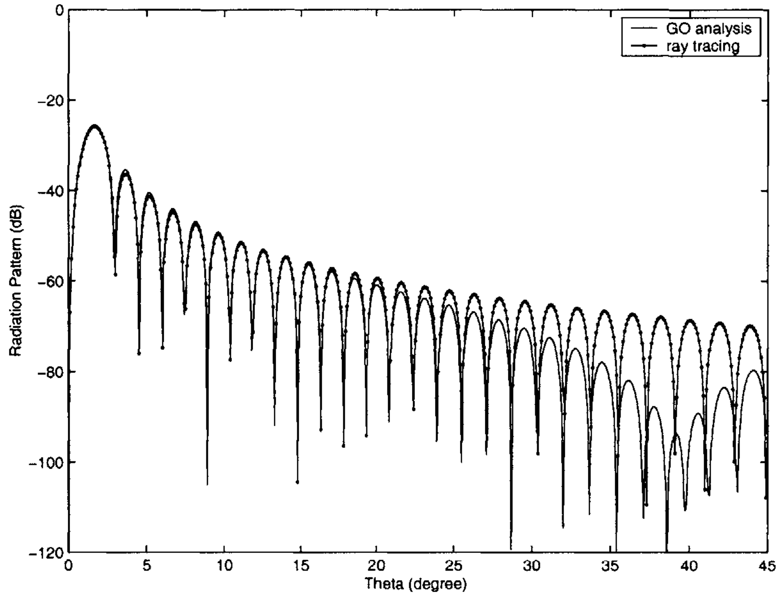

Figure 2-17: Comparison of the cross-polarized radiation patterns on the 45-degree plane between GO analysis and ray tracing.

Figure 2-14 shows the radiation patterns measured on the plane tilted at 45 degrees ($\phi = \pi/4$) between the principal E-plane and H-plane. The co-polarized pattern on this plane looks similar to those on the E-plane and H-plane. However, there is a significant increase in the cross-polarization level, which reaches its maximum on this plane. The maximum level of the cross-polarized pattern is -25.9 dB below the peak gain at $\theta = 1.7$ degrees.

Figures 2-15 to 2-17 show a comparison between (1) results obtained from GO analysis of aperture field and application of Huygens principle and (2) results obtained from ray tracing and evaluation of the far field based on a superposition of electric dipoles. Both methods yield almost identical results near the main lobe. The radiation patterns obtained from both methods agree well in the region near the main lobe, especially in the positions of the null points, which are almost identical. This is a good confirmation that the formulation and the implementation of the ray tracing program are correct.

2.3 Physical Optics

The radiation field can be found precisely if the exact current distribution on the reflector is known. However, in practice, it is unlikely that we know the exact current distribution on most radiators except for a few cases where the geometry is simple. Physical optics (PO) is often used to approximate the induced current distribution on the reflector surface. PO is a high-frequency method that can be used to find scattered field from a reflecting surface accurately when the PO approximation current is reasonably close to the true current distribution. The physical optics approximations of the induced surface currents are valid when the transverse dimensions of the reflector, the radii of curvature of the reflector, and the radius of curvature of the incident wave front are much larger than the wavelengths. PO is considered more general than geometrical optics (GO) since the equations obtained from PO for the scattered field from a conducting body can be reduced to the equations of GO in the high-frequency limit [6].

2.3.1 Physical optics analysis of radiation pattern from a paraboloidal reflector

In this section, PO will be applied to find the radiation field of a paraboloidal reflector with a point-source feed at the focus. The incident wave on the reflector surface can be expressed by

$$\overline{E}_i = \hat{e}_i E(\theta', \phi') \frac{e^{i\omega r'/c}}{r'} \tag{2.107}$$

where r' is the distance from the point source to the reflector surface. The magnitude of $E(\theta', \phi')$ is related to the gain factor of the feed according to Equation (2.21), and $\hat{e}_i$ is given by Equation (2.23). The currents which excite the scattered field are induced on the conducting surface by the incident wave. According to physical optics, the induced current density on the reflector surface can be approximated by

$$\overline{J}_s = \hat{n} \times (\overline{H}_i + \overline{H}_r) \tag{2.108}$$

where $\hat{n}$ is the unit normal to the paraboloid, $\overline{H}_i$ is the incident magnetic field, and $\overline{H}_r$ is the reflected magnetic field. The inexplicit assumption for the PO approximation is that the incident wave upon the reflector surface reflects locally as a plane wave. This approximation is true only on the illuminated side of the reflector since we assume no current density on the shadow side. On a perfectly conducting surface, $\hat{n} \times \overline{H}_i = \hat{n} \times \overline{H}_r$, making

$$\overline{J}_s = 2(\hat{n} \times \overline{H}_i) = 2(\hat{n} \times \overline{H}_r) \tag{2.109}$$

In terms of the incident and reflected electric fields, $\overline{H}_i = \frac{1}{\eta}\hat{s}_i \times \overline{E}_i$ and $\overline{H}_r = \frac{1}{\eta}\hat{s}_r \times \overline{E}_r$, the surface current density becomes

$$\overline{J}_s = \frac{2}{\eta}[\hat{n} \times (\hat{s}_i \times \overline{E}_i)] = \frac{2}{\eta}[\hat{n} \times (\hat{s}_r \times \overline{E}_r)] \tag{2.110}$$

For the ideal paraboloidal reflector, $\hat{s}_r = -\hat{z}'$ and $-\hat{z}' \cdot \hat{n} = \cos\theta'/2$. We find

$$\overline{J}_s(\overline{r}') = [\hat{e}_r \cos\frac{\theta'}{2} - \hat{z}'(\hat{n} \cdot \hat{e}_r)] \frac{2E(\theta', \phi')}{\eta} \frac{e^{ikr'}}{r'} \tag{2.111}$$

where $\hat{e}_r$ is given by

$$\hat{e}_r = \frac{1}{\sqrt{1 - \sin^2\theta' \sin^2\phi'}} \{\hat{x}'(1 - \cos\theta') \sin\phi' \cos\phi' - \hat{y}'(\cos\theta' \sin^2\phi' + \cos^2\phi')\} \tag{2.112}$$

Once the current distribution on the reflector surface is known, we may find the radiation field from

$$\overline{E}(\overline{r}) = i\omega\mu \frac{e^{ikr}}{4\pi r}(\hat{\theta} f_\theta + \hat{\phi} f_\phi) = i\omega\mu \frac{e^{ikr}}{4\pi r}(\hat{i}_{co} f_{co} + \hat{i}_{cr} f_{cr}) \tag{2.113}$$

where the vector current moment is given by

$$\overline{f} = \iint dS' \overline{J}_s(\overline{r}') e^{i\overline{k} \cdot \overline{r}'} \tag{2.114}$$

The vector current moment in Equation (2.113) can be expressed in terms of the co-polarized and the cross-polarized components because the polarization vectors are always perpendicular to $\hat{r}$. In Equation (2.114), the differential area dS' on the paraboloidal surface is

$$dS' = (r' \sin\theta' d\phi')(r' \sec\frac{\theta'}{2}\, d\theta') = f^2 \sec^5\frac{\theta'}{2}\, d\Omega' \tag{2.115}$$

and the phase retardation factor inside the integral is, according to the geometry in Figure 2-

3,

$$\bar{k} \cdot \bar{r}' = -kr'(\sin\theta \sin\theta' \cos(\phi' + \phi) + \cos\theta \cos\theta') \tag{2.116}$$

In the radiation zone, the time-average Poynting's vector is given by

$$< S_r >= \hat{r}\frac{1}{2\eta}|\overline{E}(\bar{r})|^2 = \hat{r}\frac{\eta}{2}(\frac{k}{4\pi r})^2(|f_\theta|^2 + |f_\phi|^2) = \hat{r}\frac{\eta}{2}(\frac{k}{4\pi r})^2(|f_{co}|^2 + |f_{cr}|^2) \tag{2.117}$$

The antenna gain is, in terms of the polarized components of $\overline{f}(\theta, \phi)$,

$$G(\theta, \phi) = \frac{< S_r >}{P_r/(4\pi r^2)} = \frac{\eta k^2}{8\pi P_r}(|f_\theta|^2 + |f_\phi|^2) = \frac{\eta k^2}{8\pi P_r}(|f_{co}|^2 + |f_{cr}|^2) \tag{2.118}$$

2.3.2 Numerical results

In the numerical analysis of PO, we begin with the identification of the incident ray vectors $\hat{s}_i$; each one is given in terms of the angles θ' and ϕ' of the feed coordinate system. The surface current density will be computed according to Equation (2.110) for each ray vector. The vector current moment is computed for each $\hat{s}_i$ from Equations (2.114), (2.115), and (2.116). The radiation field can be computed from Equation (2.113), but we will be more interested in the radiation pattern, which is independent of the distance from the reflector. According to Equation (2.118), the gain can be computed from the components of the vector current moment. The radiation pattern will be obtained by normalizing the gain by its maximum value, which will appear on the main axis.

Figure 2-18 and Figure 2-19 compare the co-polarized radiation pattern in the E-plane and H-plane between the numerical results obtained from PO and GO. In the case of the

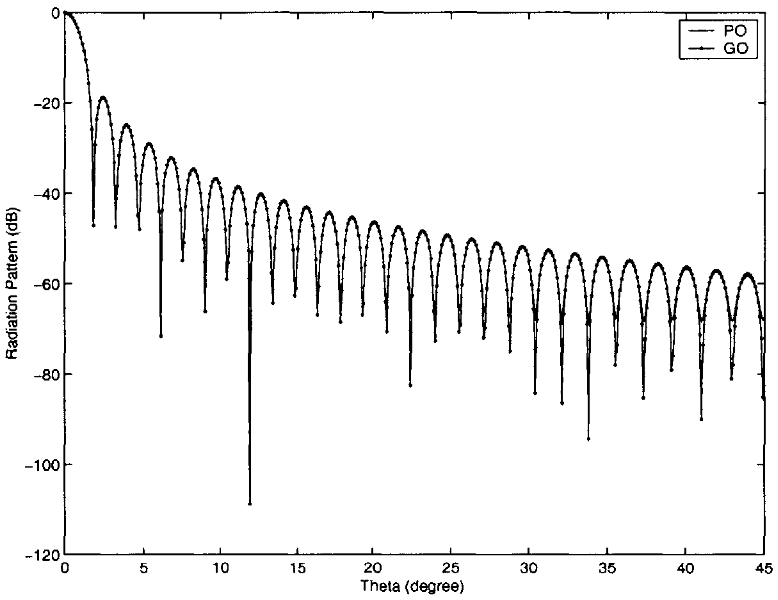

Figure 2-18: Comparison of the co-polarized radiation patterns on the E-plane between PO and GO ray tracing.

paraboloidal reflector, the excellent agreement between PO and GO is confirmed by the theoretical work [32]. Figure 2-20 shows a comparison of the cross-polarized pattern on the 45-degree plane between PO and GO. The obvious discrepancy between the two patterns is due to the z'-component of the PO current elements.

2.3.3 Region of good agreement between GO and PO

On the main axis, the far field obtained from the geometrical optics/aperture integration (GO/AI) method and the physical optics/surface integration (PO/SI) method are identical [6][40]. However, there is a limit to this agreement as the point of observation moves away from the main axis. We want to find the maximum value of the angle of observation where results from PO and GO remains in agreement.

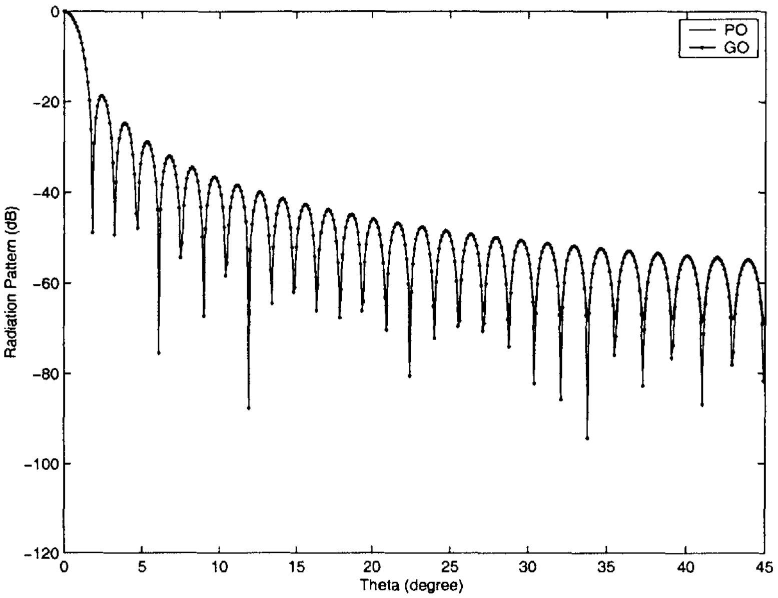

Figure 2-19: Comparison of the co-polarized radiation patterns on the H-plane between PO and GO ray tracing.

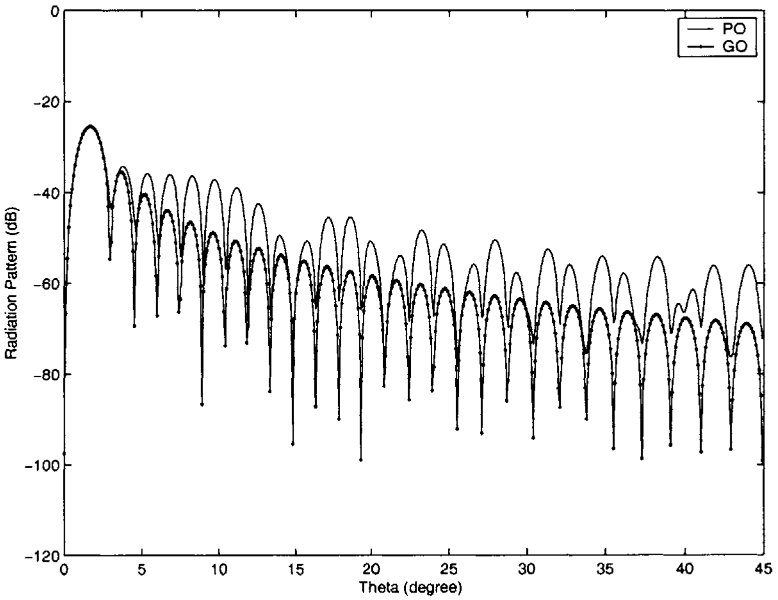

Figure 2-20: Comparison of the cross-polarized radiation patterns on the 45-degree plane between PO and GO ray tracing.

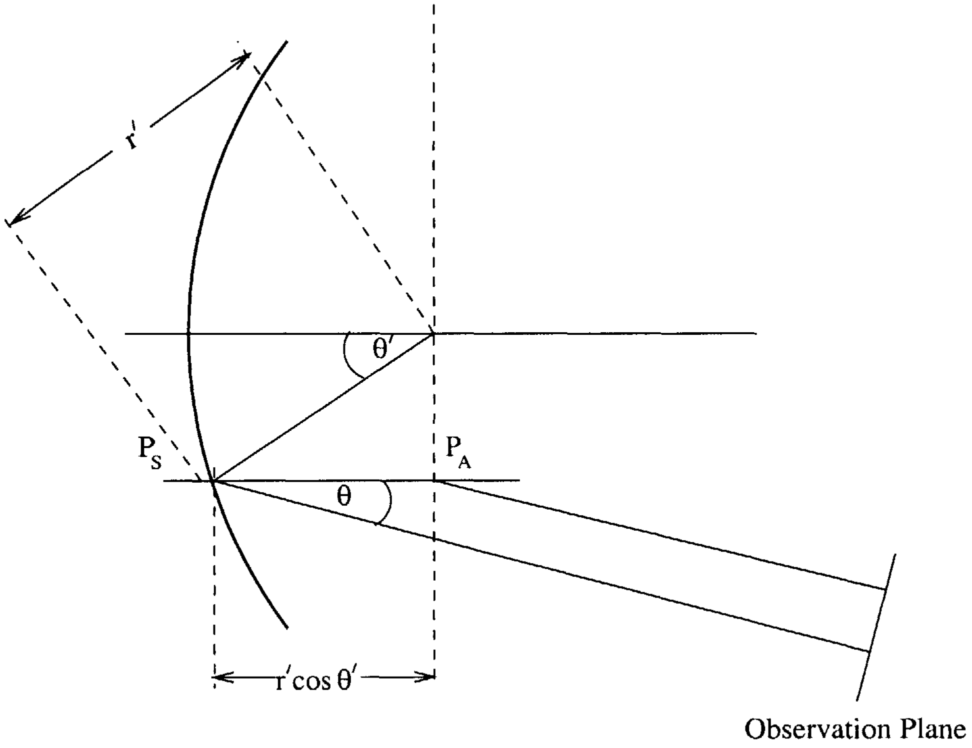

Figure 2-21: Path-length difference between the current elements of PO and GO to the plane of observation.

Let P_S be a point on the reflector surface and P_A be a point on the aperture plane related to P_S as shown in Figure 2-21. The current element at P_A has additional phase compared to the current element at P_S by the amount of $\frac{2\pi}{\lambda} r' \cos\theta'$. The total path-length difference from the observation plane to the current elements at P_S and P_A is given by

$$\Delta R = r' \cos\theta'(1 - \cos\theta) = f \sec^2 \frac{\theta'}{2} \cos\theta'(1 - \cos\theta) \tag{2.119}$$

The maximum value of ΔR occurs when the integration points P_S and P_A are on the main axis

$$\Delta R_{max} = f(1 - \cos\theta) \tag{2.120}$$

The minimum value of ΔR occurs when the P_S is on the reflector rim, and P_A is on the circumference of the aperture

$$\Delta R_{min} = f \left(1 - \left(\frac{D}{4f}\right)^2\right) (1 - \cos\theta) \tag{2.121}$$

Thus, the maximum value of variation in the path-length difference is equal to

$$\Delta R_{max} - \Delta R_{min} = \frac{D^2}{16f}(1 - \cos\theta) = \frac{D^2}{8f} \sin^2 \frac{\theta}{2} \tag{2.122}$$

In the far field, the reason for the discrepancy between PO and GO patterns is the variation in the path-length difference. This variation is caused by the curvature of the reflector surface.

By convention, the far field begins at the distance where the path-length variation due to the far-field approximation is less than $\lambda/16$ for any points on the radiator [7][6]. By the same criterion, the maximum value of θ where GO still agrees with PO is given by

$$\sin\frac{\theta_M}{2} = \sqrt{\frac{1}{2}\left(\frac{\lambda}{D}\right)\left(\frac{f}{D}\right)} \tag{2.123}$$

In our case, we substitute $D/\lambda = 40$ and $f/D = 0.5$ and obtain

$$\theta_M = 2\sin^{-1}\sqrt{\frac{1}{160}} \approx 9.0^\circ \tag{2.124}$$

Thus, the curvature of the paraboloidal reflector surface will limit the region of good agreement between GO and PO to less than the observation angle $\theta = 9.0^\circ$. However, the axial components of PO current elements may reduce this range further.

2.4 Conclusion

We have formulated a computational method based on geometrical optics to analyze the radiation field from paraboloidal reflector antennas with a linearly polarized point feed. Our scheme is based on finding the current elements (electric dipoles) on the aperture plane which will determine the pattern of radiation in the far field. The magnitude, location, phase, and polarization of each dipole contain information about the point of incidence, so the whole collection of dipoles would reflect the condition on the reflector surface. The model is intended to be used to study radiation fields from paraboloidal reflectors with small random surface errors. One of the nice features of our approach is that we are not required to know the field values at any predetermined locations on the aperture plane, which is demanded if the original diffraction integral is used to find the radiation field. We think this task will be complicated with unorganized ray vectors such as those reflected from surfaces with random errors.

For the case of ideal paraboloidal reflector, we have compared our numerical results with those from obtained from analysis. The good agreement so far is a confirmation that our results will be acceptable in the fine limit. After we incorporate random errors into the reflector surface, the results will be compared with those obtained from PO.

Chapter 3

Generation of the Gaussian random surfaces

To study the effect of random surface errors on the radiation pattern by Monte Carlo simulation, a number of random surfaces will be created. These random surfaces will be added to the surface of a paraboloidal reflector. This chapter describes a procedure to generate the Gaussian random surfaces, which is believed to be the most realistic model for the random surface errors [11]. We begin with a mathematical description of the Gaussian random surfaces, which have a Gaussian height distribution and a Gaussian correlation function. Next we describe a scheme to generate random surfaces with specified correlation characteristic from a given correlation function. Finally, we describe the procedure that we use to generate the Gaussian random surfaces and their parameters. The computer-generated results will be verified with the theory for their characteristics.

3.1 Mathematical description of the Gaussian random surfaces

The Gaussian random surfaces are characterized by the Gaussian distributed height and the Gaussian correlation function between any two points on the random surfaces [7]. For any two points (x_1, y_1) and (x_2, y_2) on a Gaussian random surface, the joint probability density function (pdf) is given by

$$p_{g_1,g_2}(g_1(x_1,y_1), g_2(x_2,y_2)) = \frac{1}{2\pi\sigma^2\sqrt{1-C^2}} e^{-(g_1^2-2Cg_1g_2+g_2^2)/2\sigma^2(1-C^2)} \tag{3.1}$$

where g_1 and g_2, the heights at point 1 and point 2 respectively, are random variables with a zero mean, C is the correlation coefficient defined as $C = \dfrac{< g_1 g_2 >}{\sigma^2}$, $\sigma^2 =< g^2 >$ is the variance of the random height, which will be assumed the same at every point on the surface, and the angle brackets denote ensemble averaging.

Equation (3.1) specifies the probability that the random surface will have its height between g_1 and $g_1 + dg$ at point 1 and between g_2 and $g_2 + dg$ at point 2. The marginal height probability density function is obtained by integrating Equation (3.1) over all possible values of g_2. We obtain the following Gaussian distribution for the surface height at a single point

$$p_g(g_1(x,y)) = \frac{1}{\sqrt{2\pi\sigma^2}} e^{-g_1^2/2\sigma^2} \tag{3.2}$$

Many random surfaces can be treated as statistically homogeneous, meaning that the surface statistics are independent of the locations on the surfaces. For such surfaces, the marginal height pdf is the same everywhere, and the correlation function C is a function of the distance between the two points. For the Gaussian random surfaces, the correlation function $C(\rho)$ is assumed to have the following Gaussian form

$$C(\rho) = e^{-\rho^2/l^2} \tag{3.3}$$

where l is the correlation length. Note that $C(0) = 1$ and $C(\infty) = 0$, which means that the random surfaces are less correlated with themselves when the correlation distances get larger.

3.2 Generation of random surfaces with specified correlation functions

In this section, we describe a scheme to generate random surfaces with specified correlation functions from a random surface with independent random heights. Assuming that we have a surface with independent random heights, we will use the concept of digital filtering to correlate these independent random inputs. The height of the output surface will be correlated according to the coefficients of the filter, which are determined from the specified correlation function [41][42]. The actual height distribution of the output random surface will depend on the length and the shape of the filter.

The output from filtering an input surface $h_{j,m}$ with a two-dimensional digital filter $W_{j,m}$

is expressed by

$$g_{k,l} = \sum_{j=1}^{N} \sum_{m=1}^{N} W_{j,m} h_{k-j,l-m} \tag{3.4}$$

The autocorrelation $C_{i,n}$ of the output is

$$C_{i,n} = E[g_{k,l} g_{k+i,l+n}] = \sum_{j=1}^{N} \sum_{m=1}^{N} \sum_{p=1}^{N} \sum_{q=1}^{N} W_{j,m} W_{p,q} E[h_{j+k,m+l} h_{p+k+i,q+l+n}] \tag{3.5}$$

Since the heights of the input surface are mutually independent, i.e.,

$$E[h_{j+k,m+l} h_{p+k+i,q+l+n}] = \begin{cases} 0, & j \neq p+i \,\mathrm{or}\, m \neq q+n \\ 1, & j = p+i \,\mathrm{or}\, m = q+n \end{cases} \tag{3.6}$$

the autocorrelation in Equation (3.5) can be simplified to

$$C_{i,n} = E[g_{k,l} g_{k+i,l+n}] = \sum_{j=1}^{N} \sum_{m=1}^{N} W_{j,m} W_{j-i,m-n} \tag{3.7}$$

By assuming that the filter is symmetric, i.e., $W_{j-i,m-n} = W_{i-j,n-m}$, Equation (3.7) can be written as

$$C_{i,n} = \sum_{j=1}^{N} \sum_{m=1}^{N} W_{j,m} W_{i-j,n-m} \tag{3.8}$$

which tells us that the autocorrelation function $C_{i,n}$ is the two-dimensional convolution of the digital filter $W_{j,m}$ with itself.

Next, we determine the filter coefficients $W_{j,m}$ from a given correlation function $C_{i,n}$. We will assume that $C_{i,n}$ are uniform samples of a continuous function $C(u,v)$, and $W_{j,m}$ are also samples of $W(u,v)$. From Equation (3.8), the Fourier transform of $C(u,v)$ is equal to a square of the magnitude of the Fourier transform of $W(u,v)$ [43]. Thus $W(u,v)$ is the inverse Fourier transform of the square root of the Fourier transform of the continuous correlation function $C(u,v)$, i.e., $W_{j,m}$ are samples of the function

$$W(u,v) = \mathcal{F}^{-1}\{\sqrt{\mathcal{F}\{C(u,v)\}}\} \tag{3.9}$$

where $\mathcal{F}$ and $\mathcal{F}^{-1}$ signify the Fourier transform and inverse Fourier transform operations respectively.[1] This approach is valid when the correlation functions and the filter coefficients are non-negative, which is the case for the Gaussian correlation functions as we will illustrate in the next section.

3.3 Procedure to generate the Gaussian random surfaces

In this section, we describe the procedure and the parameters used to generate the Gaussian random surfaces. The output surfaces are verified by being compared with the specifications and the theoretical values.

Let the Gaussian random surface with a zero mean and a unit standard deviation be represented by a matrix g. The elements $g_{k,l}$ of the matrix are distributed according to the

---

[1] The two-dimensional Fourier transform pair are defined as follow

$$F(\zeta,\xi) = \mathcal{F}\{f(u,v)\} = \int_{-\infty}^{\infty}\int_{-\infty}^{\infty} f(u,v)e^{-i2\pi\zeta u - i2\pi\xi v}dudv \tag{3.10}$$

$$f(u,v) = \mathcal{F}^{-1}\{F(\zeta,\xi)\} = \int_{-\infty}^{\infty}\int_{-\infty}^{\infty} F(\zeta,\xi)e^{i2\pi u\zeta + i2\pi v\xi}d\zeta d\xi \tag{3.11}$$

following probability density function

$$p_g(g_{k,l}) = \frac{1}{\sqrt{2\pi}} e^{-g^2/2} \tag{3.12}$$

The elements are correlated according to the discrete Gaussian correlation function, which is given by

$$C_{i,n} = exp\left[-\left(\frac{i}{l_1}\right)^2 - \left(\frac{n}{l_2}\right)^2\right] \tag{3.13}$$

where l_1, l_2 are correlation lengths in the x- and y-directions respectively. Note that Equation (3.13) is the discrete version of the continuous correlation function in Equation (3.3).

Equation (3.9) suggests that we can find the filter coefficients $W_{j,m}$ from the discrete correlation function in Equation (3.13). Since the Gaussian correlation function can be separated into a product of two single-variable functions, we will derive the expression for $W_{j,m}$ from the one-dimensional case. From Equation (3.3), the autocorrelation in the x direction is

$$C(u) = e^{-(u/l_1)^2} \tag{3.14}$$

The filter coefficients W_j are obtained from a uniform samples of

$$\begin{aligned} W(u) &= \mathcal{F}^{-1}\{\sqrt{\mathcal{F}\{e^{-(u/l_1)^2}\}}\} \\ &= \mathcal{F}^{-1}\{\sqrt{l_1\sqrt{\pi}e^{-(\pi l_1 \zeta)^2}}\} \\ &= \sqrt{\frac{2}{l_1\sqrt{\pi}}} e^{-2(u/l_1)^2} \end{aligned} \tag{3.15}$$

and are expressed by

$$W_j = \sqrt{\frac{2}{l_1\sqrt{\pi}}}\, exp\left[-2\left(\frac{j}{l_1}\right)^2\right] \tag{3.16}$$

The two-dimensional filter coefficients $W_{j,m}$ are products of coefficients from two one-dimensional filters

$$\begin{aligned} W_{j,m} &= W_j W_m \\ &= \frac{2}{\sqrt{\pi l_1 l_2}}\, exp\left[-2\left(\frac{j}{l_1}\right)^2 - 2\left(\frac{m}{l_2}\right)^2\right] \end{aligned} \tag{3.17}$$

In the computer program, we create a random matrix with independently and identically distributed (IID) elements at the first step. There are many standard procedures to generate independent random numbers with various kinds of distribution to choose from[44], and we choose one giving a uniformly distributed random numbers. Then we compute a 2-D convolution between the random matrix and the correlation filter, whose coefficients are calculated according to Equation (3.17). The correlation lengths l_1 and l_2 are chosen to be 4 units, with a unit length equal to the distance of 10 discrete intervals between the elements of the matrix. Figure 3-1 shows the correlation filter with size $M \times M = 120 \times 120$. The output matrix is normalized so that it has a zero mean and a unit standard deviation. Figure 3-2 and Figure 3-3 display two profiles of the computer-generated random surfaces with $\sigma = 1.0$ and with matrix size $N \times N = 400 \times 400$. The figures show they are distinct, and the changes on the surfaces appear to be sufficiently smooth. The many local bumps also have the look of a 2-D bell-shaped curve.

In order to verify the output surfaces, their statistical characteristics will be computed to compare with the theoretical values. These characteristics include the surface height distribution, the correlation coefficients in the x-, y-, and xy-directions, and the distribution of the surface slopes.

Because each element on the output matrix is a weighted sum of independent random elements, the output surface should have a Gaussian height distribution according to the Central Limit Theorem [42][45]. The size of the correlation filter should be large enough to make the actual results agree with the theory. Figure 3-4 and Figure 3-5 show the distributions of the height of the computer-generated surfaces displayed in Figure 3-2 and Figure 3-3. The distributions are compared with the Gaussian probability density function with $\mu = 0$ and $\sigma = 1.0$. Figure 3-6 shows the average height distribution of 20 surface profiles compared with the Gaussian pdf. Figure 3-7 shows a comparison between the correlation coefficients of the output in the x- and y-directions and the Gaussian autocorrelation function in Equation (3.13). Figure 3-8 shows a comparison between the correlation in the xy-direction and its theoretical values derived from Equation (3.13). In both cases, the computer-generated results agree well with the specification, especially when the distance is less than twice the correlation length.

Because any linear transformation of a Gaussian function remains a Gaussian function, the slopes and all the higher order derivatives of a Gaussian random surface will also have a Gaussian distribution [46]. The probability density function for the slopes of a Gaussian random surface can be derived from Equation (3.1) and is equal to [47]

$$p(\alpha, \beta) = \frac{1}{2\pi\sigma^2|C''(0)|} exp\left[-\frac{\alpha^2+\beta^2}{2\sigma^2|C''(0)|}\right] \tag{3.18}$$

where σ is the standard deviation of the height of the random surface, $C''(0)$ is the double derivative of the correlation function at $\rho = 0$, which is equal to $-2l^2$, and $\alpha = \dfrac{\partial f(x,y)}{\partial x}$ and $\beta = \dfrac{\partial f(x,y)}{\partial y}$ are the local slopes in the x- and y-directions. For the Gaussian correlation function with correlation length l, $\sigma^2|C''(0)|$ is the mean-square slope and is equal to

$$s^2 = \sigma^2 |C''(0)| = \frac{2\sigma^2}{l^2} \tag{3.19}$$

Figure 3-9 and Figure 3-10 show the average distribution of the local slope in the x- and y-directions respectively from 20 computer-generated Gaussian random surfaces. They are compared with the Gaussian pdf with $\mu = 0.0$ and $\sigma = s = \sqrt{2}/40$. The good agreement suggests that the mean-square slope of the computer-generated Gaussian surfaces is practically the same as the theoretical value.

Thus, we have succeeded in creating Gaussian random surfaces with a zero mean and a unit variance. The above verifications show that the random surfaces generated by the previously described procedures have the characteristics of the Gaussian random surfaces. So an ensemble of these surfaces can be used to study the effects of the random surface errors on the radiation patterns by the Monte Carlo simulation. The roughness of the random surfaces can be adjusted by changing the root-mean-square height and the correlation length. The former can be done easily by multiplying the elements of the standard random surfaces with the new rms value.

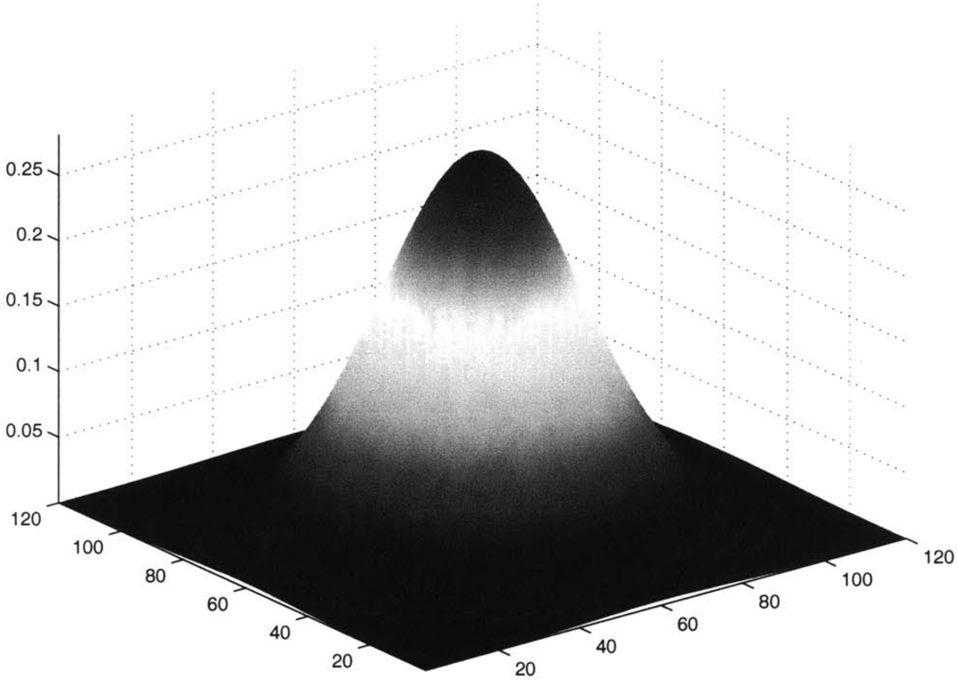

Figure 3-1: The correlation filter. The dimension is $M \times M = 120 \times 120$, and the correlation lengths are $l_1 = l_2 = 4$ units (= 40 intervals).

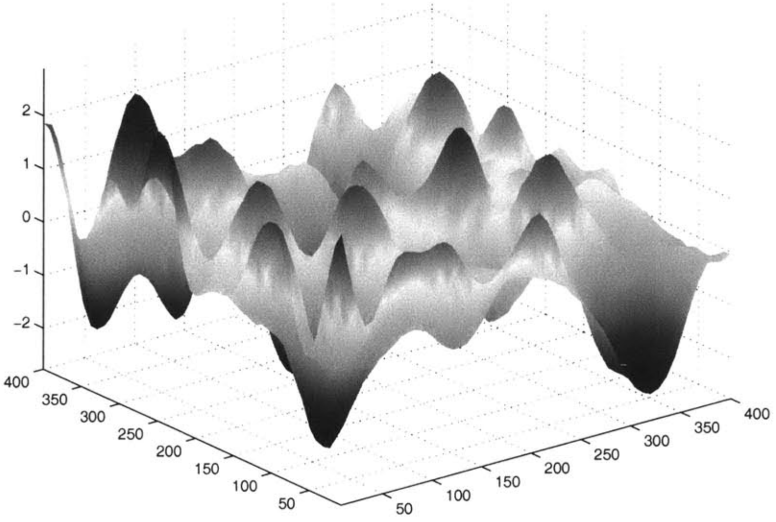

Figure 3-2: Example of a computer-generated Gaussian random surface with variance $\sigma^2 = 1.0$ and correlation lengths $l_1 = l_2 = 4$ units (= 40 intervals). The filter size is $M \times M = 120 \times 120$, and the size of the surface is $N \times N = 400 \times 400$.

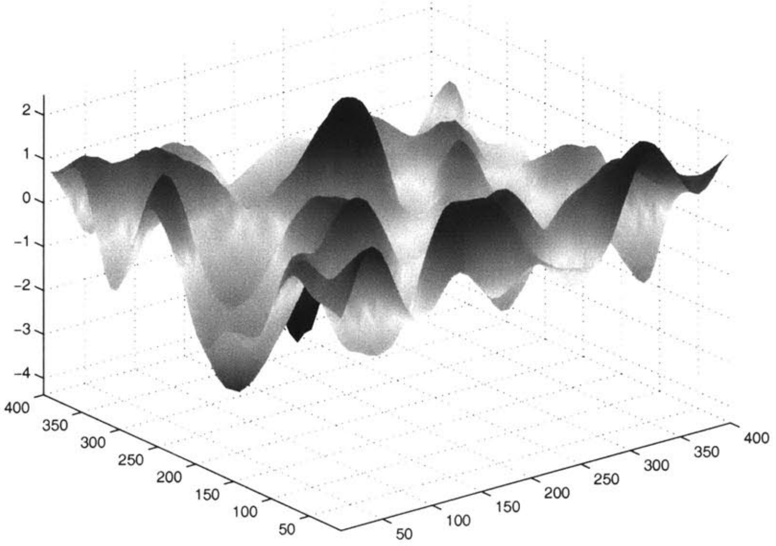

Figure 3-3: Another example of a computer-generated Gaussian random surface.

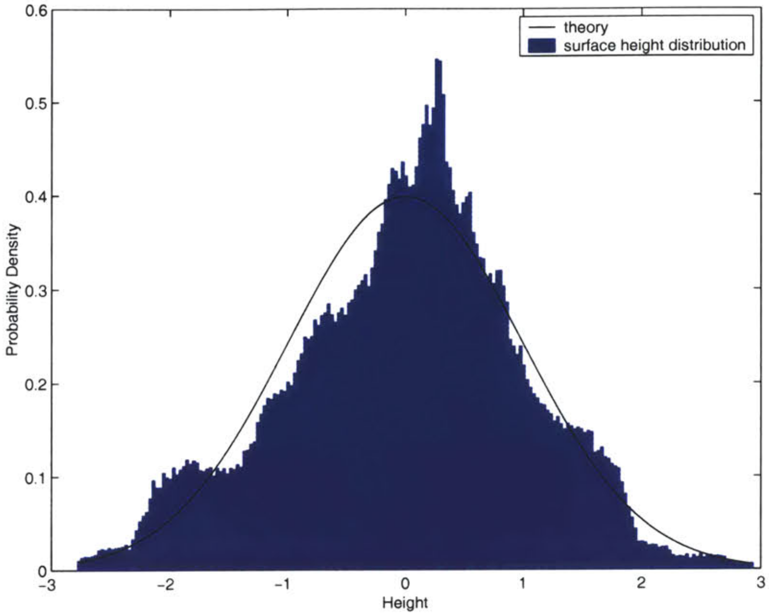

Figure 3-4: Height distribution of the random surface in Figure 3-2 compared with the Gaussian pdf ($\mu = 0.0, \sigma = 1.0$).

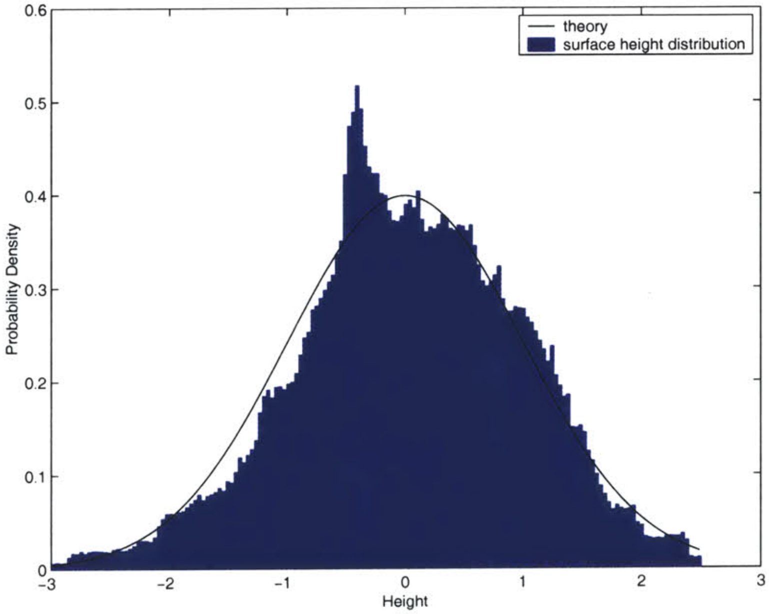

Figure 3-5: Height distribution of the random surface in Figure 3-3 compared with the Gaussian pdf ($\mu = 0.0, \sigma = 1.0$).

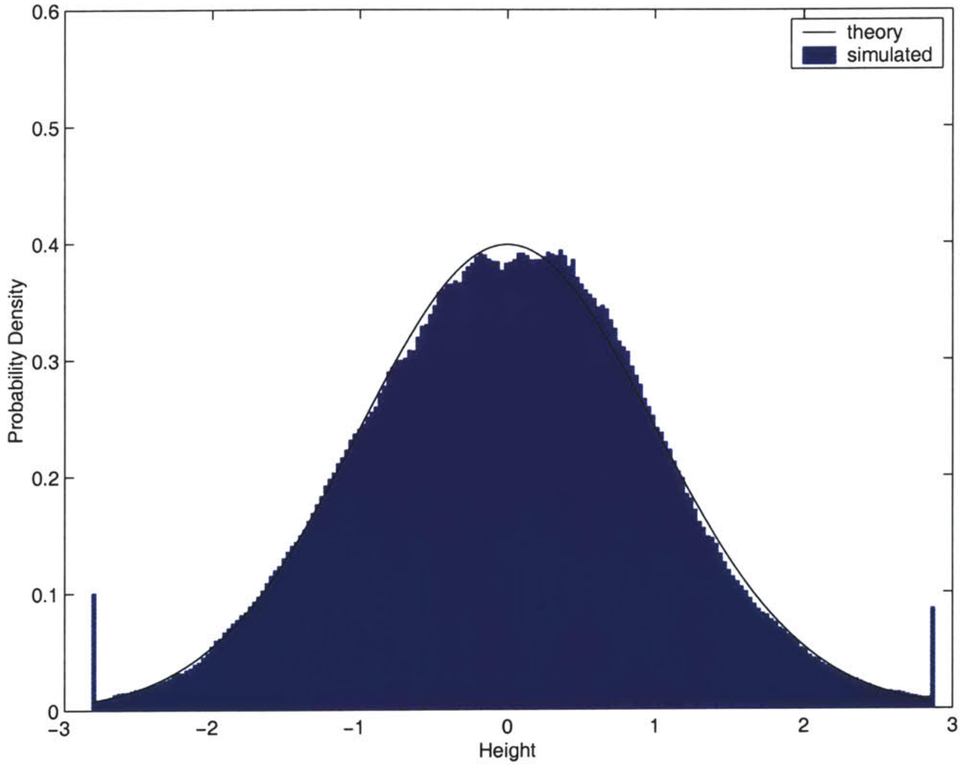

Figure 3-6: Height distribution of the random surfaces on average obtained from 20 samples compared with the Gaussian pdf ($\mu = 0.0, \sigma = 1.0$).

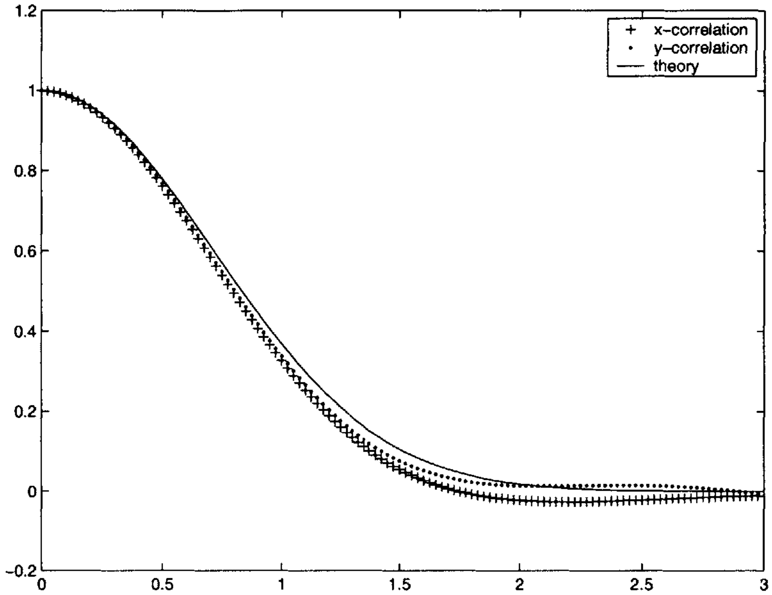

Figure 3-7: The autocorrelation of the random surfaces in the x- and y-directions compared with the Gaussian correlation function. The autocorrelation is obtained from an ensemble of 20 surface profiles.

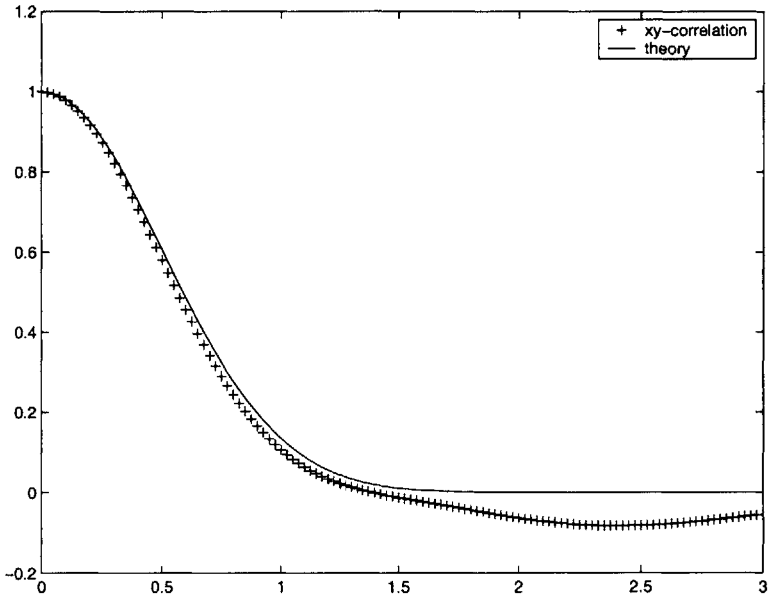

Figure 3-8: The autocorrelation of the random surfaces in the xy-direction (the diagonal direction) compared with the Gaussian correlation function.

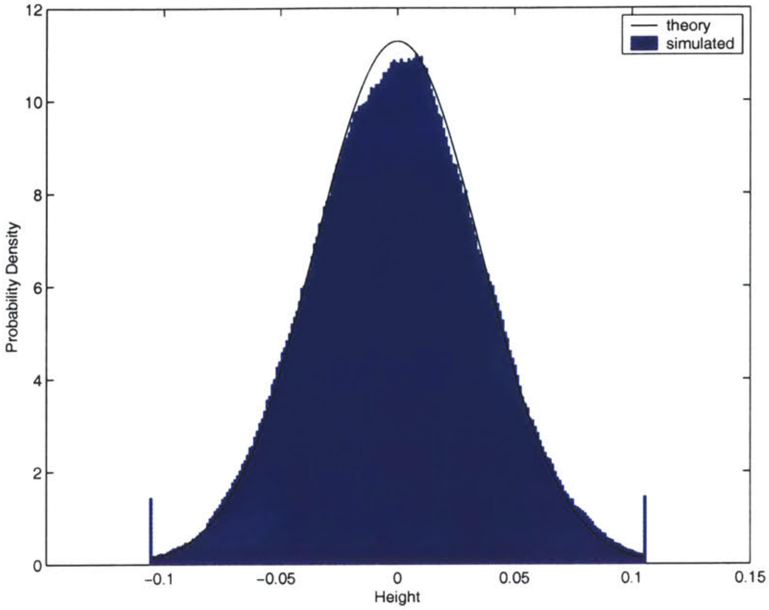

Figure 3-9: Distribution of the local slope in the x-direction on average obtained from 20 samples compared with the Gaussian pdf ($\mu = 0.0, \sigma = \sqrt{2}/40$).

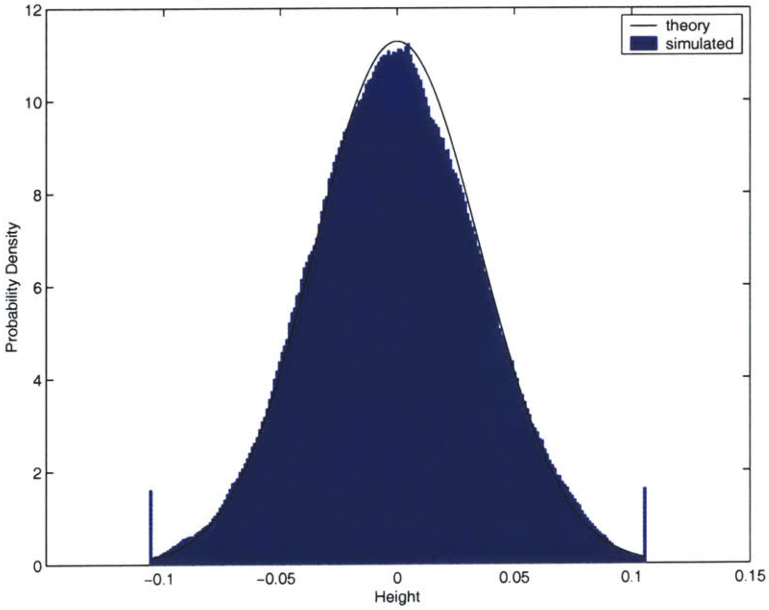

Figure 3-10: Distribution of the local slope in the y-direction obtained from 20 samples compared with the Gaussian pdf ($\mu = 0.0, \sigma = \sqrt{2}/40$).

Chapter 4

Effects of random surface errors on the radiation patterns

In this chapter, we will use the model developed in Chapter 2 to compute the radiation fields from a paraboloidal reflector with random surface errors of the Gaussian characteristics described in the previous chapter. After some adjustment are made to incorporate the surface errors to the paraboloidal reflector, results from the Monte Carlo simulation will be presented. They will be compared with results obtained from the antenna tolerance theory.

4.1 Incorporation of the random surfaces to the paraboloidal surface

The Gaussian random surfaces with appropriate parameters will be added to the surface of a paraboloidal reflector surface to study the effects of random surface errors on the radiation patterns. The incorporation of the surface errors will change the locations of the points of incidence and the normal vectors at those points. These changes will affect both the GO and PO approaches to the analysis of radiation patterns. They will have more significant effect on the positions, phases, and polarizations of the current elements for both GO and PO, and with very little effect on the amplitude.

4.1.1 Change of locations of the incident points

The local deviation on the reflector surface at the point of incidence (x'_0, y'_0, z'_0) will be determined from the two-dimensional random surface by the method of bilinear interpolation [44]. Bilinear interpolation is a method to approximate the height of a point in a rectangular grid from the coordinates and the heights of the corner points. Alternatively, a number of curve-fitting schemes have been suggested in some similar studies [48][31][14], but bilinear interpolation can be used in situations where the first-order level of accuracy is sufficient.

Let $\overline{P}_0 = (x'_0, y'_0, z'_0)$ be a point of incidence on the zero-error paraboloidal surface, and h be the local surface deviation in the direction perpendicular to the paraboloidal surface as shown in Figure 4-1. The point of incidence will be moved to a new location $\overline{P}_1 = (x'_1, y'_1, z'_1)$, which is related to $\overline{P}_0$ by

$$\begin{aligned} \overline{P}_1 &= \overline{P}_0 + \hat{s}_i\, l \\ &= \overline{P}_0 - \hat{s}_i \frac{h}{\hat{s}_i \cdot \hat{n}_0} \end{aligned} \tag{4.1}$$

where l is the distance between $\overline{P}_0$ and $\overline{P}_1$ along the direction of the incident ray vector.

The local deviation h will be determined from the uniform samples $g_{i,j}$ of the Gaussian random surface $g(x', y')$. A point of incidence will fall into one of the grids formed by the sampling intervals (see Figure 4-2). Four corners of the grid are denoted by, starting from the lower-left corner and moving counterclockwise, $g_1 = g_{i,j} = g(x'_j, y'_i)$, $g_2 = g_{j+1,i} = g(x'_{j+1}, y'_i)$, $g_3 = g_{j+1,i-1} = g(x'_{j+1}, y'_{i-1})$, and $g_4 = g_{j,i-1} = g(x'_j, y'_{i-1})$. The indices i, j are determined from the location of $\overline{P}_0$, the size of the random matrix N, and the diameter of the dish D as follow

$$i = \left\lceil -\frac{N-1}{D} y'_0 + \frac{N+1}{2} \right\rceil \qquad (4.2)$$

$$j = \left\lfloor \frac{N-1}{D} x'_0 + \frac{N+1}{2} \right\rfloor \qquad (4.3)$$

After the indices are obtained, the coordinates of the lower-left corner are determined from

$$x'_j = \left(j - \frac{N+1}{2} \right) \frac{D}{N-1} \qquad (4.4)$$

$$y'_i = -\left(i - \frac{N+1}{2} \right) \frac{D}{N-1} \qquad (4.5)$$

The coordinates of the remaining corners can be determined by adding or subtracting the increment of $D/(N-1)$ from x'_j and y'_i according to Figure 4-2. The local height deviation will be approximated by bilinear interpolation according to the formula [44]

$$h(x', y') = (1-t)(1-u)g_1 + t(1-u)g_2 + tug_3 + (1-t)ug_4 \qquad (4.6)$$

where g_i are the heights of the random surface at the corners, and $0 \leq t, u \leq 1$.

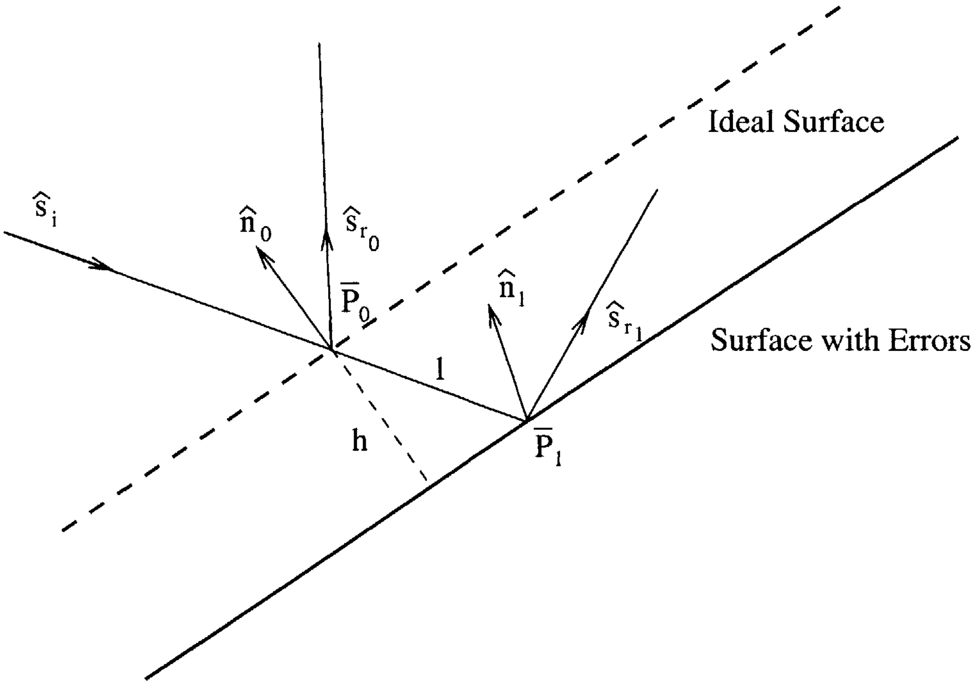

Figure 4-1: Changes in the location of a point of reflection and in the direction of the reflected ray vector due to the incorporation of surface errors with the paraboloidal surface. $\overline{P}_0$, $\hat{n}_0$, and $\hat{s}_{r_0}$ are the point of incidence, the unit normal vector, and the reflected ray vector on the ideal reflector surface. $\overline{P}_1$, $\hat{n}_1$, and $\hat{s}_{r_1}$ are the point of incidence, the unit normal vector, and the reflected ray vector on the reflector surface with surface errors.

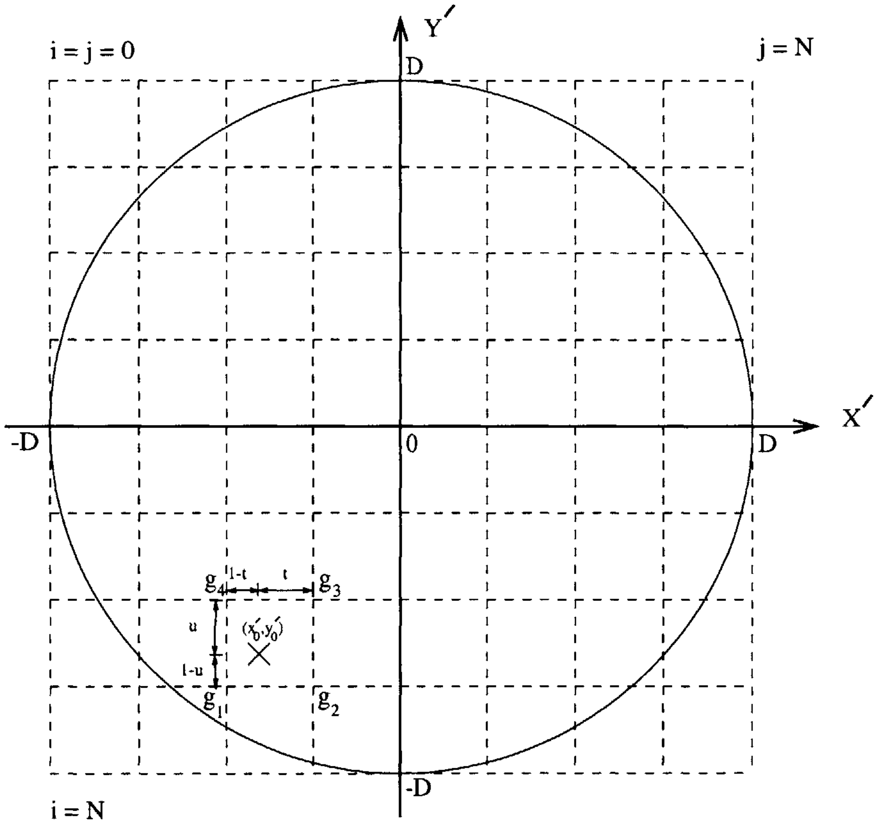

Figure 4-2: A random surface is mapped vertically onto the paraboloidal surface. The cross is the position of a point of incidence, which will be used to determine the corners of the grid.

4.1.2 Change of the normal vectors

The addition of the random surface errors onto the surface of the paraboloidal reflector will change the direction of the normal vectors at the points of incidence, which in turn will change the direction of the reflected rays. In order to simplify the analysis, we use a different assumption in the way we add the random surface to the surface of the paraboloid. The random surface will be added to the paraboloidal surface in the direction of the main axis as if the surface errors were measured in that direction. The resulting surface will be expressed by

$$f_1(x', y') = f_0(x', y') + g(x', y') \tag{4.7}$$

where $g(x', y')$ represents the random surface, $f_0(x', y')$ is the ideal paraboloidal surface, and $f_1(x', y')$ is the paraboloidal surface with random errors. The unit normal vector $\hat{n}_1$ on the modified surface is given by

$$\hat{n}_1 = \frac{\hat{x}\,\alpha_1 + \hat{y}\,\beta_1 - \hat{z}}{\sqrt{\alpha_1^2 + \beta_1^2 + 1}} \tag{4.8}$$

where $\alpha_1 = \dfrac{\partial f_1(x', y')}{\partial x'} = \dfrac{\partial f_0(x', y')}{\partial x'} + \dfrac{\partial g(x', y')}{\partial x'}$ and $\beta_1 = \dfrac{\partial f_1(x', y')}{\partial y'} = \dfrac{\partial f_0(x', y')}{\partial y'} + \dfrac{\partial g(x', y')}{\partial y'}$.
The partial derivatives of the paraboloidal surface can be expressed by

$$\begin{aligned}\frac{\partial f_0(x', y')}{\partial x'} &= \frac{(4f^2 - x'^2 - y'^2)/4f}{\partial x'} \\ &= \frac{-x'}{2f} \\ &= \tan\frac{\theta'}{2}\cos\phi' \end{aligned} \tag{4.9}$$

and

$$\begin{aligned}\frac{\partial f_0(x',y')}{\partial y'} &= \frac{(4f^2 - x'^2 - y'^2)/4f}{\partial y'} \\ &= \frac{-y'}{2f} \\ &= \tan\frac{\theta'}{2}\sin\phi' \end{aligned} \tag{4.10}$$

where we use $x' = \rho' \cos\phi' = 2f\tan(\theta'/2)\cos\phi'$ and $y' = \rho' \sin\phi' = 2f\tan(\theta'/2)\sin\phi'$ to get the results above. The partial derivatives $\frac{\partial g(x',y')}{\partial x'}$ and $\frac{\partial g(x',y')}{\partial y'}$ at the point of incidence (x'_0, y'_0, z'_0) can be approximated to the first order by using a method borrowed from the bilinear interpolation with the following formula

$$\frac{\partial g}{\partial x'} = \frac{(1-u)g_2 + ug_3 - (1-u)g_1 - ug_4}{D/(N-1)} \tag{4.11}$$

$$\frac{\partial g}{\partial y'} = \frac{(1-t)g_4 + tg_3 - (1-t)g_1 - tg_2}{D/(N-1)} \tag{4.12}$$

4.2 Results from the Monte Carlo simulation

An ensemble of random surfaces created in the previous chapter will be used to simulate the random surface errors. The different root-mean-square surface values are achieved by multiplying elements of the standard Gaussian random surfaces by ε_{rms}, which is the ratio between the rms surface error and the wavelength. For each rms value, one hundred samples will be used in the Monte Carlo simulation.

Figure 4-3 and Figure 4-4 show the changes that the random surface errors with $\varepsilon_{rms} = 0.005\lambda$ and $\varepsilon_{rms} = 0.05\lambda$ brought on the distribution of the electric dipoles in Figure 2-12.

The change is obscure in the first case where ε_{rms} is less than $\lambda/100$ but looks more obvious when ε_{rms} is ten times larger.

Figure 4-5 and Figure 4-6 show the co-polarized radiation patterns on the E-plane form the distributions of dipoles in Figure 4-3 and Figure 4-4 respectively. The patterns in the first figure ($\varepsilon_{rms} = 0.005\lambda$) are almost identical to each other and to the ideal pattern. However there are several obvious changes in the second figure ($\varepsilon_{rms} = 0.05\lambda$). First, the maximum gain are reduced from the ideal case for both GO and PO by similar amount. Second, the levels and locations of the peak side lobe are very different from the ideal pattern. Third, the GO and PO patterns are in good agreement until the observation angle $\theta \approx 5^\circ$ where they begin to diverge.

Figures 4-7 to 4-12 show average gain patterns from a paraboloidal reflector with different degrees of random surface errors on the E-, H-, and 45-degree planes. The patterns are obtained from the GO ray tracing formulated in Chapter 2. The co-polarized patterns show a steady reduction in peak gain and increase in the levels of side lobes with the rising level of ε_{rms} in all planes of observation. The null positions are almost unchanged for the co-polarized patterns. The cross-polarized patterns show a steady on-average increase in all planes of observation. The level of the on-axis ($\theta = 0$) cross-polarization increases almost linearly in the log scale, corresponding to the similar way ε_{rms} increases. Similar trends appear for patterns from PO in Figures 4-13 to 4-18, which show average gain patterns from a paraboloidal reflector with different degrees of random surface errors on the E-, H-, and 45-degree planes.

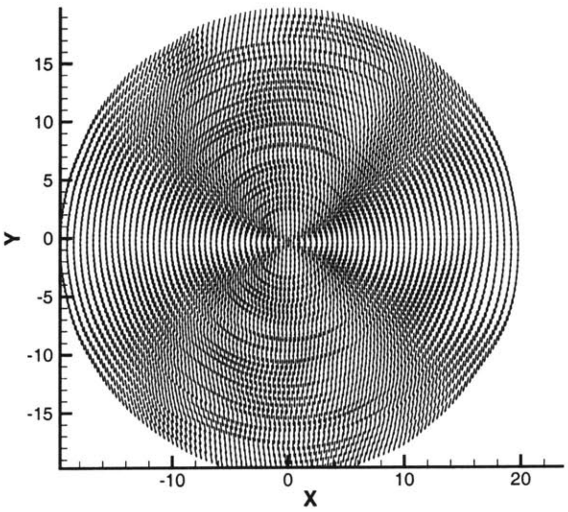

Figure 4-3: The effect of random surface errors ($\varepsilon_{rms} = 0.005\lambda$) on the distribution of equivalent electric dipoles on the aperture plane.

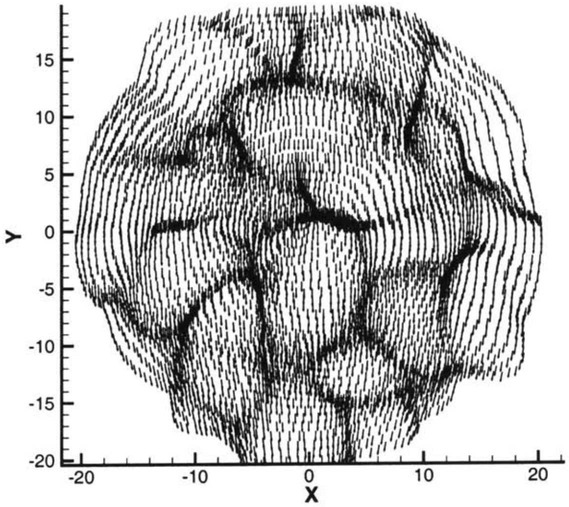

Figure 4-4: The effect of random surface errors ($\varepsilon_{rms} = 0.05\lambda$) on the distribution of equivalent electric dipoles on the aperture plane.

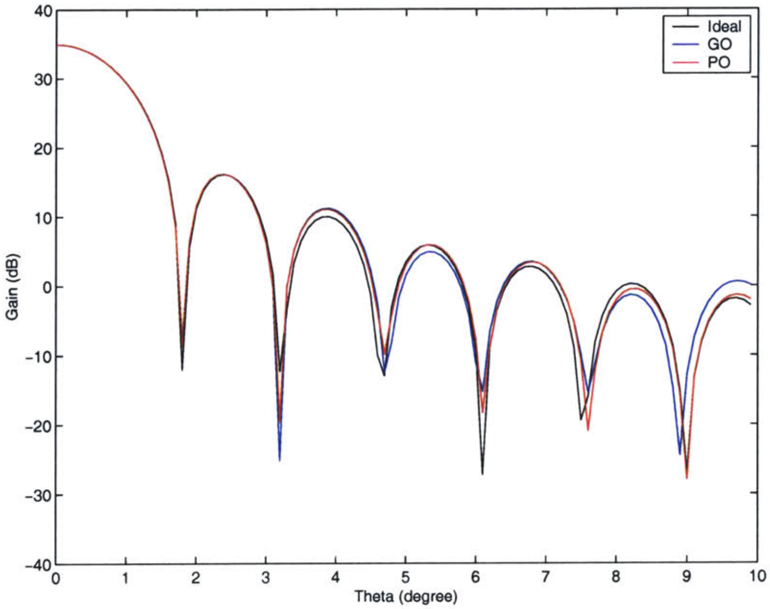

Figure 4-5: Comparison of GO and PO gain patterns of the co-polarized field on the E-plane from a paraboloidal reflector with $\varepsilon_{rms} = 0.005\lambda$.

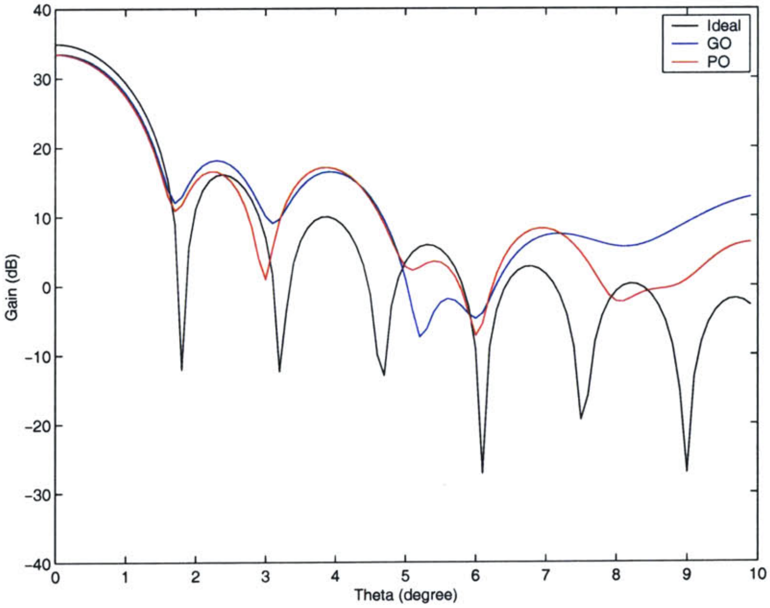

Figure 4-6: Comparison of GO and PO gain patterns of the co-polarized field on the E-plane from a paraboloidal reflector with $\varepsilon_{rms} = 0.05\lambda$.

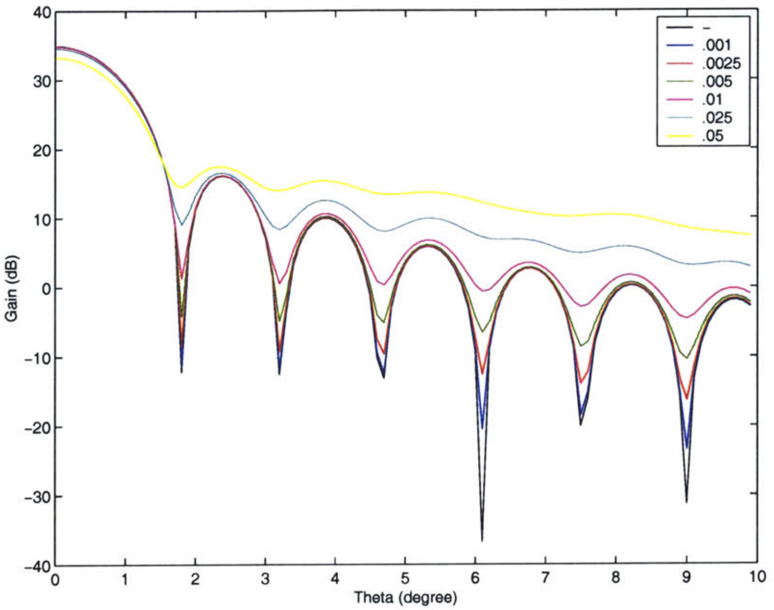

Figure 4-7: Average gain patterns of the co-polarized field on the E-plane from a paraboloidal reflector with various degrees of random surface errors. The patterns are obtained from the GO ray tracing model.

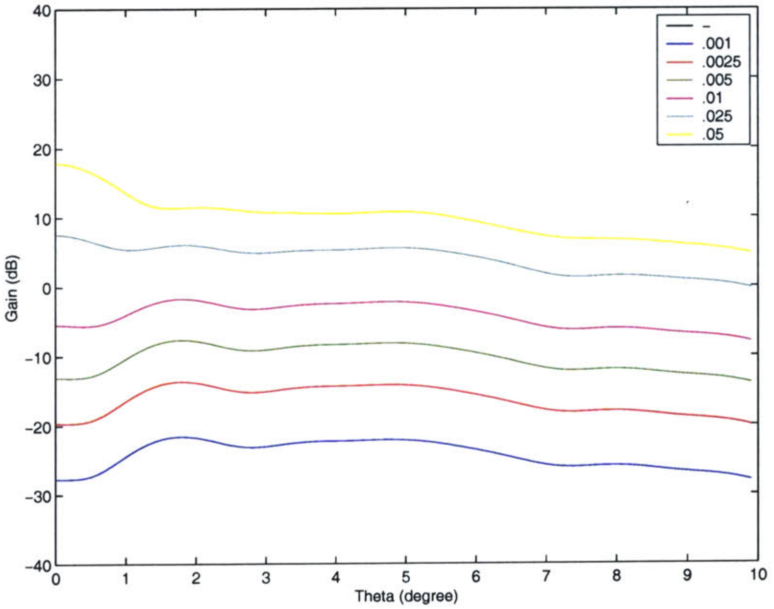

Figure 4-8: Average gain patterns of the cross-polarized field on the E-plane from a paraboloidal reflector with various degrees of random surface errors. The patterns are obtained from the GO ray tracing model.

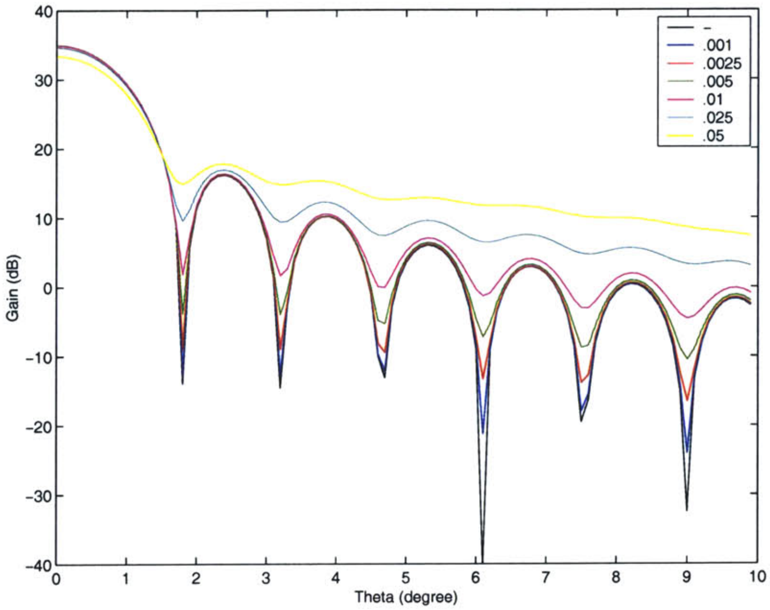

Figure 4-9: Average gain patterns of the co-polarized field on the H-plane from a paraboloidal reflector with various degrees of random surface errors. The patterns are obtained from the GO ray tracing model.

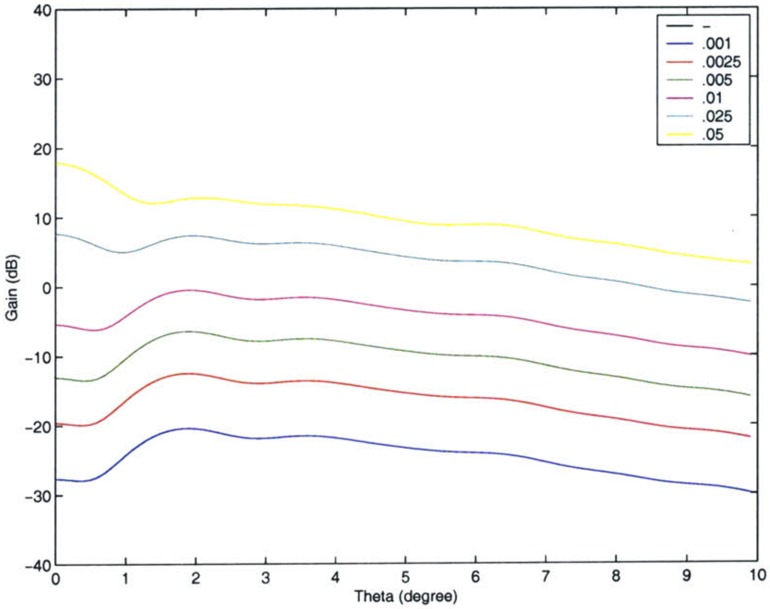

Figure 4-10: Average gain patterns of the cross-polarized field on the H-plane from a paraboloidal reflector with various degrees of random surface errors. The patterns are obtained from the GO ray tracing model.

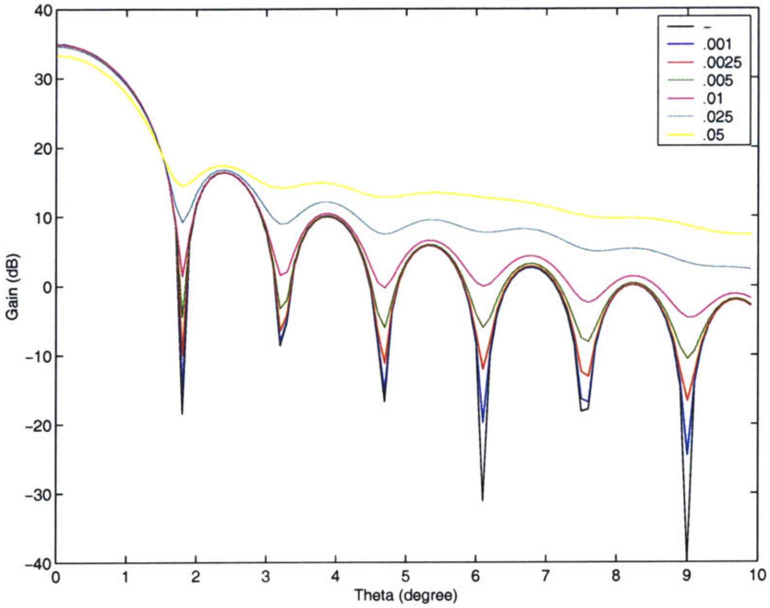

Figure 4-11: Average gain patterns of the co-polarized field on the 45-degree plane from a paraboloidal reflector with various degrees of random surface errors. The patterns are obtained from the GO ray tracing model.

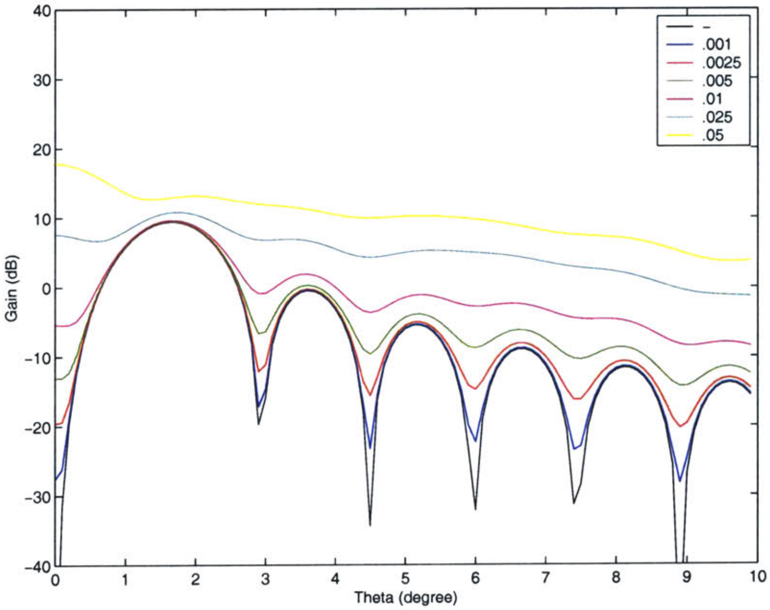

Figure 4-12: Average gain patterns of the cross-polarized field on the 45-degree plane from a paraboloidal reflector with various degrees of random surface errors. The patterns are obtained from the GO ray tracing model.

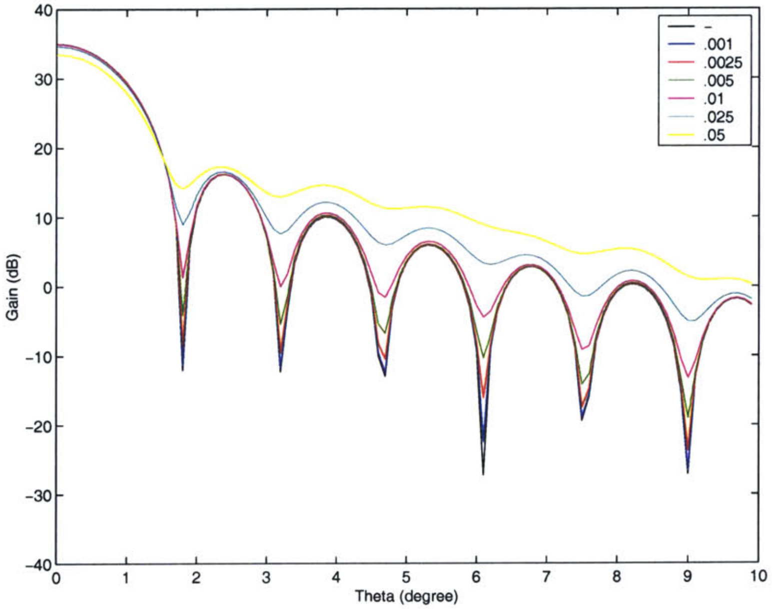

Figure 4-13: Average gain patterns of the co-polarized field on the E-plane from a paraboloidal reflector with various degrees of random surface errors. The patterns are obtained from PO.

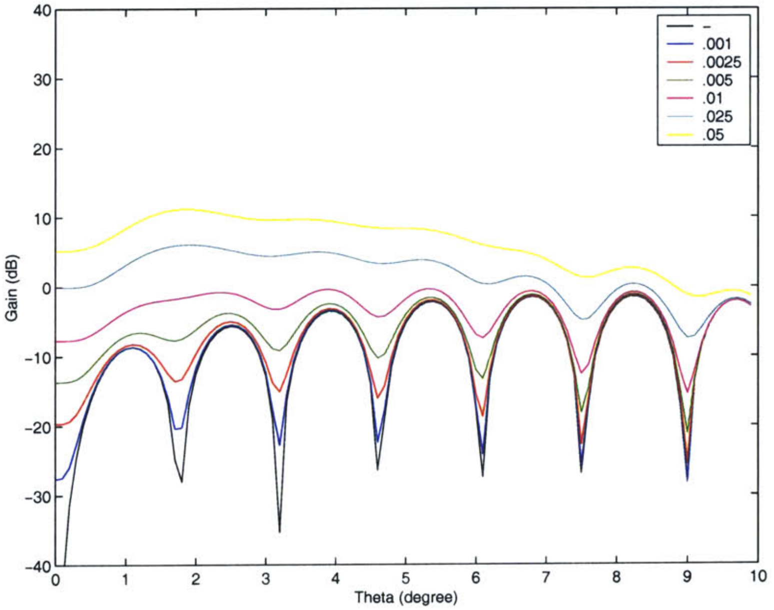

Figure 4-14: Average gain patterns of the cross-polarized field on the E-plane from a paraboloidal reflector with various degrees of random surface errors. The patterns are obtained from PO.

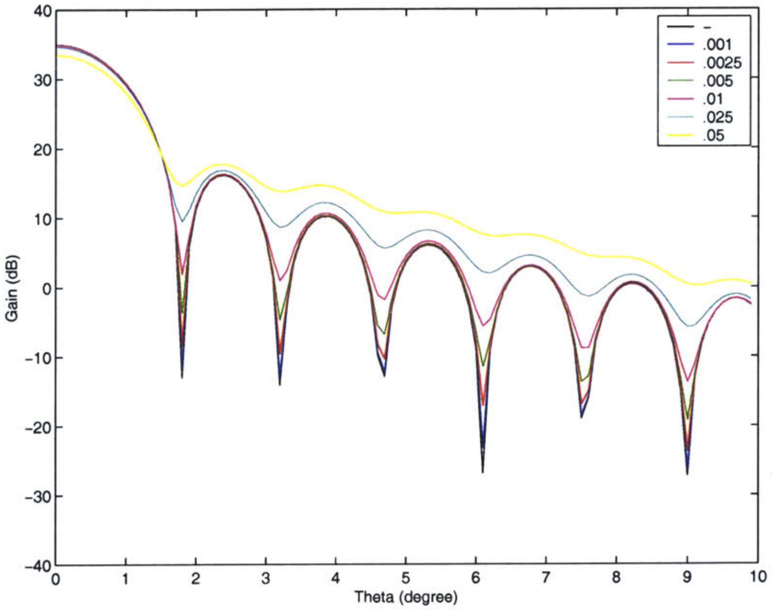

Figure 4-15: Average gain patterns of the co-polarized field on the H-plane from a paraboloidal reflector with various degrees of random surface errors. The patterns are obtained from PO.

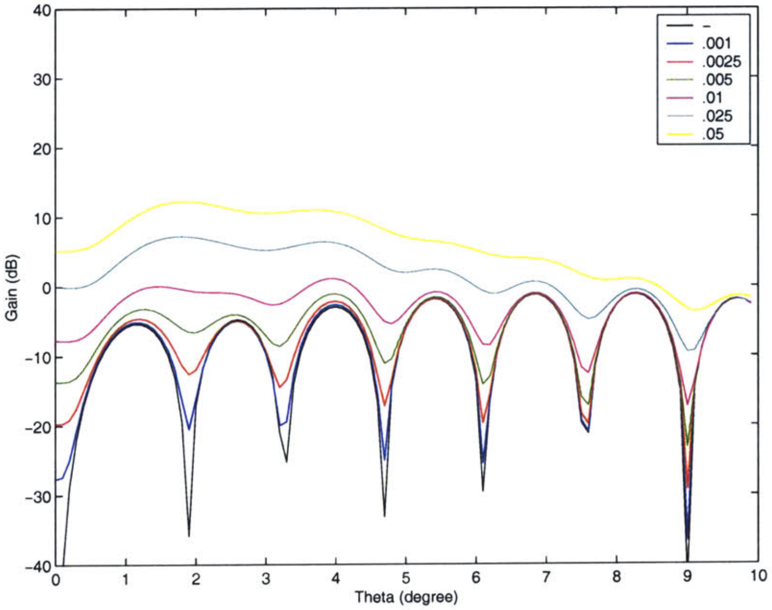

Figure 4-16: Average gain patterns of the cross-polarized field on the H-plane from a paraboloidal reflector with various degrees of random surface errors. The patterns are obtained from PO.

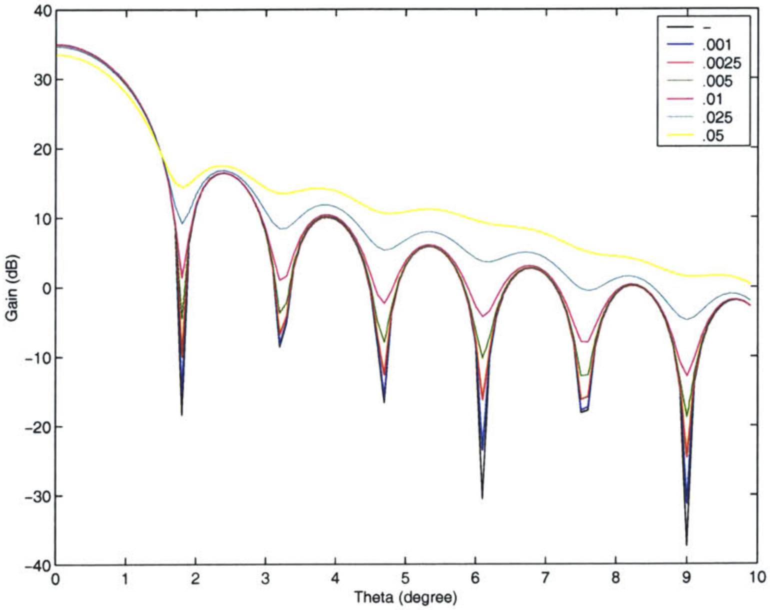

Figure 4-17: Average gain patterns of the co-polarized field on the 45-degree plane from a paraboloidal reflector with various degrees of random surface errors. The patterns are obtained from PO.

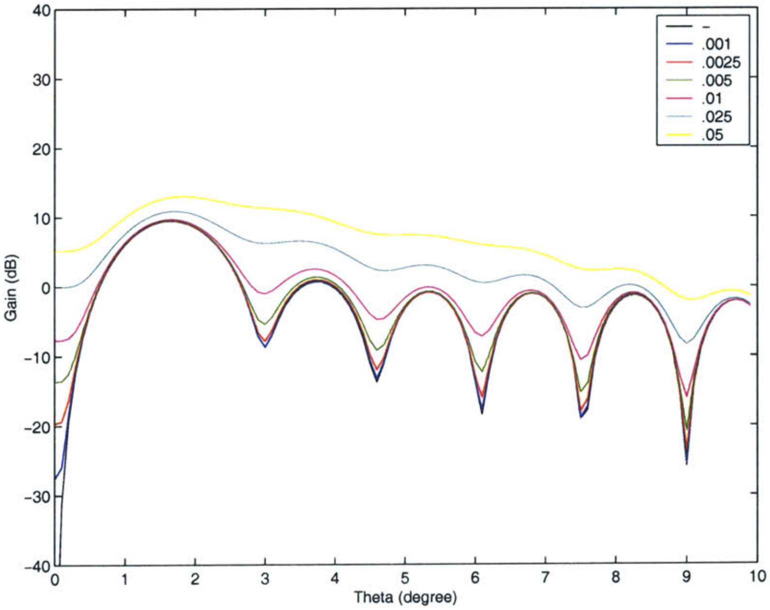

Figure 4-18: Average gain patterns of the cross-polarized field on the 45-degree plane from a paraboloidal reflector with various degrees of random surface errors. The patterns are obtained from PO.

4.3 Comparison with the antenna tolerance theory

We would like to make a comparison between our results and those obtained from the antenna tolerance theory [11]. The antenna tolerance theory predicts the average changes on the radiation pattern as a function of the root-mean-square surface error and its spatial correlation distance. The theory is obtained by analyzing the statistical phase change on the aperture field of the reflector due to the random surface errors. The statistics of the phase deviations is assumed Gaussian, which is the same statistics that we use for creating the random surface errors, making the tolerance theory an analytical approach in close parallel to our proposed scheme.

4.3.1 The antenna tolerance theory

The gain of an aperture antenna with an arbitrary phase error $\delta(\overline{\rho})$ may be written as

$$G(\theta,\phi) = \frac{4\pi}{\lambda^2}\frac{\left|\iint dA\, f(\overline{\rho})e^{-i\overline{k}\cdot\overline{\rho}}e^{i\delta(\overline{\rho})}\right|^2}{\iint dA\, f^2(\overline{\rho})} \tag{4.13}$$

where $\overline{\rho}$ is a position vector on the aperture, $\overline{k}$ is a vector in the direction of observation, $f(\overline{\rho})$ is the aperture illumination function, and $\delta(\overline{\rho})$ is the aperture phase perturbation function. The numerator may be written as

$$\left|\iint dA\, f(\overline{\rho})e^{-i\overline{k}\cdot\overline{\rho}}e^{i\delta(\overline{\rho})}\right|^2 = \iiiint dA_1 dA_\tau f(\bar{\rho}_1)f(\bar{\rho}_1+\bar{\tau})e^{-i\bar{k}\cdot\bar{\rho}}e^{i\gamma(\bar{\tau})} \tag{4.14}$$

where $\overline{\tau} = \overline{\rho}_1 - \overline{\rho}_2$ and $\gamma(\overline{\tau}) = \delta(\overline{\rho}_1) - \delta(\overline{\rho}_2)$.

Let $\Phi(\bar{\tau})$ be the correlation of the illumination function, which is defined as

$$\Phi(\bar{\tau}) = \frac{\iiiint f(\bar{\rho}_1) f(\bar{\rho}_1 + \bar{\tau}) dA_1}{\iint f^2(\bar{\rho}_1) dA_1} \tag{4.15}$$

We can rewrite Equation (4.13) as

$$G(\theta, \phi) = \frac{4\pi}{\lambda^2} \iint dA_\tau \Phi(\bar{\tau}) e^{-i\bar{k}\cdot\bar{\tau}} e^{i\gamma(\bar{\tau})} \tag{4.16}$$

The expected value of $G(\theta, \phi)$ in Equation (4.16) is expressed by

$$< G(\theta, \phi) >= \frac{4\pi}{\lambda^2} \iint dA_\tau \Phi(\bar{\tau}) e^{-i\bar{k}\cdot\bar{\tau}} (< \cos\gamma(\bar{\tau}) > +i < \sin\gamma(\bar{\tau}) >) \tag{4.17}$$

For large values of τ compared to the correlation interval $2l$, the phase values at the two points should be uncorrelated, making $\gamma(\tau)$ a normally distributed random variable with zero mean and variance $2\sigma^2$, where σ^2 is the variance of $\delta(\bar{\rho})$. When τ is getting small, $\gamma(\tau)$ approaches zero with a zero variance. We will assume that $\gamma(\tau)$ has the following variance function

$$< \gamma^2(\tau) >= 2\sigma^2 (1 - e^{-\tau^2/4l^2}) \tag{4.18}$$

Then we have

$$\begin{aligned} < \cos\gamma(\tau) > &= \int_{-\infty}^{\infty} \cos\gamma \frac{1}{\sqrt{4\pi < \gamma^2 >}} e^{-\gamma^2/4<\gamma^2>} d\gamma \\ &= e^{-\sigma^2}(1 - e^{-\tau^2/4l^2}) \qquad (4.19) \\ < \sin\gamma(\tau) > &= 0 \qquad (4.20) \end{aligned}$$

Equation (4.17) can be rewritten as

$$
\begin{aligned}
< G(\theta,\phi) > &= \frac{4\pi}{\lambda^2}e^{-\sigma^2}\iint dA_\tau \Phi(\bar{\tau})e^{-i\bar{k}\cdot\bar{\tau}}e^{\sigma^2 e^{-(\tau/2l)^2}} \\
&= \frac{4\pi}{\lambda^2}e^{-\sigma^2}\sum_{n=0}^{\infty}\iint dA_\tau \Phi(\bar{\tau})e^{-i\bar{k}\cdot\bar{\tau}}\frac{\sigma^{2n}}{n!}e^{-n(\tau/2l)^2} \\
&= G_0(\theta,\phi)e^{-\sigma^2} + \frac{4\pi}{\lambda^2}e^{-\sigma^2}\sum_{n=1}^{\infty}\iint dA_\tau \Phi(\bar{\tau})e^{-i\bar{k}\cdot\bar{\tau}}\frac{\sigma^{2n}}{n!}e^{-n(\tau/2l)^2} \qquad (4.21)
\end{aligned}
$$

where $G_0(\theta,\phi)$ is the zero-error gain, and l is half the length of the correlation interval.

We will assume that the correlation interval $c = 2l$ is small compared to the aperture size. If we assume that the illumination correlation function $\Phi(\bar{\tau})$ in Equation (4.21) has a unit value, the integration can be performed, which yields the following result

$$
< G(\theta,\phi) >= G_0(\theta,\phi)e^{-\sigma^2} + \frac{8\pi^2}{\lambda^2}e^{-\sigma^2}\sum_{n=1}^{\infty}\frac{\sigma^{2n}}{n!}\int J_0(\frac{2\pi}{\lambda}\tau\sin\theta)e^{-n\tau^2/4l^2}\tau d\tau \qquad (4.22)
$$

Using the following substitution

$$
\int_0^{\infty} J_0(\frac{2\pi}{\lambda}\tau\sin\theta)e^{-n\tau^2/4l^2}\tau d\tau = \frac{2l^2}{n}e^{-\pi(\sin\theta/\lambda)^2/n} \qquad (4.23)
$$

we have the general form of the antenna tolerance theory

$$
< G(\theta,\phi) >= G_0(\theta,\phi)e^{-\sigma^2} + \left(\frac{4\pi l}{\lambda}\right)^2 e^{-\sigma^2}\sum_{n=1}^{\infty}\frac{\sigma^{2n}}{n\cdot n!}e^{-(2\pi l\sin\theta/\lambda)^2/n} \qquad (4.24)
$$

According to the first term of Equation (4.24), the gain is reduced by an exponential factor to account for power scattered into the side lobes. The reduction for the gain on axis is expressed by

$$\frac{< G(0,0) >}{G_0(0,0)} = e^{-\sigma^2} + \frac{1}{\eta_{ap}} \left(\frac{4l}{D}\right)^2 e^{-\sigma^2} \sum_{n=1}^{\infty} \frac{\sigma^{2n}}{n \cdot n!} \tag{4.25}$$

where $\eta_{ap} = G_0(0,0)(\lambda/\pi D)^2$ is the aperture efficiency of the reflector, and D is the diameter of the circular aperture. For a shallow reflector, we may assume the following relation between the standard deviation σ of the phase perturbation and the root-mean-square value of the normal surface errors (see Appendix B)

$$\sigma \approx 4\pi\varepsilon_{rms}/\lambda \tag{4.26}$$

where ε_{rms} is the rms surface error. For a small correlation interval, the second term in Equation (4.25) can be neglected, leaving

$$G_{max} = \eta_{ap} \left(\frac{\pi D}{\lambda}\right)^2 e^{-(4\pi\varepsilon_{rms}/\lambda)^2} \tag{4.27}$$

By assuming fixed values of η_{ap}, D, and ε_{rms} and taking the derivative of Equation (4.27) with respect to λ, we arrive at the optimal operating wavelength $\lambda_{max} = 4\pi\varepsilon_{rms}$. The maximum gain at this wavelength is equal to $G_{max} \approx \frac{\eta_{ap}}{43}(D/\varepsilon_{rms})^2$, which is at 4.3 dB below the error-free level. The optimum gain is determined by the square of the precision of manufacturing D/ε_{rms} and the aperture efficiency.

4.3.2 Results

Figure 4-19 and Figure 4-20 show patterns on the E-plane from the antenna tolerance theory. The results are calculated from Equation (4.24) with $G_0(\theta, \phi)$ being the ideal pattern from GO. They display similar trends for pattern degradation like those obtained previously from GO and PO. However, the degree of deterioration is much worse for the case of the tolerance theory as we can see from the side lobes of the co-polarized patterns and the on-axis ($\theta = 0$) cross-polarization.

Figure 4-21 and Figure 4-22 show two comparisons between the average patterns from GO and PO and those from the antenna tolerance theory for $\varepsilon_{rms} = 0.005\lambda$ and $\varepsilon_{rms} = 0.05\lambda$ respectively. It is clear from the figures that the antenna tolerance theory predicts worse degradation than our results. In any case, results from PO should be used as a standard due to its superior formulation. It can be seen that in the region near the main lobe, our results agree better with those from PO than those given by the tolerance theory.

4.4 Conclusion

In this chapter, we present results from the application of our model to study the effects of Gaussian random surface errors on the paraboloidal reflector based on the Monte Carlo simulation. The results show that almost all of the performance parameters associated with the radiation patterns are degraded by the presence of random surface errors on the reflector. We found that the the maximum gain decreases with the increasing level of rms surface errors, whereas the side lobe and cross-polarization levels increases. The only exception is

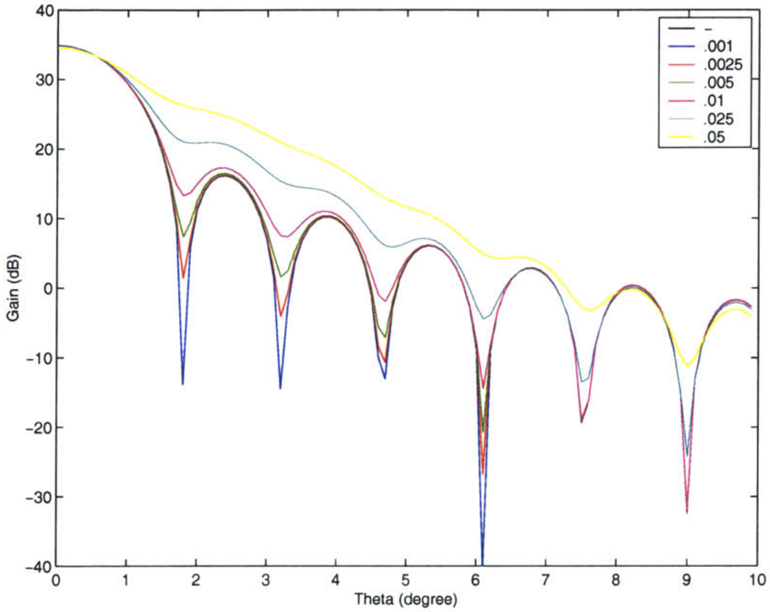

Figure 4-19: Average gain patterns of the co-polarized field on the E-plane from a paraboloidal reflector with various degrees of random surface errors. The patterns are obtained from the antenna tolerance theory ($D = 40.0, \lambda = 1.0, l = 4.0, n = 100$).

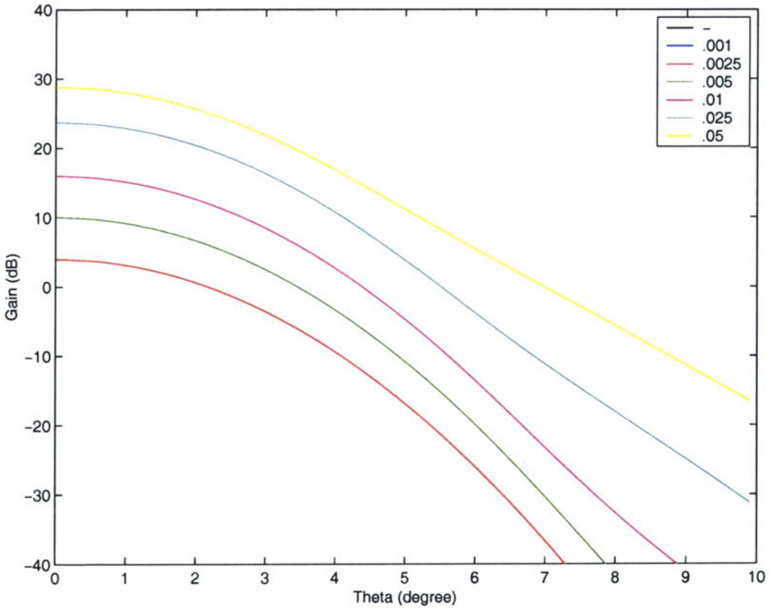

Figure 4-20: Average gain patterns of the cross-polarized field on the E-plane from a paraboloidal reflector with various degrees of random surface errors. The patterns are obtained from the antenna tolerance theory ($D = 40.0, \lambda = 1.0, l = 4.0, n = 100$).

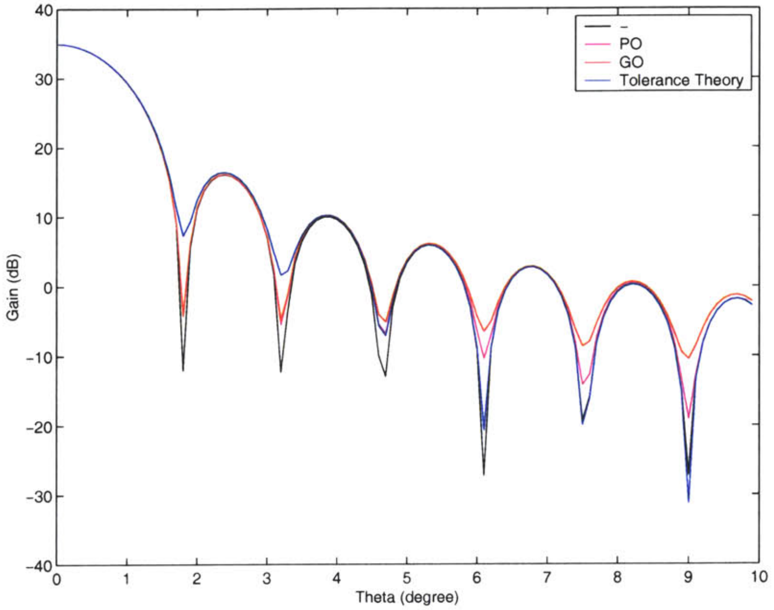

Figure 4-21: A comparison between results from GO, PO and the antenna tolerance theory for $\varepsilon_{rms} = 0.005\lambda$.

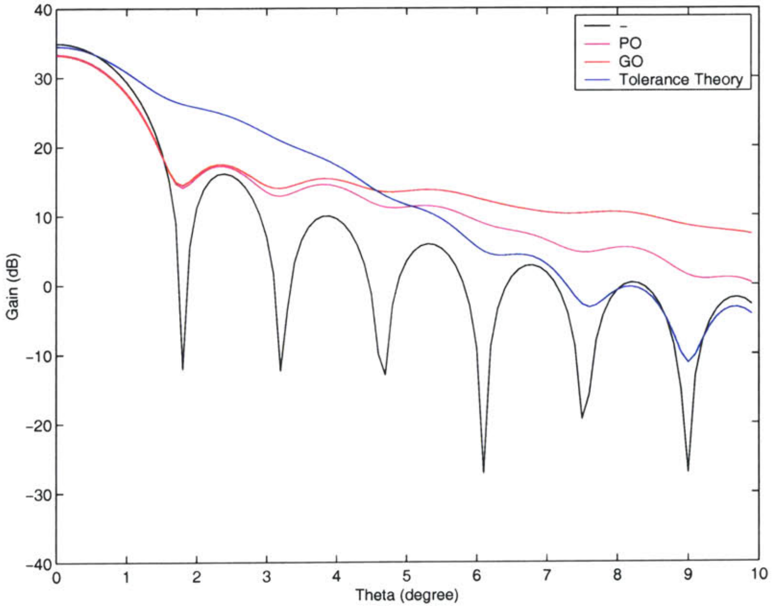

Figure 4-22: A comparison between results from GO, PO and the antenna tolerance theory for $\varepsilon_{rms} = 0.05\lambda$.

the beamwidth, which does not display obvious changes. In addition, we have found that our model gives better results than the antenna tolerance theory, which is the analog to our GO-based approach. The results seem to agree well when the $\varepsilon_{rms}/\lambda$ is lower than 1/100. When the ratio rises beyond this level, the disagreement is quite large, and results from the antenna tolerance theory should not be considered accurate.

Chapter 5

Conclusion and suggestions for future work

We have proposed and presented the development of a method to study the effects of random surface errors on the performance of paraboloidal reflector antennas. Our method is based on geometrical optics ray tracing and integration of the current elements on the aperture plane of the reflectors. The parameters that describe the current elements will reflect changes due to the random surface errors on the antenna surface, which will present themselves in the radiation patterns.

The random surface errors are assumed to have Gaussian statistics. An ensemble of these surfaces are created to be used in the Monte Carlo simulation.

The results show that almost all of the performance parameters associated with the radiation patterns—the maximum gain, side lobe levels, and cross-polarization—are degraded by the presence of random surface errors on the surface of the reflector. The degree of degradation increases with the levels of the rms surface errors. In addition, we have found that our model gives better results than the antenna tolerance theory, whose accuracy is limited to the very low level of rms surface errors.

Based on this work, we would like to make a few suggestions for future work. First, our program can be used to study the effects of random surface errors on paraboloidal reflector antennas with different configurations such as the sizes, shapes of the dish, and the feed factor.

Second, from the collection of data from the Monte Carlo simulation, we should be able to arrive at some probability laws to describe some performance parameters such as the directivity, the gain, the beamwidths, the cross-polarization interference, and the side lobe levels. This will be a more useful information than the mean distribution of these parameters to characterize the influence of the random surface errors on the radiation patterns. In addition, we will have an opportunity to study some features that have seldom been reported in the literature such as the shifting of positions of the peak side lobes (see Figure 4-6) or the null positions as a function of the rms surface errors.

Appendix A

Radiation from electric current source

In antenna and radiation problems, we are interested in finding the electromagnetic solution to Maxwell's equations given a time-harmonic current source distribution $\overline{J}(\overline{r})$. We begin with the Faraday's and Ampere's laws in phasor form

$$\nabla \times \overline{E}(\overline{r}) = i\omega\mu\overline{H}(\overline{r}) \tag{A.1}$$

$$\nabla \times \overline{H}(\overline{r}) = -i\omega\epsilon\overline{E}(\overline{r}) + \overline{J}(\overline{r}) \tag{A.2}$$

By substituting $\overline{H}(\overline{r})$ from Equation (A.1) into Equation (A.2), we obtain the following equation

$$\nabla \times \nabla \times \overline{E}(\overline{r}) - k^2\overline{E}(\overline{r}) = i\omega\mu\overline{J}(\overline{r}) \tag{A.3}$$

where $k^2 = \omega^2\mu\epsilon$. Assuming that the source distribution $\overline{J}(\overline{r})$ lies in an unbounded isotropic medium, and the observation point is outside of the source region as shown in Figure A-1. In terms of the scalar Green's function in spherical coordinates , we find a solution for the

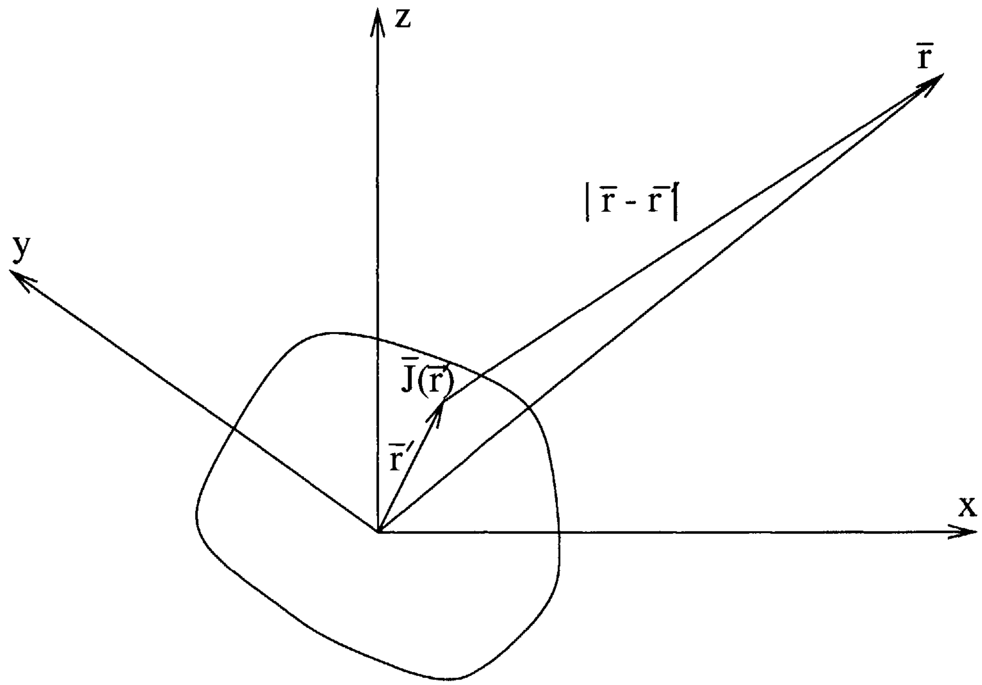

Figure A-1: Radiation from a current source.

electric field [7]

$$\overline{E}(\overline{r}) = i\omega\mu \left[\overline{\overline{I}} + \frac{1}{k^2}\nabla\nabla\right] \cdot \iiint dV' \, \frac{e^{ik|\overline{r}-\overline{r}'|}}{4\pi|\overline{r}-\overline{r}'|}\overline{J}(\overline{r}') \tag{A.4}$$

Once the electric field is solved, the magnetic field can be calculated from Faraday's law in Equation (A.1).

For observation points which are very far away from the source, all wave vectors originating from different parts of the source are essentially parallel. The radiation field (far field) can be approximated with the following conditions

$$|\overline{r} - \overline{r}'| = r - \hat{r} \cdot \overline{r}' \tag{A.5}$$

$$kr \gg 1 \tag{A.6}$$

In the radiation zone, the $\overline{k}$ vector is in the $\hat{r}$ direction ($\overline{k} = k\hat{r}$). Neglecting $\hat{r} \cdot \overline{r}'$ in the denominator, the electric field is

$$\begin{aligned} \overline{E}(\overline{r}) &= i\omega\mu \left[\overline{\overline{I}} + \frac{1}{k^2}\nabla\nabla\right] \cdot \iiint dV' \,\overline{J}(\overline{r}') \frac{e^{ik|\overline{r}-\overline{r}'|}}{4\pi|\overline{r}-\overline{r}'|} \\ &= i\omega\mu \left[\overline{\overline{I}} + \frac{1}{k^2}\nabla\nabla\right] \cdot \frac{e^{ikr}}{4\pi r} \iiint dV' \,\overline{J}(\overline{r}') e^{-i\overline{k}\cdot\overline{r}'} \end{aligned} \tag{A.7}$$

Since the current density $\overline{J}(\overline{r}')$, which is weighted with the phase retardation factor $e^{-i\overline{k}\cdot\overline{r}'}$, is integrated over the volume of $\overline{r}'$, the electric field will be a function of θ and ϕ only. In terms of the vector current moment, which is defined as

$$\overline{f}(\theta,\phi) = \iiint dV' \,\overline{J}(\overline{r}') e^{-i\overline{k}\cdot\overline{r}'} \tag{A.8}$$

and replacing the del operator by $i\overline{k}$, the far field in Equation (A.7) becomes

$$\begin{aligned} \overline{E}(\overline{r}) &= i\omega\mu[\overline{\overline{I}} - \hat{r}\hat{r}] \cdot \overline{f} \frac{e^{ikr}}{4\pi r} \\ &= i\omega\mu \frac{e^{ikr}}{4\pi r} (\hat{\theta} f_\theta + \hat{\phi} f_\phi) \end{aligned} \tag{A.9}$$

where $\overline{f}(\theta,\phi) = \hat{r} f_r + \hat{\theta} f_\theta + \hat{\phi} f_\phi$.

Under the same far-field approximation, the magnetic field $\overline{H}(\overline{r})$ is

$$\overline{H}(\overline{r}) = \frac{1}{i\omega\mu} \nabla \times \overline{E}(\overline{r}) = \frac{\overline{k}}{\omega\mu} \times \overline{E}(\overline{r}) = ik \frac{e^{ikr}}{4\pi r} (\hat{\phi} f_\theta - \hat{\theta} f_\phi) \tag{A.10}$$

Appendix B

Change of path length due to deviation on the reflector surface

At a point on the reflector surface at which the normal surface deviation is equal to h_i, the total change in the geometrical optics path length is

$$\begin{aligned} \Delta R &= d_1 + d_2 \\ &= d_1 + d_1 \cos 2\alpha_i \\ &= 2d_1 \cos^2 \alpha_i \\ &= 2h_i \cos \alpha_i \end{aligned} \tag{B.1}$$

Thus, the total change in the path length at a point on the reflector surface is equal to twice the axial component of the normal deviation at that point. When the reflector is relatively flat or at locations near the center, we may assume $\Delta R = 2h_i$.

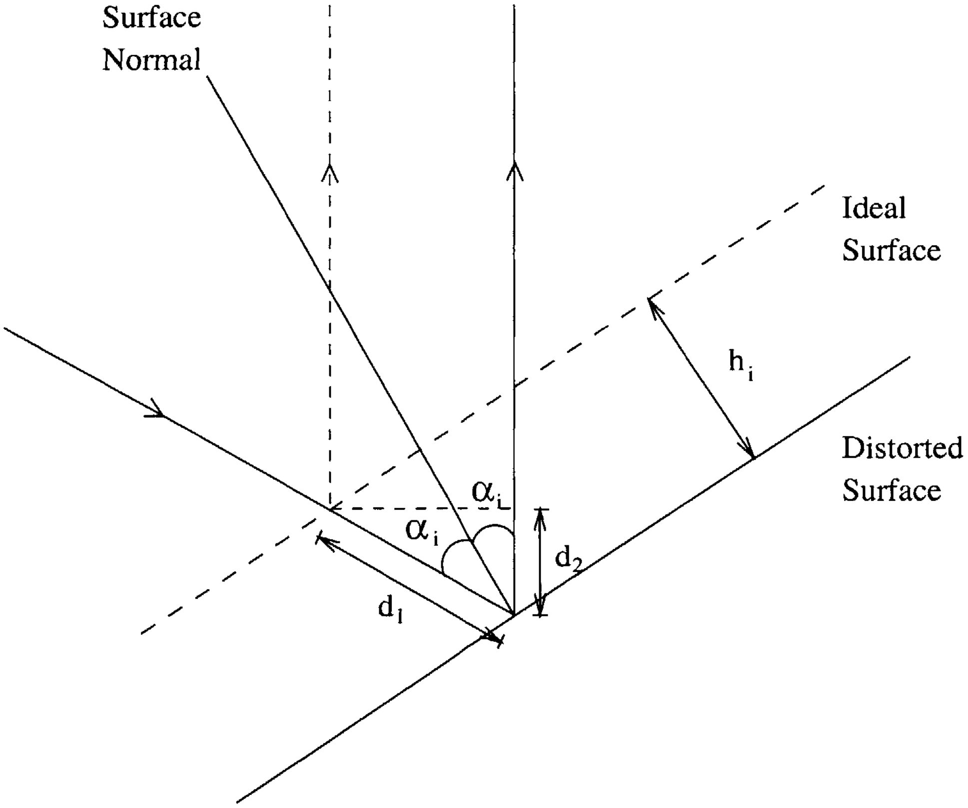

Figure B-1: Change of path length due to deviation on the reflector surface

Bibliography

[1] IEEE Standard Definitions of Terms for Antennas. *IEEE Trans. Antennas Propagat.*, AP-31:1019–1025, November 1983.

[2] C. C. Cutler. Parabolic Antenna Design for Microwaves. *Proc. IRE*, 35:1284–1294, November 1947.

[3] A. W. Love. Some Highlights in Reflector Antenna Development. *Radio Science*, 11:671–684, August 1976.

[4] C. M. Rappaport. Analysis of Scanning in Dual Offset Reflector Antennas and the Bifocal System. Master of Science and Engineering, Massachusetts Institute of Technology, EECS Department, 1982.

[5] D. H. Staelin, A. W. Morgenthaler, and J. A. Kong. *Electromagnetic Waves.* Prentice-Hall, New Jersey, 1994.

[6] W. L. Stutzman and G. A. Thiele. *Antenna Theory and Design: Second Edition.* John Wiley & Sons, New York, 1998.

[7] J. A. Kong. *Electromagnetic Wave Theory.* John Wiley & Sons, New York, 1990.

[8] W. V. T. Rusch. The Current State of the Reflector Antenna Art–Entering the 1990. *Proceedings of the IEEE*, 80(1):113–126, January 1992.

[9] M. Safak. Limitations on Reflector Antenna Gain by Random Surface Errors, Pointing Errors, and the Angle-of-Arrival Jitter. *IEEE Trans. Antennas Propagat.*, 38(1):117–121, January 1990.

[10] Y. Rahmat-Samii. An Efficient Computational Method for Characterizing the Effects of Random Surface Errors on the Average Power Pattern of Reflectors. *IEEE Trans. Antennas Propagat.*, AP-31(1):92–98, January 1983.

[11] J. Ruze. Antenna Tolerance Theory-A Review. *Proc. IEEE*, 54:633–640, April 1966.

[12] M. J. Brenner, A. J. Ellder, and M. S. Zarghamee. Upgrade of a Large Millimeter-Wavelength Radio Telescope for Improved Performance at 115 GHz. *IEEE Trans. Antennas Propagat.*, 82(5):734–741, May 1994.

[13] M. I. Skolnik. Large Antenna Systems. In R. E. Collin and F. J. Zucker, editors, *Antenna Theory: Part 2*, pages 655–674. McGraw-Hill, New York, 1969.

[14] W. T. Smith, R. J. Bastian, and S. Y. Cheah. An Efficient Neural Network Algorithm for Reflector Surface Error Compensation. *IEEE Trans. Antennas Propagat.*, 44(2):137–142, February 1996.

[15] M. S. Zarghamee. On Antenna Tolerance Theory. *IEEE Trans. Antennas Propagat.*, AP-15:777–781, November 1967.

[16] S. Silver. *Microwave Antenna Theory and Design*. McGraw-Hill, New York, 1949.

[17] R. E. Collin. *Antennas and Radiowave Propagation.* McGraw-Hill, New York, 1985.

[18] S. I. Ghobrial. Axial Cross Polarization in Reflector Antennas with Surface Imperfections. *IEEE Trans. Antennas Propagat.*, AP-28(5):610–616, September 1980.

[19] S. Wu and Y. Rahmat-Samii. Beam Efficiency of Large Reflector Antennas Subject to Correlated Random Surface Errors. *Antennas and Propagat. Society International Symposium*, 1:144–147, 1990.

[20] D. K. Cheng. Effect of Arbitrary Phase Errors on the Gain and Beamwidth Characteristics of Radiation Pattern. *IEEE Trans. Antennas Propagat.*, AP-3:145–147, July 1955.

[21] H. Ling, Y. T. Lo, and Y. Rahmat-Samii. Reflector Sidelobe Degradation Due to Random Surface Errors. *IEEE Trans. Antennas Propagat.*, AP-34:164–172, February 1986.

[22] J. Kim, B. S. Kim, S. Nam, and W. Lee. Computation of the Average Power Pattern of a Reflector Antenna with Random Surface Errors and Misalignment Errors. *IEEE Trans. Antennas Propagat.*, 44(7):996–999, July 1996.

[23] J. A. Jervase and S. I. Ghobrial. Axial Cross Polarization in Reflector Antennas with Surface Errors of Large Correlation Diameter. *IEEE Trans. Antennas Propagat.*, AP-31(4):662–665, July 1983.

[24] V. K. Tripp. A New Approach to the Analysis of Random Errors in Aperture Antennas. *IEEE Trans. Antennas Propagat.*, AP-32(8):857–863, August 1984.

[25] A. Lindley. Analysis of Distorted Reflector Antennas. *Sixth International Conference on Antennas and Propagation (ICAP 89)*, 1:32–34, 1989.

[26] T. H. Legg. A New Aperture Plane Method of Measuring Antenna Surface Errors. *IEEE Trans. Antennas Propagat.*, 42(1):116–119, January 1994.

[27] T. B. Vu. The Effect of Phase Errors on the Forward Gain. *IEEE Trans. Antennas Propagat.*, AP-13:981–982, November 1965.

[28] W. L. Stutzman, S. W. Gilmore, and S. H. Stewart. Numerical Evaluation of Radiation Integrals for Reflector Antenna Analysis Including a New Measure of Accuracy. *IEEE Trans. Antennas Propagat.*, 36(7):1018–1023, July 1988.

[29] G. A. Deschamps. Ray Techniques in Electromagnetics. *Proc. IEEE*, 60:1022–1035, September 1972.

[30] M. A. Campo, J. R. Franscisco, J. L. Besada, and L. de Haro. SABOR: Description of the Methods Applied for a Fast Analysis of Horn and Reflector Antennas. *IEEE Antennas and Propagation Magazine*, 40(4):95–108, August 1998.

[31] W. T. Smith and W. L. Stutzman. A Comparison of Physical Optics and Geometrical Optics Methods for Computation of Reflector Surface Error Effects. *IEEE Proceedings of Energy and Information Technologies in the Southeast*, pages 214–219, 1989.

[32] A. D. Yaghjian. Equivalence of Surface Current and Aperture Field Integrations for Reflector Antennas. *IEEE Trans. Antennas Propagat.*, AP-32(12):1355–1357, December 1984.

[33] S. F. Holt. Wave Fronts, Rays, and Focal Surfaces. In R. E. Collin and F. J. Zucker, editors, *Antenna Theory: Part 2*, pages 1–35. McGraw-Hill, New York, 1969.

[34] C. A. Balanis. *Antenna Theory: Analysis and Design.* Harper & Row, New York, 1982.

[35] J. F. Kauffman, W. F. Croswell, and L. J. Jowers. Analysis of the Radiation Patterns of Reflector Antennas. *IEEE Trans. Antennas Propagat.*, AP(24):53–65, January 1976.

[36] J. B. Keller. Geometrical Theory of Diffraction. *J. Opt. Soc. Amer.*, 52:116–130, 1962.

[37] A. C. Ludwig. The Definition of Cross Polarization. *IEEE Trans. Antennas Propagat.*, AP-21:116–119, January 1973.

[38] C. J. Sletten. Reflector Antennas. In R. E. Collin and F. J. Zucker, editors, *Antenna Theory: Part 2*, pages 37–75. McGraw-Hill, New York, 1969.

[39] A. J. Booysen. A Physical Interpretation of the Equivalence Theorem. *IEEE Trans. Antennas and Propagat.*, 48(8):1260–1262, August 2000.

[40] W. V. T. Rusch and P. D. Potter. *Analysis of Reflector Antennas.* Academic Press, New York, 1970.

[41] S. C. Wu, M. F. Chen, and A. K. Fung. Non-Gaussian Surface Generation. *IEEE Trans. Geos. and Remote Sensing*, 26(6):885–888, November 1988.

[42] A. K. Fung, A. J. Blanchard, and M. F. Chen. Polarization Properties in Random Surface Scattering. In J. A. Kong, editor, *PIER3 Progress in Electromagnetic Research: Polarimetric Remote Sensing*, pages 143–225. Elsevier Science Publishing, New York, 1990.

[43] A. V. Oppenheim, A. S. Willsky & I. T. Young. *Signals and Systems.* Prentice-Hall, New Jersey, 1983.

[44] W. H. Press, S. A. Teukolsky, W. T. Vetterling and B. P. Flannery. *Numerical Recipes in C: Second Edition.* Cambridge University Press, New York, 1992.

[45] H. Stark and J. W. Woods. *Probability, Random Processes, and Estimation Theory for Engineers: Second Edition.* Prentice-Hall, New Jersey, 1994.

[46] R. T. Marchand and G. S. Brown. Inferring Rough Surface Parameters from Average Scattering Data Using Approximate Scattering Models: 1. Gaussian Spectrum. *Radio Science*, 33:821–834, Jul-Aug 1998.

[47] W. B. Davenport and W. L. Root. *An Introduction to the Theory of Random Signals and Noise.* McGraw-Hill, New York, 1958.

[48] P. Kildal. Analysis of Numerically Specified Multireflector Antennas by Kinemetic and Dynamic Ray Tracing. *IEEE Trans. Antennas Propagat.*, AP-28(5):610–616, September 1980.